Growing Bubbles and Freezing Drops

depletion effects and tip singularities

Oscar R. Enríquez Paz y Puente

The different regimes of bubble growth in a slightly supersaturated solution can be correctly understood by plotting the rate of change of the bubble area, rather than the radius, as a function of time.

In principle it should be possible to visualise the convective flow around our growing bubbles by interferometric techniques. However, this would require confining the bubbles in a Hele-Shaw type of geometry in order to shorten the optical path.

The formation of pointy tips on freezing water drops is the cause of a crucial aspect of ice preparation for a Curling match. [Comment received in connection with freezing droplet video produced for the Gallery of Fluid Motion 2012]

The impossibility of predicting the side-effects of drastic techno-scientific solutions to our (environmental) problems –*e.g.* geo-engineering– makes their appropriateness questionable. This suggests that the wisest option is to start doing a lot less of what we already know to be detrimental to the environment. However, this can only happen if we manage to re-think our society outside the dogma of economic growth.

The political neutrality of science is a myth that scientists should be wary of. Inasmuch as science takes place in society, and as social life is inseparable from politics, there is always politics at work in the production of science.

The central aspect of science in the 'knowledge economy' calls for scientists to reflect on the broader implications of their work and whether they agree with the underlying normative presuppositions concerning the optimal organisation of society.

"We should be on our guard not to overestimate science and scientific methods when it is a question of human problems; and we should not assume that experts are the only ones who have a right to express themselves on questions affecting the organisation of society." [Albert Einstein, Why Socialism? Monthly Review 61(1), 2009 (originally published in 1949)]

Not too long ago philosophers and scientists were the same people. Today scientists seem to be 'highly-qualified' labourers or 'high-value human capital'. (Higher) education should recover a strong philosophical component in order to form sensitive and critical citizens, rather than competitive individuals, "leaders" and neo-colonial "global citizens" . [Reflection after reading our University's 2020 Vision]

When looking at the current socio-economical order and power relations it is hard to find room for optimism. However, there is room for hope; it resides in the social movements that seek to maintain or recover the sense of community life and organise to construct true autonomy and a world were many worlds fit.

GROWING BUBBLES AND FREEZING DROPS: DEPLETION EFFECTS AND TIP SINGULARITIES

Oscar R. Enríquez Paz y Puente

Thesis committee members:

Prof. Dr. Ir. Leen van Wijngaarden (chairman)	UT, Enschede
Prof. Dr. Devaraj van der Meer (promotor)	UT, Enschede
Prof. Dr. Andrea Prosperetti (promotor)	Johns Hopkins University, Baltimore
Assoc. Prof. Dr. Chao Sun (copromotor)	UT, Enschede
Prof. Dr. Javier Rodríguez Rodríguez	Universidad Carlos III, Madrid
Prof. Dr. Anton Darhuber	TU/e, Eindhoven
Prof. Dr. Detlef Lohse	UT, Enschede
Prof. Dr. Serge Lemay	UT, Enschede

The work in this thesis was carried out at the Physics of Fluids group of the Faculty of Science and Technology of the University of Twente. This thesis was financially supported by the FOM-Shell Industrial Partnership Program, and the National Council of Science and Technology (CONACyT) of Mexico

Dutch title:
Groeiende bellen en bevriezende druppels: Het spel van de concentratiegradiënt

Publisher:
Oscar R. Enríquez Paz y Puente, Physics of Fluids, University of Twente,
P.O. Box 217, 7500 AE Enschede, The Netherlands

Cover image:
Experimental image of in-line growing bubbles on watercolour background by Daniela Flores Magón Bustamante

ISBN: 978-90-365-3814-5

GROWING BUBBLES AND FREEZING DROPS: DEPLETION EFFECTS AND TIP SINGULARITIES

DISSERTATION

to obtain
the degree of doctor at the University of Twente,
on the authority of the rector magnificus,
Prof. Dr. H. Brinksma,
on account of the decision of the graduation committee,
to be publicly defended
on Wednesday the 14th of January 2015 at 16:45

by

Oscar Raúl Enríquez Paz y Puente
Born on the 13th of September 1983
in Mexico City, Mexico

This dissertation has been approved by the promotors:

Prof. Dr. Devaraj van der Meer,

Prof. Dr. Andrea Prosperetti

and the copromotor:

Assoc. Prof. Dr. Chao Sun

Contents

1 Introduction

1.1 Bubbles and some of their multiple manifestations

In Art and Society

Children's Games (Kunsthistorisches Museum, Vienna), by Pieter Bruegel the Elder (ca. 1526–1569), is a nice allegory of two of the motivations that lured me to the path which lead to this thesis: the aesthetic beauty of fluid flow phenomena and the ludic nature of the experimental work which is necessary to visualize or understand the behaviour of fluids in diverse situations. Bruegel, in the characteristic style of the Flemish Renaissance painters, presents us with a crowded scene of children absorbed in all sorts of games –which might allude to the scientific endeavour in general–. A direct connection with this thesis, besides the geographical one, is given in the lower, left-hand corner where a child amuses himself blowing soap bubbles (shown in the detail) in a manner only slightly different to what I have done in the lab during the past few years.

Not only a long-lived source of amusement, bubbles have also been a recurring metaphor in Western literary and pictorial traditions [1] to evoke the ephemerality of life. This can be traced at least as far back as an ancient Greek proverb –here in its Latin version– *Homo bulla est*: "Man is a bubble" [2]. These days, perhaps the figurative use encountered most frequently comes from economics. Apparently it was in the early ninetieth century [3] that 'bubble' was adopted as the nickname for a process of significant increase in the price of a certain good, driven by speculation, which ends in a sudden –and violent– collapse. Although the famous Dutch

Figure 1.1: *Children's Games* (Kunsthistorisches Museum, Vienna), by Pieter Bruegel the Elder (ca. 1526-1569). The detail comes from the left-hand, lower corner and shows a child blowing a soap bubble (center).

"Tulip Mania" of the 1600's is usually considered as first occurrence of this kind of phenomenon [4], the term 'bubble' was taken up in connection to the plunge of the South Sea Company stock value in England in 1720, regarded as the first international stock market burst [3].

In Physical Sciences and Industry

Symbolic allusions aside, physical bubbles –volumes of gaseous matter which are clearly, but subtly, delimited from their surroundings– have also elicited considerable scientific curiosity, and remarkably continue to do so, as testified by a growing body of literature on the topic [5–8]. Interest in them ranges from geophysics, where bubbles might lead to volcanic eruptions [9–12] to the medical consequences of bubble formation in the blood and tissues during decompression disease [13, 14]. Technological applications for bubbles are also abundant, such as ultrasound contrast agents [15], targeted drug delivery [16], biomass reactors [17] or treatment of residues [18].

Bubbles can be classified according to three categories: what they are surrounded by, what they are filled with and how they were formed. In terms of their surroundings there are two options: gas or liquid. Sure, there can also be bubbles in solids, but these were most likely trapped there when the solid was a liquid (*e.g.* glass [19–21], plastics [22–25], metals [26] or some kinds of volcanic rock [27]) or otherwise formed by an explosive event which temporarily fluidized the solid. Bubbles surrounded by gas must be separated from it by a thin material, like a lipid or polymer shell or a soap film [15]. Those in a liquid are the most common type and can have either a separating shell or a direct interface with their encompassing medium.

Regarding their contents, the options are gas, vapour or a mixture of both. Although vapour is a gaseous phase, it can coexist with its liquid and solid phases and can be condensed back to liquid form by isothermal compression, whereas a gas can do neither.

Finally, bubbles can be formed by direct mechanical means, chemical reactions, cavitation, boiling or nucleation. The first two methods are easy to distinguish. Mechanical means are exemplified by forced mixing of a gas into a liquid [28], injection of gas through a needle [29], impact of an object and the ensuing gas entrapment [30, 31], or the blowing of soap bubbles. Examples of bubble formation by chemical reactions are electrolysis [32, 33], acid-base reactions such as vinegar with baking soda, and fermentation processes [34]. Cavitation and boiling are perhaps a bit difficult to separate. While both of them imply a phase change from a pure liquid to vapour, cavitation is traditionally considered to be caused by pressure reduction while boiling is caused by heating. However, the advent of laser-induced cavitation broadened the definition to include a phase change caused by sudden, very localized heating. Nucleation usually refers to the formation of gas bubbles in a solution which

contains gas in excess of its saturation concentration. If it happens in the bulk, it is called classical nucleation and it requires very high levels of supersaturation to overcome the energy barrier for the formation of an interface inside the liquid [35]. For small and medium supersaturation, it requires the presence of pre-existing gas cavities, known as nucleation sites [36]. Nonetheless, nucleation can also not be completely separated from boiling. In a boiling process, bubbles are also said to nucleate, usually on the walls of its container; whereas in order for boiling to start in the liquid bulk, a high level of superheating is required [37] analogously to the classical nucleation process for a supersaturated solution. Furthermore, in the boiling of normal tap water (which contains dissolved air) bubble growth occurs both by nucleation of air bubbles and vaporization of water. The first bubbles observed in the bottom of the pot where one heats water to cook pasta or something else, grow mainly because the temperature increase makes the water supersaturated with respect to its content of air but also because the interface created by these bubbles allows for some vaporization of the liquid before the boiling temperature is reached; at which point boiling properly starts.

1.2 Bubbles in supersaturated liquids

We now turn our attention to the kind of bubbles featured in this thesis: gas bubbles growing in a supersaturated liquid solution. These are the kind of bubbles that grow, among other places, in carbonated drinks [38–42], in the blood or tissues of scuba divers undergoing decompression sickness [13, 14], in the degassing of magmas that can lead to volcanic eruptions [9–12] or during solution-gas-drive oil production as the pressure of the reservoir drops [43–47]. Although significant theoretical, numerical and experimental works have been performed in connection with all these areas, the understanding of how bubbles grow and interact when they are close to each other is far from complete. Specifically, in the limit where supersaturation is low (ten times lower than in carbonated drinks) to our knowledge there are no previous experimental studies. In this limit, bubble growth should take place quasi-statically, without the influence of advection caused by the expanding bubble surface. Understanding what happens in this regime is particularly relevant in the context of solution-gas-drive where supersaturation develops at a very slow pace.

The amount of gas that can be dissolved in a liquid, *i.e.*, its equilibrium concentration c is directly proportional to the partial pressure P of that gas above the liquid. This is stated by Henry's law as

$$c = k_H(T)P \tag{1.1}$$

where k_H is known as Henry's coefficient and is a decreasing function of the temperature T specific to each gas-liquid pair.

A saturated solution with conditions T_0, P_0 and c_0 will become supersaturated if its temperature increases to T_s or the pressure is decreased to P_s. The supersaturation coefficient is then defined as

$$\zeta = \frac{c_0 - c_s}{c_s} \tag{1.2}$$

where c_s is the concentration that would be in equilibrium at the new conditions, *i.e.*, $c_s = k_H(T_s)P_s$.

Upon supersaturation, gas will come out of the liquid until an equilibrium state is restored, either by reaching c_s in an open system (*e.g.* a carbonated drink left open and gone 'flat') or by restoring some of the pressure above the liquid and settling at new P_n, T_n and c_n conditions in a closed system (*e.g.* a carbonated drink taken out of the refrigerator, opened, closed again and left outside). It is known that most of the gas escapes through the free surface by diffusion [40], but given the right conditions, *i.e.*, very large supersaturation or the presence of nucleation sites for moderate or low supersaturation, bubbles will also form. Examples of this last case are carbonated beverages [38–42, 48], bubble formation during decompression disease [13, 14], and the ex-solution of gasses during oil extraction [43–47].

It is the limit of small supersaturation that interests us in this work. Whereas bubbly drinks have supersaturation coefficients ζ ranging from 2 to 5, all our experiments were done with $\zeta < 0.5$. Such low supersaturation is similar to what is expected during oil extraction, where the pressure decreases very slowly (a few bar each day). It has been observed in the oil industry that this leads to the growth of bubbles, which can either produce what is known as 'foamy oil', where bubbles do not coalesce and is therefore produced at a higher rate, or it can result in the formation of a continuous gas phase that slows down the production.

Our objective is to look into the mechanisms of bubble growth and interaction in the low supersaturation limit, where, to our knowledge, no previous experimental studies have been done. As liquid we use water, and as gas CO_2 (or N_2 in a few experiments). These choices are due to the ready availability of the liquid and the relatively high solubility of CO_2 in it. Theoretical solutions predict a quasi-static, purely diffusion-driven growth, developing a concentration gradient in its surroundings, without influence of inertial effects due to the expanding bubble interface and without natural convection. We shall see that this last consideration is not justified; in fact, the concentration gradient leads to natural convection, which plays an important role that changes the mass-transfer rate into the bubbles.

1.3 Freezing droplets and their singularities

If bubbles are usually gas cavities surrounded by a liquid (or sometimes a gas), droplets can be their exact opposite: small volumes of liquid encompassed by gas

(or sometimes a different liquid). Like for bubbles, there is no shortage of interest in phenomena involving droplets. The behaviour of droplets as they impact and spread on solid substrates [49], other liquids [50, 51], or granular materials [52] is still the subject of ongoing investigations. They are also researched in connection to ink-jet printing [53], levitation on hot [54] or moving surfaces [55], or explosive boiling [56].

When a water droplet is placed on a cold plate below its freezing temperature, it will freeze from the bottom up and form a sharp singular tip at the end of the process. As part of the playful exploration stimulated by the interaction with other curious people, we began to explore this phenomenon, and what started as a 'Friday afternoon' experiment soon turned into a serious investigation of the conditions that determine the tip shape. This led to interesting experiments, which included the freezing of 2D droplets in order to investigate the dynamics of the freezing front. Besides the interest in pointy ice drops related to, for example, frost formation [57] or solidification for freeze drying purposes [58], understanding the physics of solidification is crucial for processes like metal drop deposition or 3D printing.

1.4 This thesis

This thesis consists of experimental studies on two different topics: the diffusion-driven growth of gas bubbles and the conduction-driven freezing of a water droplet. The first takes place in a supersaturated dissolution of gas in water where bubbles grow from pre-existing gas pockets which allow for the establishment of directional mass-transfer processes, driven by local concentration gradients. The second occurs when a liquid water droplet is placed on a cold plate and a phase change process takes place from the plate up. Of the first, we study the effects that gas depletion of the surrounding medium has on the growth rate of both isolated and neighbouring bubbles. About the second, we investigate the formation of pointy singularities at the top of the droplet in the final stages of freezing. The two have in common the physical analogy between diffusive mass transfer and conductive heat transfer.

Chapter 2 is devoted to the experimental set-up that we built to study bubble growth. It describes the design and construction of the system and the processes used to prepare a saturated dissolution of CO_2 in water and afterwards make it supersaturated by means of a controlled pressure drop. In fact, the experiment is basically a rather high-tech soda machine. This chapter also explains the preparation of the silicon chips with hydrophobic pits that we use as nucleation sites, and reports the first tests and experiments performed.

In Chapter 3 we study the growth of an isolated gas bubble in a slightly supersaturated water-CO_2 solution. In contrast to previous experimental works in higher supersaturation regimes, our observations of the evolution of the bubble radius differed noticeably from theoretical solutions which, for diffusion-driven growth, predict that

the radius, $R(t)$, should be proportional to $t^{1/2}$. We traced back and disentangled the differences which were due to effects of the concentration boundary layer around the bubble and the presence of the substrate. In the early phase, growth was slowed down by the presence of the substrate; later on it was enhanced by the onset of density driven convection.

In Chapter 4 we delve further into the onset of density driven convection, which is caused by the density differences created by the development of a concentration profile around the bubble. Such density variations had been consistently neglected in previous works on bubble growth in supersaturated liquids, as they were deemed too small to have a noticeable effect. Here, we show that they are indeed responsible for the enhancement of the mass transfer rate into the bubble, and that we can predict the time of convection onset with a simple argument. We also tackle a recurring question that came up in many conversations and presentations on this topic, namely, whether this phenomenon also happens for other gasses, such as N_2.

Chapter 5 explores the interactions between bubbles that grow close to each other under a small supersaturation. We compare the growth of an isolated bubble to pairs, triplets in linear and triangular arrangements, and longer lines of bubbles at different distances. Two kinds of interactions were distinguished: spatial interactions between bubbles that grow close to each other simultaneously and temporal interactions which take place through the gas depletion of the surrounding medium by bubbles which grew previously from the same nucleation sites. As could be expected, the development of natural convection enriches and complicates the interactions.

In Chapter 6 we turn to the formation of tip singularities in freezing water drops. Although that phenomenon has been known for a long time and is clearly related to the expansion of water upon freezing, a quantitative description of the tip singularity has remained elusive. We performed systematic measurements of the tip angle, and revealed the dynamics of the solidification front through experiments with 2D freezing droplets in a Hele-Shaw cell. Our results suggest a universal, self-similar mechanism, independent on the solidification rate, which is in good agreement with the analytical model we propose.

2

Growing bubbles in a slightly supersaturated liquid solution *

We have designed and constructed an experimental system to study gas bubble growth in slightly supersaturated liquids. This is achieved by working with carbon dioxide dissolved in water, pressurized at a maximum pressure of 1 MPa *and applying a small pressure drop from saturation conditions. Bubbles grow from hydrophobic cavities etched on silicon wafers, which allow us to control their number and position. Hence, the experiment can be used to investigate the interaction among bubbles growing in close proximity when the main mass transfer mechanism is diffusion and there is a limited availability of the dissolved species.*

*Published as: [O.R. Enríquez, C. Hummelink, G-W. Bruggert, D. Lohse, A. Prosperetti, D. van der Meer and C. Sun, Growing bubbles in a slightly supersaturated liquid solution, Review of Scientific Instruments 84, 065111 (2013)].

2.1 Introduction

We study the growth of bubbles by gas diffusion in a liquid, which is the mass transfer mechanism when bubbles grow in a supersaturated solution. In experimental studies carried out so far [35,38,39] the flow induced by the growing bubble on its surroundings might not be negligible. The consequence of this is larger growth rates than expected for pure diffusion. In a solution that is only very slightly supersaturated, bubbles should grow quasi-statically and hence exclusively by diffusion. In this paper, after briefly introducing the context of supersaturated liquids, we describe an experimental system in which bubble growth can be studied under favourable conditions to isolate diffusion and where the number and position of bubbles can be controlled in order to study the interaction among them.

2.1.1 Supersaturation and its occurrence

The de-gassing of a supersaturated gas solution in a liquid takes place in a wide range of natural and industrial processes. Perhaps the most familiar examples are carbonated beverages, which have motivated a large amount of research on the physics and chemistry behind bubble formation, foaming and gushing in soda, beer and champagne [38–42]. Other examples include bubble growth in blood and tissues due to decompression sickness [13], de-gassing of magmas during volcanic eruptions [9], boiling-up of cryogenic solutions [59–61], production processes involving molten polymers, metals or glass [22], and ex-solution of gases during oil extraction [43].

As described by Henry's Law, the equilibrium (saturation) concentration, c, of gas in a liquid solution at a temperature T is proportional to the partial pressure P of the gas above the liquid:

$$c = k_H P. \tag{2.1}$$

Here k_H, the so-called Henry's constant, is specific to the gas-liquid pair and is a decreasing function of temperature. If a gas-liquid solution, with concentration c_0, in thermodynamic equilibrium at a pressure P_0 and temperature T_0, is brought to a lower pressure P_s and/or higher temperature T_s, it becomes supersaturated with respect to the equilibrium concentration $c_s = k_H(T_s)\,P_s$ at the new conditions. The excess amount of dissolved gas can be characterized in terms of the supersaturation ratio ζ defined by

$$\zeta = \frac{c_0 - c_s}{c_s} = \frac{\Delta c}{c_s} \tag{2.2}$$

Clearly, supersaturation requires that $\zeta > 0$.

Upon supersaturation, the excess gas must escape from the solution in order to re-establish equilibrium ($\zeta = 0$). In a quiescent liquid this can be a rather slow process which involves diffusion through the free surface and formation of gas bubbles that

rise through the liquid and burst at the surface. A familiar example of this is the 'going flat' of a carbonated drink that is left open, which can take a few hours. To further illustrate this example we can consider the case of Champagne wines, studied in depth by Liger-Belair [40]. In such drinks $\zeta \approx 5$ (with c_s defined at $P_s = 101$ kPa). A 0.1 l glass of Champagne contains an excess of ~ 0.6 l of gaseous CO_2 that, if left alone, will escape the liquid. Contrarily to what might be expected, it has been shown that only about 20% of the gas escapes inside the ~ 2 million bubbles of average diameter ~ 500 μm that will be formed. The other 80% leaves directly through the free surface [40], although not without help from the mixing provided by the swarms of rising bubbles.

2.1.2 Bubble nucleation

The conditions necessary for gas bubbles to nucleate have been the object of substantial debate and study. Lubetkin [62] presented a list that illustrates the variety of arguments that have been put forward to explain the discrepancies between nucleation theory and experiments. The supersaturation ratio in the Champagne example is low compared to the theoretical predictions of $\zeta > 1000$ in order for homogeneous nucleation to occur at room temperature [63]. Bubble growth below the homogeneous threshold requires the pre-existence of gas pockets [64] (nucleation sites) with a radius equal to or larger than a critical value

$$R_c = \frac{2\sigma}{P_s \zeta}, \tag{2.3}$$

with σ the surface tension of the gas-liquid interface. This value is obtained by equating the concentration of gas in the liquid bulk (which immediately after supersaturation is equal to c_0) to the gas concentration at the surface of the gas pocket, given by $c_b = k_H(P_s + 2\sigma/R)$. The second term in the parenthesis is the Laplace pressure jump due to a curved interface. A smaller gas pocket will dissolve quickly since the concentration on its surface exceeds c_0, causing an unfavourable concentration gradient. Larger ones, on the other hand, will induce a diffusive flow of the dissolved gas towards them and hence grow. In principle, nucleation sites might be provided by suspended particles, crevices in the container or free small bubbles. However, the latter are not stable. An undisturbed liquid which is left to rest will soon get rid of free bubbles either by dissolution or by growth and flotation [36].

2.1.3 Our experimental set-up

It is our intention to study the growth of gas bubbles in a liquid with supersaturation $\zeta < 1$, where bubble growth times are expected to be long. To our knowledge, there exist no previous experimental studies of diffusive bubble growth under such

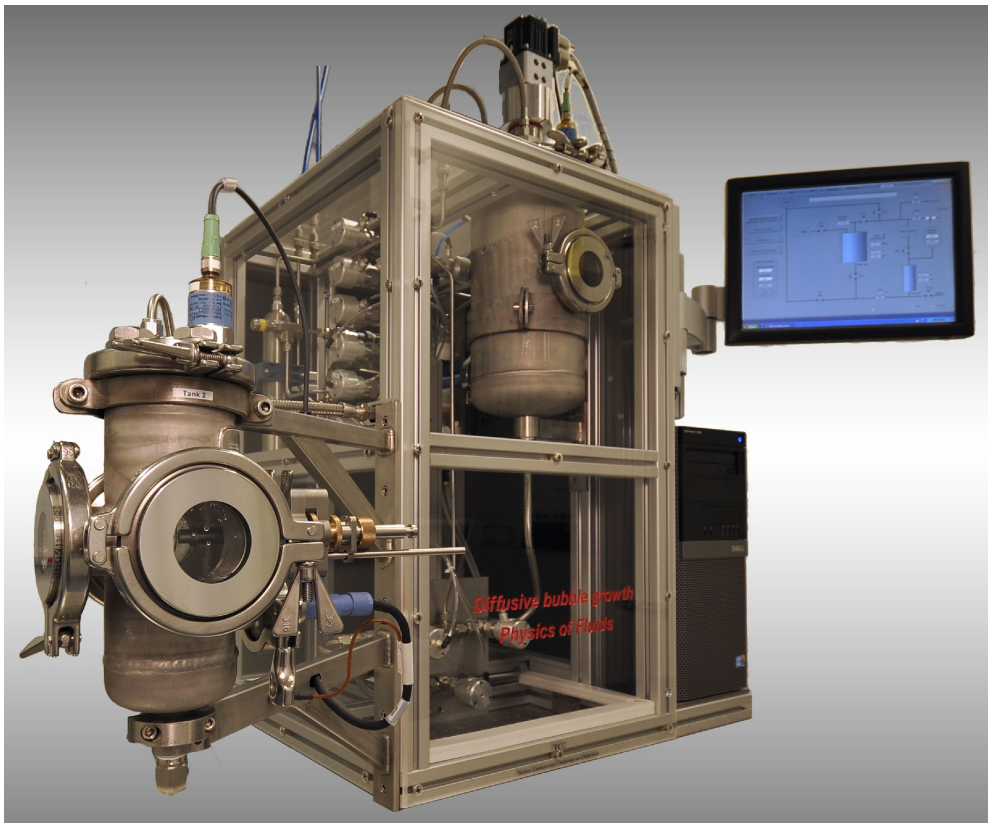

Figure 2.1: Photograph of the experimental system. The reservoir tank is located on the right-hand side and inside the frame. The observation tank is outside the frame in order to allow positioning of lights and cameras. The height of the frame is about 90 cm.

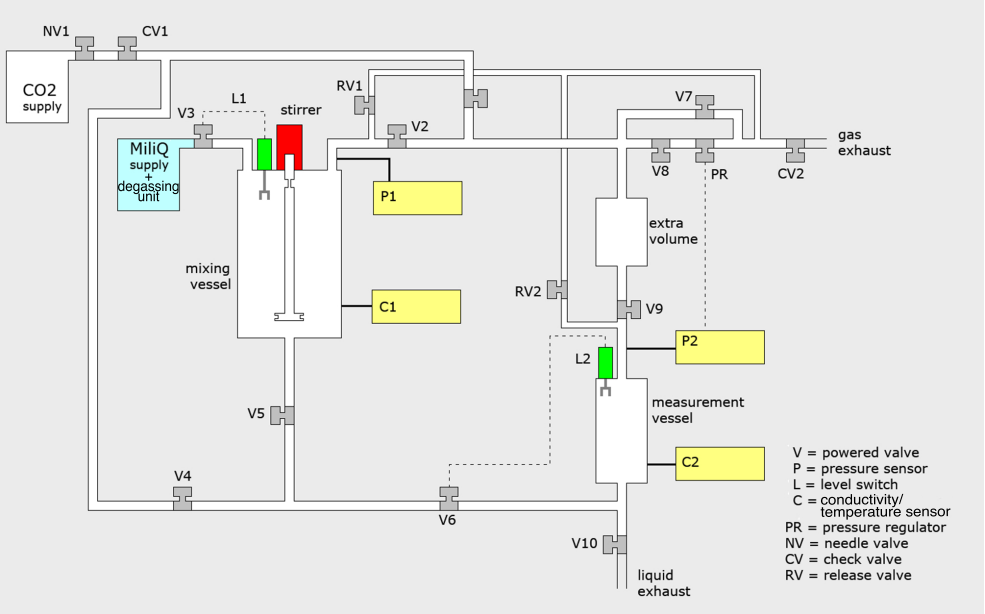

Figure 2.2: Scheme of the setup indicating the location of valves, pressure controllers, and sensors. Here the position of the tanks is reversed with respect to the picture shown in figure 1.

conditions. Previous studies have used values of $\zeta \sim 2$, which is comparable to the supersaturation of carbonated soft drinks [35,38,65]. We shall probe the limit of very slow degassing, first to observe the growth of a single bubble and then how bubbles interact when growing in mutual proximity while 'competing' for a limited amount of available gas.

In this chapter we describe an experimental system (fig.2.1) designed to prepare a saturated solution and then supersaturate it by slightly decreasing its pressure (sections 2.2.1 through 2.2.5). It is through accurate pressure control that we can achieve and maintain the small supersaturations desired for the experiments. Bubbles then grow in pre-determined positions provided by crevices in a specially prepared surface (sections 2.2.6 and 2.2.7). This technique allows us to control the number of bubbles and the distance between them as we image their evolution digitally (section 2.2.8). Finally, in sections 2.3 and 2.4 we present the results of performance tests and the outlook of the experimental studies to be performed in the future.

2.2 Experimental set-up description

2.2.1 Stainless steel tanks

The system (figures 2.1 and 2.2) is composed of two stainless steel tanks with volumes of 7 and 1.3 liters respectively. The larger one serves as a reservoir where a solution of water saturated with gas can be prepared and stored. This mixture can be transferred to the smaller observation tank where the experiments in controlled bubble growth properly take place. A system of steel pipes and pneumatic valves connect the tanks to each other and to the water and gas sources as well as to the drainage system of the lab.

The tanks were manufactured from 3161 stainless steel (Het Noorden, Gorredijk, The Netherlands), and are certified for a working pressure of 1 MPa. The reservoir (figure 2.3) has a lateral flanged port for fitting a temperature/conductivity sensor (section 2.2.4), a lateral viewing window made of metal-fused glass (Metaglas, Herberts Industrieglas), and a fluid inlet/outlet at the bottom. The plate that covers the top of the tank has fittings for a magnetic stirrer head (Macline mrk12, Premex Reactor AG), a level switch (Liquiphant FTL20, Endress+Hausser Inc.), a water inlet, and a gas inlet/outlet.

If we were to rely on natural diffusion for preparing the mixture of water saturated with gas, experimental waiting times would be extremely long. Hence, the reservoir tank is equipped with the aforementioned magnetic stirrer attached to a 285 mm gassing propeller (BR-3, Premex Reactor AG) and powered by an external motor (Smartmotor SM2315D, Animatics Corp). Figure 2.4 shows how the mixer accelerates the saturation process. Rotation of the propeller blades creates a low pressure region around them. As a result, gas is sucked into the hollow stirrer axis and blown into the liquid through holes at the end of the propeller blades. With this system, the preparation of seven liters of saturated water takes less than one hour.

The observation tank (figure 2.5) has two lateral flanged ports: one for a temperature/conductivity sensor like the reservoir, and the other for introducing a specially designed tweezer (see section 2.2.7) designed to hold the substrates with nucleation sites for bubble growth. This tank has three viewing portholes also made of metal fused glass. These windows sit at 90°angles from each other and allow for illumination and visualization of experiments (see section 2.2.8). The cover holds a level switch and a gas inlet/outlet. Water enters and exits through the bottom of the tank.

2.2.2 Liquid and gas sources

Although in principle any transparent liquid-gas combination could be studied using this setup, the only configuration used up to now and in upcoming experiments is water with carbon dioxide. This mixture is convenient due to the high solubility of

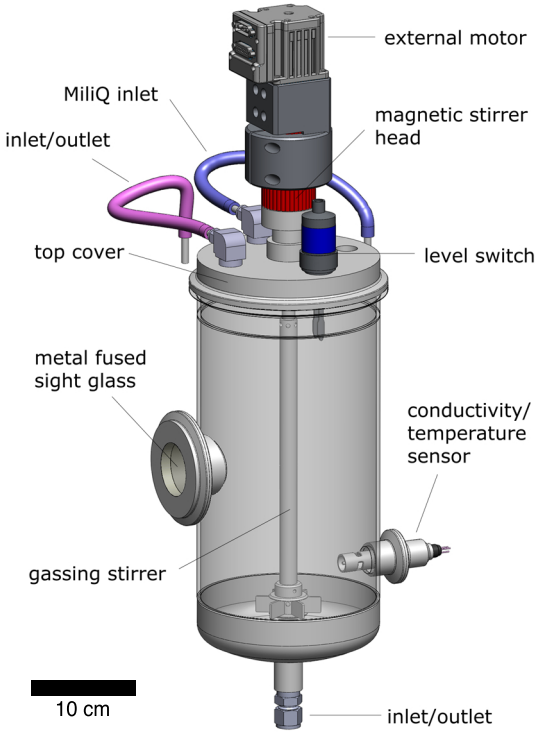

Figure 2.3: The stainless steel reservoir tank used for preparing and storing a saturated mix of H_2O and CO_2 at a maximum overpressure of 10 bar.

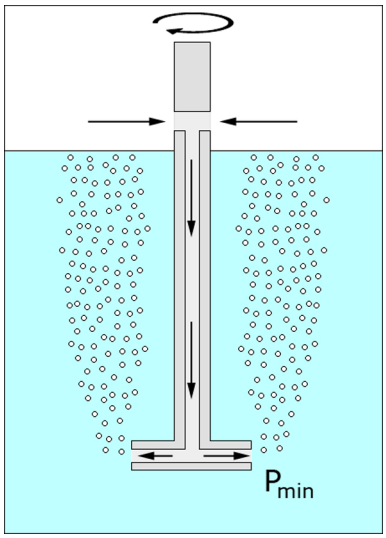

Figure 2.4: Sketch of the gassing mixer used. The rotation of the propeller blades creates low pressure zone. As a result, CO_2 is sucked into the hollow stirrer axis and bubbled into the liquid through the end of the propeller blades

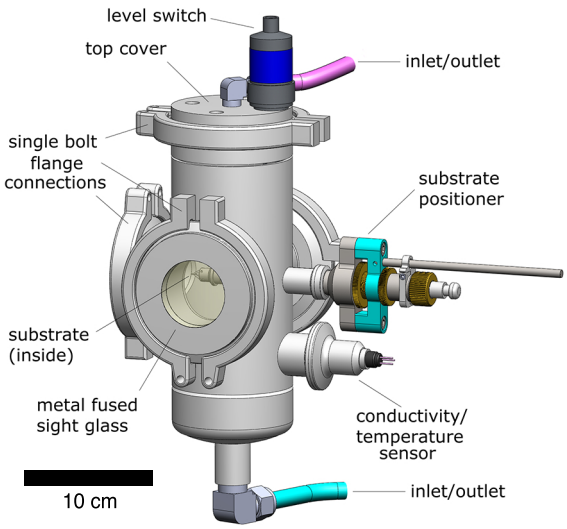

Figure 2.5: The stainless steel observation tank. Part of the saturated mixture from the reservoir is transferred to this tank to be supersaturated by dropping the pressure in a controlled way. Bubbles grow on a sample held by the substrate positioner. The process is visualized through the windows.

CO_2 in water ($\sim 1.6\ g_{CO_2}/kg_{H_2O}$ at $T = 20°C$ and $P = 0.1$ MPa) compared to other gases.

We use ultra-pure water (MilliQ A10, Millipore) degassed in line by a vacuum pump (VP 86, VWR) coupled to a degassing filter (Millipak 100). The CO_2 is provided by Linde Gas with 99.99% purity.

2.2.3 Pressure control

As stated in Henry's Law, the quantity of a gas that can be dissolved into a liquid is directly proportional to the partial pressure of the gas above the liquid. The proportionality constant (Henry's constant) reflects the solubility of the gas-liquid pair and is a function of temperature. Therefore, by altering either pressure or temperature of a saturated solution it is possible to take it to an under or supersaturated state. In our experiments, we control supersaturation by dropping the pressure in the observation tank and keeping the temperature constant.

The pressure at which the liquid is saturated in the mixing tank is controlled through a regulator on the CO_2 line of the laboratory which has a maximum working pressure of 1 MPa. The value inside the tank is measured with a pressure transmitter (Midas C08, Jumo GmbH) which is read out by a multiparameter transmitter (eco-Trans Lf03, Jumo GmbH) that communicates with the general control interface (see section 2.2.5)

The pressure in the observation tank is measured and controlled by a pressure regulator (P-502C, Bronkhorst) and flow controller (F-001AI, Bronkhorst). The pressure regulator has a pressure range of 0.02-1 MPa with a measurement error of 5 kPa. The flow controller has a working pressure range of 0.1-1 MPa and its flow range is 10-500 ml/min. Since this type of control is based on a certain controlled volume, an extra volume of 500 ml is placed between the measurement vessel and the flow controller to permit a smooth regulation of the pressure. Figure 2.6 shows the pressure in the observation tank during a bubble growth experiment (see section 2.3.2) where the pressure is dropped from an initial saturation state and kept constant as the solution degasses.

2.2.4 Monitoring concentration

Carbon dioxide reacts with water to form carbonic acid (H_2CO_3) which is unstable and dissociates into roughly equal amounts of hydrogen (H^+) and bicarbonate (HCO_3^-) ions. The amount of each chemical species and their molar conductivity will determine the general conductivity of the solution [66]. This property is used to monitor the concentration of CO_2 during the saturation process in the mixing tank. For preparing the solution, the water filled tank is pressurized with CO_2 and the mixer turned on. The rise in conductivity is immediately detected by the sensor and it satu-

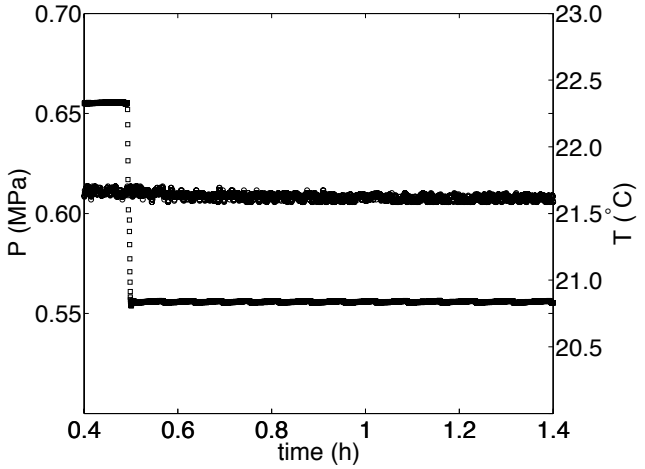

Figure 2.6: Example of a time series of pressure (squares) and temperature (circles) measurements in the observation tank during an experiment. The pressure was decreased by 0.1 MPa from the saturation condition, and kept at a constant value afterwards.

rates after some time. Measuring this property, therefore, serves as an indicator that saturation has been reached. It is assumed that after 10 minutes of measuring a stable conductivity value the desired state is achieved (see section 2.3.1).

In the case of the observation vessel, the measurement of conductivity serves as a qualitative indicator of the amount of CO_2 present in the mix. Upon de-pressurization gas diffuses out of the solution. In the absence of significant mixing -as is the case during experiments- the main mechanism of gas exsolution is diffusion out of the free surface. Therefore a concentration gradient is established through the mixture and the conductivity measurement close to the bottom of the tank is no longer representative of the overall concentration of CO_2.

Conductivity and temperature of the liquid in both vessels are measured with 2-electrode conductivity sensors with integrated Pt100 temperature probes (Condumax CLS16, Endress+Hausser Inc.) located near the bottom of each tank (fig.2.2). Knowing the temperature during experiments is necessary in order to correctly quantify the amount of supersaturation by knowing the correct value of Henry's constant. To avoid significant temperature variations, a hose (not shown in fig.2.1) is wrapped around both thanks, through which water circulates at a temperature controlled with a refrigerated/heated circulator (Julabo, F25HL). Figure 2.6 shows the temperature in the observation tank during an experiment.

2.2.5 Control and user interface

The elements of the experiment that require electronic control are the magnetic stirrer, the level switches, the pneumatic powered valves and the flow regulator used for gradual pressure release. Control of these elements, together with data acquisition of the sensors, is done through a combination of programmable logic controllers (PLCs) (BC9120, Bus Terminal Controller, Beckhoff) and a graphical user interface built in National Instruments LABVIEW which communicates with the PLCs and the data transmitters from the sensors.

2.2.6 Substrates for bubble nucleation

Controlling the positions where bubbles grow is of paramount importance for studying the interaction of bubbles growing near each other as they 'compete' for the gas available in dissolution. For this purpose we use silicon wafers of area around 1 cm^2 with micron sized pits (of radius $R_{pit} = 10-50$ μm and depth ~ 30 μm) that function as nucleation sites. The substrates are fabricated in a clean room using soft lithograpy and Reactive-Ion-Etching (RIE) techniques which allow to create pits with a minimum diameter of a couple microns and depths of a few tens of microns. In order to ensure that gas will be entrapped inside the pits after being submerged in water, the last step in the micro-manufacturing process is to create a super-hydrophobic 'black silicon' [67] structure in the bottom of the pits. This guarantees that the air pockets in the cavities will be stable and henceforth work as nucleation sites for bubbles to grow upon de-pressurization. The feasibility and stability of such hydrophobic cavities as nucleation sites has been successfully tested by Borkent *et al.* [68].

2.2.7 Substrate holder

The substrates are introduced and held in the observation tank using the holder shown in figure 2.7. This device keeps the substrate at a level where it is visible through the windows and separated (~ 5 cm from the walls, in order to avoid interaction with bubbles that might grow there. It consists of a set of tweezers ('substrate gripper' in the figure) with one fixed and one mobile lever. The mobile one is actuated via the push button on the right-hand side and a spring mechanism that runs inside the central pin and keeps it in a closed position by default. The central pin can be slid back and forth and rotated by hand by loosening the conical clamping nut which will keep it fixed against the pressure in the tank. The clamping and adjustment bolts allow for a fine positioning along the direction of the parallel pin on which the guiding taper bush is mounted.

The substrate is mounted on the tweezers outside the tank and then introduced through a flanged port (see figure 2.5) and secured with a single-bolt clamp. In this

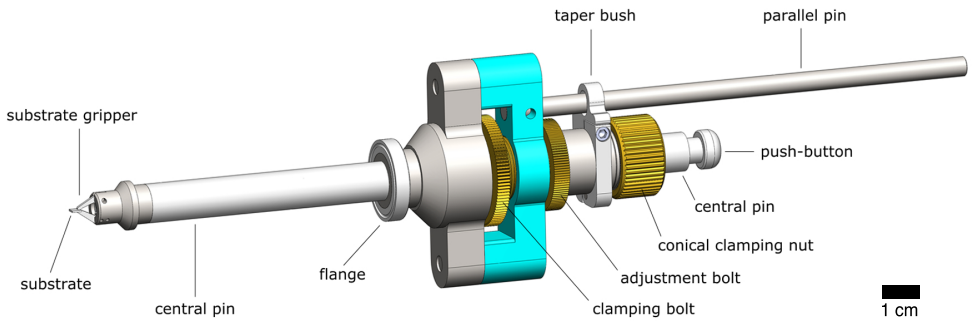

Figure 2.7: The substrate holder. The section to the left of the flange is introduced in the observation tank. The bolts on the right hand side are used to adjust the position of the substrate from outside the tank and keep it fixed firmly against the high pressure inside. The substrates can be held horizontally, vertically or at any angle in between by rotating the central pin.

and all other flange connections, o-rings are used to ensure the water and air tightness of the system.

2.2.8 Visualization

Images are taken using a long distance microscope objective (K2/SC, Infinity) with a maximum working distance of 172 mm and a CCD camera (Flowmaster, LaVision) with a resolution of 1376 x 1040 pixels. When experiments are done with the substrate in a horizontal position diffuse backlighting is used. If the substrate is held vertically light is reflected onto it though a half mirror in front of the microscope.

2.3 First experiments

2.3.1 Preparing a saturated solution

Firstly, we have tested how effective our system is for preparing a saturated water-CO_2 mixture and to what extent the measurement of conductivity serves as an indicator of the concentration. As mentioned in section 2.2.4, CO_2 in water dissociates according to

$$CO_{2(aq)} + H_2O \longleftrightarrow H^+ + HCO_3{}^-, \tag{2.4}$$

with overall dissociation constant $K_1 = 4.22 \times 10^{-7}$ at 21°C. The molar conductivities (Λ_i^o) of the hydrogen and bicarbonate ions and their concentrations will determine the conductivity of the solution. The contributions of the dissociation of H_2O

and HCO_3^- can be safely neglected. Hence, the conductivity (S) can be calculated as:

$$S = (\Lambda^{o}_{H^+} + \Lambda^{o}_{HCO_3^-})K_1[CO_{2aq}], \tag{2.5}$$

where the concentration of carbon dioxide $[CO_{2aq}]$ is expressed in $\mathrm{mol/m^3}$, $\Lambda^{o}_{H^+} = 348.22 \times 10^{-4}\ \mathrm{Sm^2/mol}$ and $\Lambda^{o}_{HCO_3^-} = 40.72 \times 10^{-4}\ \mathrm{Sm^2/mol}$ at 21°C. Such a way of determining the conductivity is expected to work only for low concentrations of dissolved CO_2, since due to its weak acidity, the ion concentration is not necessarily linear with $[CO_{2aq}]$ [66].

Tests were performed by filling the reservoir tank with water, leaving about 3 cm of head space for gas. Subsequently, and after the pressure regulator of the gas line had been set to the desired pressurization value, the CO_2 inlet valve was opened. At this time we also started the mixing propeller with a speed of 900 rpm so that CO_2 is forced into the liquid through the mechanism described in figure 2.4. The gas inlet valve is kept open throughout this procedure in order to keep the pressure rising as gas dissolves into the liquid. We monitored the conductivity measurement of the sensor as it rose throughout the process. When its value did not change for 10 minutes we considered the solution to be stable, which was achieved after around 30 minutes of mixing as shown in figure 2.8. Henry's constant was computed using the van 't Hoff equation for its temperature dependence: [69]

$$k_H(T) = k_H(\Theta)\exp\left[C\left(\frac{1}{T} - \frac{1}{\Theta}\right)\right], \tag{2.6}$$

where Θ is the standard temperature (298 K) and $C = 2400$ K for the case of CO_2 [70]. The temperature during experiments, T was ≈ 21°C, giving $k_H = 3.79 \times 10^{-7}\ \mathrm{mol/kg \cdot Pa}$. We then use Henry's law to calculate $[CO_{2aq}]$ at the experimental pressure, and introduce this value into equation 2.5 to calculate the conductivity. Figure 2.9 shows the measured and the calculated values for saturation (absolute) pressures going from 2 to 11 bar. Agreement is very good until around 9 bar, when presumably the concentration of CO_2 can no longer be considered as low, compared to the atmospheric concentration treated in [66].

2.3.2 Growing bubbles

After making sure that our method to prepare the saturated solution is effective, we tested the bubble growing process from a single cavity and a pair of cavities. The typical procedure of an experiment is the following: the whole system is flushed with CO_2 in order to expel atmospheric gasses. A saturated solution is prepared in the reservoir tank and part of it is transferred to the observation tank where the substrate with artificial nucleation sites was previously mounted on its holder. The filling is done by first pressurizing the tank to the same level as the reservoir in order to avoid

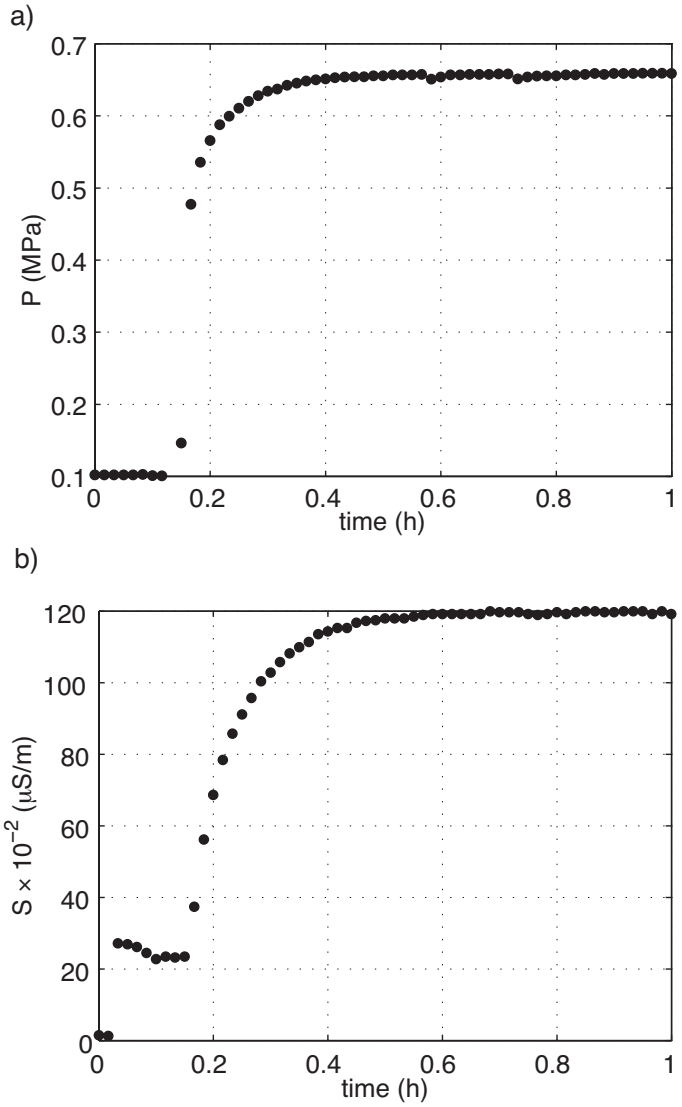

Figure 2.8: Pressure (a) and conductivity (b) in the reservoir tank during the filling, pressurizing and mixing of the solution until saturation. The first jump of the conductivity corresponds to the immersion of the sensor in water as the reservoir is filled. Once full, the pressurization and mixing start. The solution reaches saturation after about half an hour.

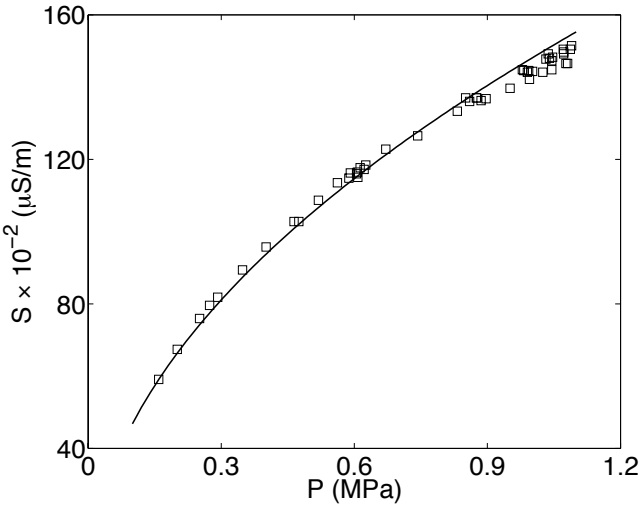

Figure 2.9: Conductivity of the saturated $H_2O + CO_2$ solution. Squares are the values measured by the conductivity sensor after the preparation procedure. The solid line is obtained with equation 2.5.

a sudden, high pressure inflow of (supersaturated) water. The valves that connect the bottom of the two tanks (V5 and V6 in fig.2.2) are then open. Water flows slowly into the observation tank driven by the slightly higher positioning of the reservoir. The level switch (L2) closes the valves, thus ensuring that the tank is always filled to the same level. After this procedure we wait for half an hour to let water become completely stagnant. Then the experiment can start.

The mix in the observation tank is supersaturated by reducing the pressure of the gas above it. Since we want to study diffusive growth without effects like inertia or streaming which appear when bubbles grow quickly in succession as in the case of, *e.g.*, Champagne [40], the pressure is dropped only 5 to 20% from the absolute saturation pressure, giving a corresponding range of supersaturation $\zeta = 0.05 - 0.25$. The critical radius (eq. 2.3) for a gas pocket to grow under the smallest ζ considered is ~ 5 µm, which means that hydrophobic pits of radius $10 - 50$ µm are very well suited as nucleation sites under our experimental conditions.

Figure 2.10 shows a bubble growing from a pit with a 10 µm radius after a pressure drop from 6.5 to 6 bar and figure 2.11 shows its radius as a function of time. The size at which the bubble detaches is determined by a competition between buoyancy pulling upwards and surface tension, pulling downwards. It is known as the Fritz

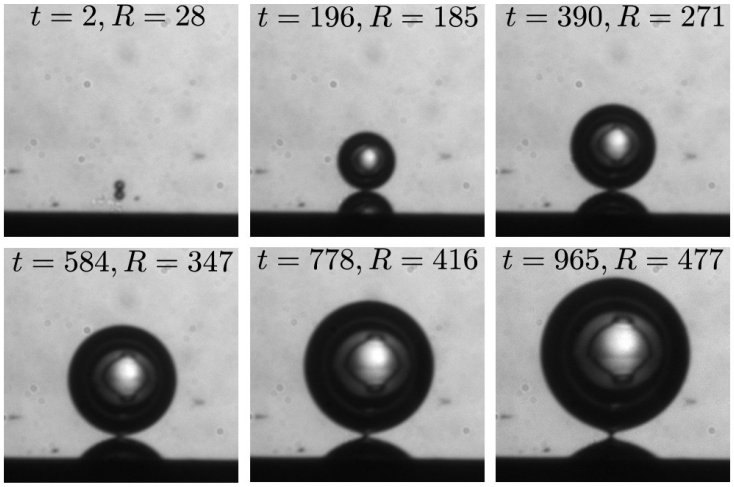

Figure 2.10: Bubble growing on a substrate positioned horizontally with a single pit of radius 10 μm after a pressure drop from 0.65 to 0.6 MPa corresponding to a supersaturation $\zeta = 0.08$. Time is expressed in seconds and radius in micro meters.

radius [71] and for a spherical bubble is given by:

$$R_{Fritz} = \left(\frac{3}{2} \frac{\sigma R_{pit}}{\rho g} \right)^{1/3}. \tag{2.7}$$

The last observed radius of the bubble in figure 2.10 before detachment was $\sim$ 477 μm which is ~ 5 μm larger than the Fritz value for such a pit (with $\sigma = 0.069$ N/m due to the presence of CO_2). The discrepancy is about 1% and could be due to the fact that the tracking method assumes a spherical bubble, and at this point the latter is slightly deformed, or to small deviations in the pit's radius. However, regardless of the cause, this is the maximum error incurred in the image processing, which we consider acceptable.

Two interesting things can already be pointed out from figure 2.10. The first is the fact that the bubble took more than 15 minutes to grow to a radius of ~ 0.5 mm, which makes it a safe assumption to say that the only mass transfer mechanism present was diffusion. The second is that its growth was much slower than the solution of Epstein and Plesset [72] for a bubble growing under such supersaturation, which, as expected from diffusive processes predicts a $R \sim \sqrt{t}$ evolution. Their solution assumes an unbounded bubble in an infinite medium, so the slowing down is probably due to the presence of the substrate where the nucleation site is located. This feature will be studied systematically with the present apparatus.

After the bubble detaches, another one starts growing from the same place. As far as we have observed, this sequence continues for at least 12 hours. The amount

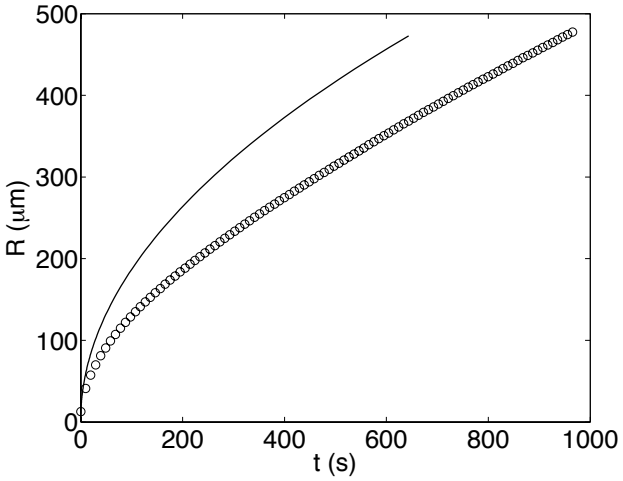

Figure 2.11: Radius evolution of the bubble shown in figure 2.10 ∘ experimental measurements, — theoretical solution for a bubble growing by gas diffusion in an unbounded medium.

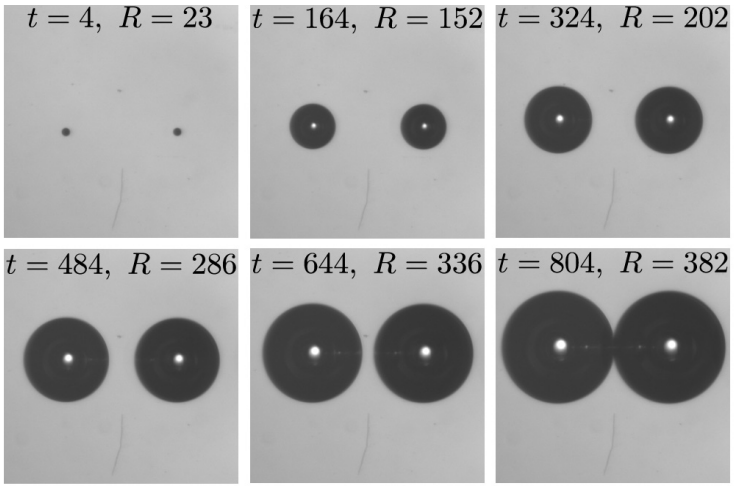

Figure 2.12: Two bubbles growing on a substrate positioned vertically with two pits of radius 10 μm, separated 760 μm after a pressure drop from 0.65 to 0.6 MPa. Time is expressed in seconds and radius (values correspond to left-hand bubble) in micro meters.

of undesired bubbles growing on the walls of the tank is small, which means that the water is mainly degassing by diffusion through the gas-water interface above. The stratification provoked by the escape of CO_2 from the surface is gravitationally stable and therefore will not give rise to density-driven convection unlike the opposite case of an undersaturated liquid pressurized with gas from above [73]. This considered, with the nucleation site sitting ≈ 15 cm below the surface, and the diffusivity of CO_2 in water being $D = 1.97 \times 10^{-9}$ m^2/s, the time for the diffusive penetration length ($\delta_d = 2\sqrt{Dt}$) to reach the bubble site should be about 1 month. In practice, the local concentration around the nucleation site will eventually drop to a level where the radius of the pit is less than R_{crit} and the site will become inactive. However, we expect that the bubble growth sequence can continue for a couple of days after the initial pressure drop.

Finally, we have tested the case of two bubbles growing close to each other. Figure 2.12 shows two nucleation sites, separated 760 μm from which bubbles grow after an equal pressure drop to figure 2.10. In this case the substrate was positioned vertically and lit from the front through a half mirror. The growth of the pair of bubbles is slightly slower than the single bubble case, suggesting that each one of them influences the growth rate of the other.

2.4 Summary and outlook

We have developed an experimental system with which bubble growth by gas diffusion can be studied quantitatively. The method used to prepare a saturated solution of CO_2 in water by pressurizing and mixing in a reservoir tank while monitoring the electrical conductivity has been shown to be effective. The position of bubbles growing when the solution is supersaturated by dropping its pressure can be accurately controlled using hydrophobic pits on silicon wafers. First experiments with a single bubble and a pair of them suggest that diffusion is indeed the only mass transfer mechanism in action.

The next step is to take a close look at the sequential growth of bubbles from a single nucleation site in order to understand the differences with the growth of an unbounded bubble. Afterwards we will investigate how multiple bubbles interact when growing in close proximity under low supersaturation conditions.

3

The quasi-static growth of CO_2 bubbles *

We study experimentally the growth of an isolated gas bubble in a slightly supersaturated water-CO_2 solution at 6 atm pressure. In contrast to what was found in previous experiments at higher supersaturation, the time evolution of the bubble radius differs noticeably from existing theoretical solutions. We trace back the differences to several combined effects of the concentration boundary layer around the bubble, which we disentangle in this work. In the early phase, the interaction with the surface on which the bubble grows slows down the process. In contrast, in the final phase, before bubble detachment, the growth rate is enhanced by the onset of density-driven convection. We also show that the bubble growth is affected by prior growth and detachment events, though they are up to 20 minutes apart.

*Published as: [O.R. Enríquez, C. Sun, D. Lohse, A. Prosperetti and D. van der Meer, The quasi-static growth of CO_2 bubbles, Journal of Fluid Mechanics 741, R1 (2014)].

3.1 Introduction

The diffusion-driven growth of bubbles in supersaturated liquids is a common occurrence in nature and technology. From carbonated drinks [38–42] to magmatic melts [9] or oil reservoirs [43], molten polymers and metals [22], or even the blood of whales or scuba-divers [13, 74], the appearance of gas bubbles might be anything from beneficial to completely detrimental. They may be responsible for a pleasant flavour enhancement but can also lead to volcanic eruptions or cause decompression sickness or even death.

Theories, both including [75] and neglecting [72] the advective transport induced by the radially expanding bubble interface, predict that the radius R grows proportionally to $\sqrt{t}$ (with a larger prefactor in the former case). Experimental studies using moderately supersaturated water-CO_2 solutions (corresponding to that in a carbonated beverage or beer) have confirmed such time dependence [35, 38, 39].

We perform an experimental study of the controlled growth of a single CO_2 bubble at high pressure (~ 6 atm) in a hitherto unexplored low supersaturation regime, which is an order of magnitude smaller than that of a typical carbonated beverage. In contrast to other works in the moderately supersaturated regime, we find that the concentration boundary layer around the bubble and the substrate on which the latter grows have an important influence on the growth rate.

3.2 Experimental procedure and results

In the experiment, the desired supersaturation level is induced by a small, isothermal pressure drop in a water-CO_2 solution equilibrated at pressure P_0 and temperature T_0. A suitable and controlled nucleation site is provided by a hydrophobic micro-cavity of radius $R_p = 10$ μm and depth 30 μm, etched in the center of a small rectangular silicon chip (8 mm $\times$ 6 mm). A bubble grows from the pit until buoyancy overcomes the surface tension (estimated as 61 mN/m in our conditions) that attaches it to the pit, forcing it to detach [76]. After this, another bubble grows from the same site in a process that can go on for hours. We take images with a digital camera and a long-distance microscope objective at rates of 0.5-1 Hz. The smallest bubbles resolvable with our optical resolution (~ 2 μm/pixel) had a radius of about 10 μm. Figure 3.1 shows a sketch of the experiment and a detailed description of it can be found in [28].

Figure 3.2 shows the results of two different experiments in which the pressure was reduced from the initial value $P_0 = 0.65$ MPa ($T_0 = 21.6$°C) by 0.05 and 0.1 MPa. Under these conditions it took the bubbles around 5 and 15 minutes, respectively, to detach. Their final radius, $R_{det} \approx 477$ μm, agrees with the expectation for a quasi-statically grown bubble [29].

The long detachment times and slow growth rates observed suggest that advec-

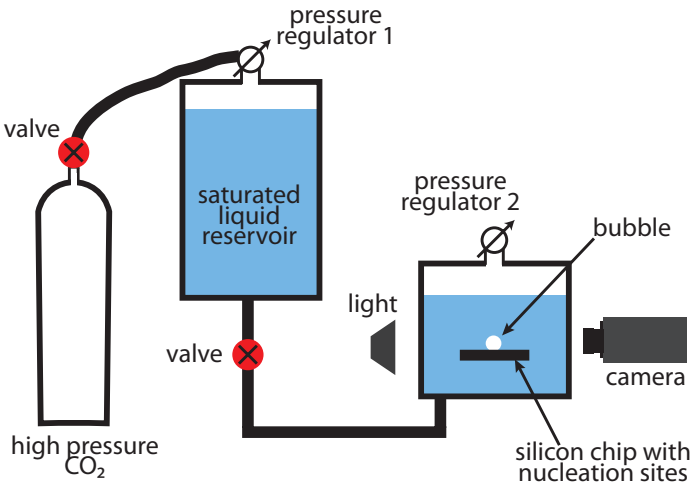

Figure 3.1: Sketch of the experimental system. A saturated aqueous solution of CO_2 is prepared in the reservoir tank and part of it transferred to a smaller observation tank. Here the mix is supersaturated by means of a small, isothermal pressure drop. In order to avoid residual currents in the observation tank, the liquid is allowed to rest for thirty minutes after filling before the pressure is dropped. Temperature is kept stable by circulating water from a refrigerated cooler through a hose wrapped around the tank (see [28]). A bubble grows from a hydrophobic micro-pit etched on a silicon wafer. The process is imaged through a window in the tank using a long-distance microscope objective with diffuse back light through a window in the opposite side.

tion caused by the moving bubble interface is negligible. However, upon comparing experimental results with the corresponding theory, significant discrepancies are evident:

- The radius is always smaller than the theoretical prediction and is not proportional to $\sqrt{t}$ (figure 3.2a).
- The derivative dR/dx, with $x \propto \sqrt{t}$, does not converge to a constant value. Instead, the experimental curves only reach a plateau at a level 20-40% lower than the theory and they take a longer time to do so (figure 3.2b). Furthermore, the growth rate of the second bubble in each case (empty symbols) differs from that of the first one (filled symbols). In figure 3.2b it becomes clear that differences are limited to the early growth stages and the two curves for each experiment eventually converge.
- Around $x \sim 20$ there is a point where dR/dx starts increasing until eventually it surpasses the maximum predicted by the standard theory summarized below.

In the remainder of this article we disentangle the causes of these differences, which are: (*i*) the presence of the silicon chip, (*ii*) a region depleted of CO_2 left behind by the previously detached bubble, and (*iii*) natural convection triggered by the density difference between liquid in the concentration boundary layer and outside. This last phenomenon stands in contrast to previous experimental studies in which its effects were not detected and therefore explicitly discounted by the authors [35, 38].

3.3 Analysis

Idealized problem

Before getting further in the discussion, let us briefly recall the idealized problem of a bubble growing in an unbounded, supersaturated gas-liquid solution as formulated by [72]. The equilibrium concentration of gas is given by $c_0 = k_H P_0$ (Henry's law), where k_H, Henry's coefficient, is a decreasing function of temperature specific for a given gas-liquid pair. Decreasing the pressure to P_s (at the same temperature T_0) leads to an out-of-equilibrium, supersaturated state. A bubble with an initial radius R_0 is placed in such a supersaturated liquid at $t = 0$. Initially, the concentration is c_0 everywhere, and far from the bubble it is assumed it will remain so. Neglecting the Laplace pressure, the gas concentration at the bubble boundary is constant and given by $c_s = k_H P_s$. For the conditions discussed in this paper, it can be shown that the influence of surface tension is limited to the very first instants of growth, so that it can be neglected throughout. The bubble remains immobile with its center at the origin of a spherical coordinate system. One can then solve the spherically symmetric

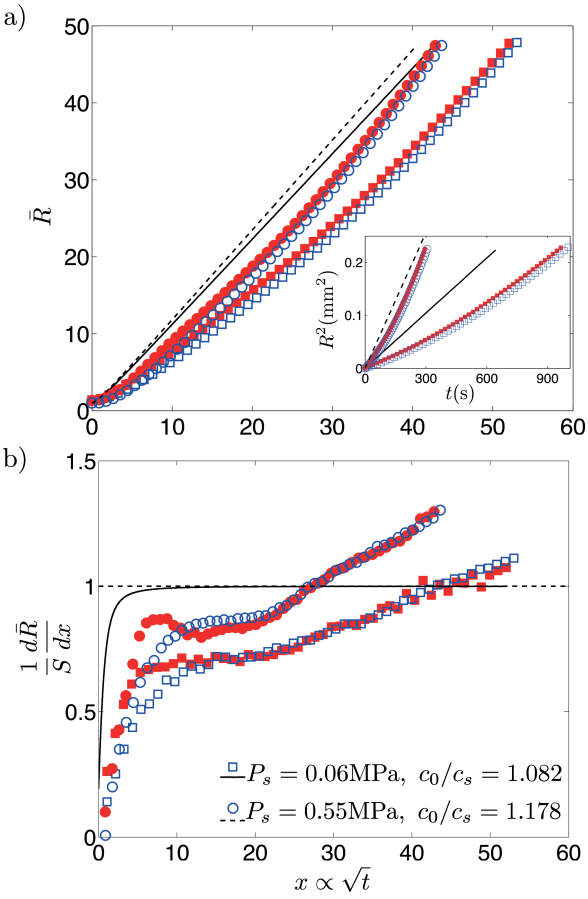

Figure 3.2: Radius (a) and its derivative with respect to $\sqrt{t}$ (b) in dimensionless form. Symbols represent experimental data. Filled ones correspond to the first bubble to emerge from the nucleation site and empty ones to the second. Circles correspond to $c_s = 9.10\,\mathrm{kg/m^3}$ and squares to $c_s = 10.01\,\mathrm{kg/m^3}$. In (a) dark lines represent the full analytical solution of eq. (3.1) for each case. The inset shows the same data and theoretical curves in dimensional form. In (b) the theoretical curves for both experimental conditions collapse to the dark solid line when they are divided by the steady state value S. The local maximum observed for the red circles corresponds to a slight initial overshoot and oscillation of the pressure controller, and therefore is not present in the second bubble. The depressurization is complete and stable at a dimensionless time around 11. For the smaller pressure drop, corresponding to the squares, the overshoot is minimal.

diffusion equation to evaluate the time evolution of the concentration gradient at the bubble surface ($r = R$). Equating the gas flow caused by this gradient to the time derivative of the bubble mass gives an expression for the quasi-static radial growth rate:

$$\frac{dR}{dt} = D\beta\left(\frac{1}{R} + \frac{1}{\sqrt{\pi Dt}}\right), \tag{3.1}$$

where $\beta = (c_0 - c_s)/\rho$, $D = 1.97 \times 10^{-9}\ \mathrm{m}^2/\mathrm{s}$ is the diffusivity of CO_2 in water and $\rho \approx 10\ \mathrm{kg/m}^3$ is the density of the gaseous phase at P_s. Equation (3.1) can be conveniently expressed in terms of the dimensionless variables $\bar{R} = R/R_p$ and $x = \sqrt{(2D\beta/R_p^2)t}$, where R_p is the radius of the nucleation site. In the original formulation R_0 was used as a length scale; but as this quantity is not defined in the present experiment, we use R_p. Although the full analytical solution to the equation can be obtained [72], the asymptotic solution:

$$\bar{R} \approx \left[\gamma + \left(1 + \gamma^2\right)^{1/2}\right] x \equiv Sx \tag{3.2}$$

valid when $\bar{R} \gg 1$ and $x \gg 1$, is a very good approximation. The constant γ is defined as $\gamma = \sqrt{\beta/2\pi}$. The solid line in figure 3.2b shows $d\bar{R}/dx$ for the complete solution, normalized by its asymptotic value, S, given by the terms inside the brackets in eq. (3.2). We can see here how quickly the full solution to eq. (3.1) converges to this long-term solution (horizontal dashed line in figure3.2b).

Note that the initial time $t = 0$ of the Epstein-Plesset theory is slightly shifted with respect to the one used in plotting our figures due to the different initial conditions. We could define a virtual initial time by fitting a square-root behavior to the first few data points, but we do not pursue this possibility as its influence is very small in comparison with the major differences between theory and experiments that are apparent in figure 3.2.

As the bubble grows, the boundary layer, across which there is a concentration gradient from c_s to c_0, also grows. Its thickness δ (from the bubble surface) grows proportionally to $\sqrt{Dt}$ and soon becomes of the order of, or larger than, the bubble itself [72]. The assumptions made for the theory imply that $\delta = 0$ at $t = 0$.

We are now in a position to address the issues (*i*) to (*iii*) mentioned before.

i. The role of the silicon chip

A clear difference between theory and experiments is that in the latter bubbles grow on a substrate instead of an unbounded medium. This reduces the area available for mass transfer through two effects. First, the bubble is no longer a full sphere, but rather a spherical cap pinned to the perimeter of the nucleation site [35, 38, 39]. An area equal to the opening of the pit will always be excluded. While such exclusion

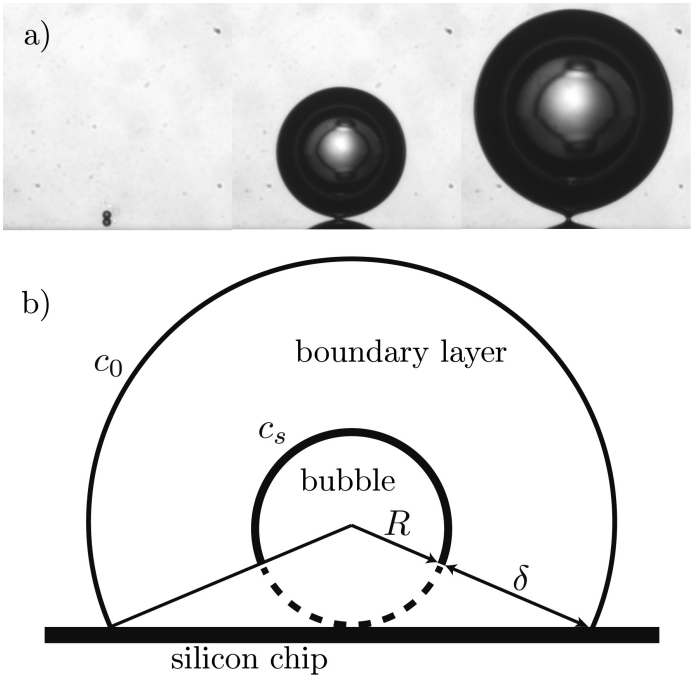

Figure 3.3: (a) Images of a growing bubble at $t \approx 1,\ 152$ and 295 s with $R = 20,\ 307$ and 474 μm. In the first snapshot, the mirror image of the bubble on the silicon surface is clearly seen below the real bubble. In the other two frames only a small fraction of the reflection is visible. Before dropping the pressure and after each bubble detaches the gas pocket is completely inside the pit and therefore not visible at all. (b) Sketch to illustrate the interaction of the concentration boundary layer with the silicon substrate. The excluded bubble area (dashed line) is estimated using the cone formed by the center of the bubble and the intersection of the boundary layer (shown by the bigger sphere) with the silicon chip.

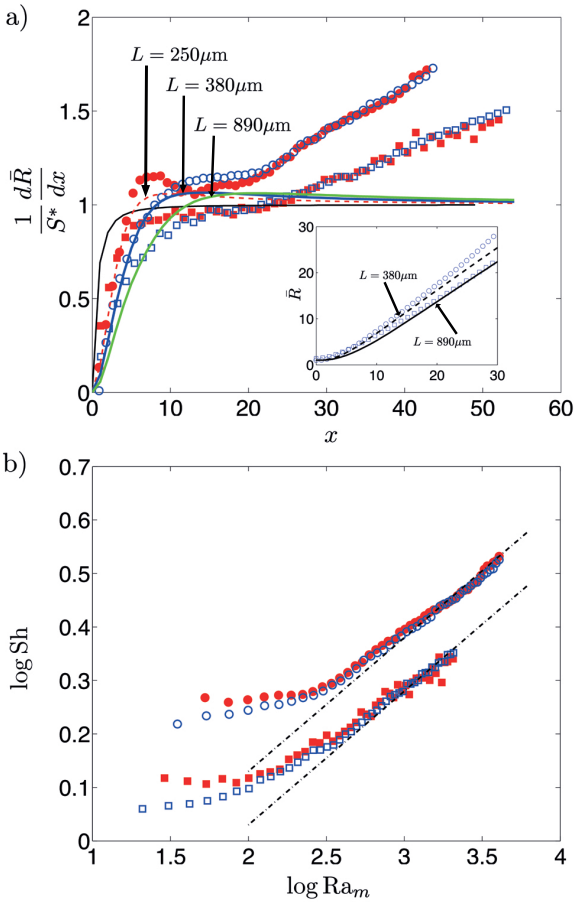

Figure 3.4: (a) Experimental $d\bar{R}/dx$ rescaled with S^*. Again, circles correspond to $c_s = 9.10\,\mathrm{kg/m^3}$ and squares to $c_s = 10.01\,\mathrm{kg/m^3}$ whereas filled symbols correspond to the first and open ones to the second bubble growing in each experimental condition. Corrections for effective diffusion area (solid black curve) and pre-existing boundary layers for the first (red, dashed curve) and the second bubbles in both experimental conditions (blue ($c_s = 9.9\,\mathrm{kg/m^3}$) and green ($c_s = 9.1\,\mathrm{kg/m^3}$) curves). The inset shows the measured time evolution of $\bar{R}$ for the second bubble of both experimental conditions together with its corresponding corrected curve. (b) Sherwood number (eq. (3.5)) as a function of the mass transfer Rayleigh number. The lines have a slope of $1/4$, which indicates that density driven convection develops around the bubble.

might be significant for a small bubble, by the time $\bar{R}$ equals 5, it represents only one hundredth of the bubble surface area (see figure 3.3a). Hence, this effect can be considered minimal over the course of the entire bubble lifetime, and clearly it cannot account for the 20-40% reduction observed in the plateau value of $d\bar{R}/dx$ (figure 3.2b).

The second effect is that the substrate acts like a barrier which hinders mass transfer into the bubble. This can be qualitatively estimated by removing the mass diffusing across the dashed portion of the bubble surface shown in figure 3.3b, where the larger sphere denotes the edge of the boundary layer of thickness $\delta = \sqrt{\pi Dt}$. A simple geometrical calculation shows that the remaining "effective" area of the bubble is given by

$$A_{\text{eff}} = 4\pi R^2 \left(1 - \frac{1}{2}\frac{\sqrt{\pi Dt}}{R+\sqrt{\pi Dt}}\right) \equiv 4\pi R^2 f_A \tag{3.3}$$

If we repeat the process to derive eq. (3.1) using the diffusion over an area A_{eff} instead of over the full bubble surface area, we recover that same equation multiplied by f_A, the factor inside the parenthesis in eq. (3.3). An asymptotic solution can be readily found for the equation, namely

$$\bar{R} \approx \left[\gamma + \left(\frac{1}{2} + \gamma^2\right)^{1/2}\right] x \equiv S^* x, \tag{3.4}$$

where the new term inside the parentheses, S^*, is smaller than S for the unbounded case. In spite of the crude approximations that go into deriving eq. (3.4), the numerical solution to the area-corrected equation (solid and dashed black curves in figure 3.4a) show markedly better agreement with experiments in the range $x = 0 - 20$.

It is worth noting that another difference with respect to the idealized problem is that by remaining in contact with the silicon chip, the bubble is effectively moving upwards. However it does so at a very small speed, equal to the radial expansion of the bubble ($\dot{R}$). In our experiments, the Péclet number ($\text{Pe} = 2R\dot{R}/D$) during the diffusive growth regime (plateau in the curves in figure 3.2b) has values of approximately 0.1 and 0.3, respectively, ruling out the possibility that the bubble translation has a significant effect.

ii. CO_2 depletion

Upon detaching, the first bubble leaves behind a region depleted of CO_2, slowing down the growth of the second bubble. This is shown as a delay in reaching the plateau value in the $d\bar{R}/dx$ curve (figure 3.2b). Although this phenomenon was considered by [35] and related to the time it takes the following bubble to nucleate, alterations in the growth rate after nucleation were not reported. We introduce the

effect of an initially depleted zone into the theoretical model by modifying the initial condition of uniform concentration everywhere to a linear gradient in the radial direction from c_s at $r = R$ to c_0 at $r = L > R$ and uniform concentration farther away. The resulting equation for dR/dt is then solved numerically with L as a fitting parameter which is adjusted to match the experimental curves. We found that $L \approx 350$ and 890 μm (figure 3.3a) match the observed slowing down of the respective second bubble growth for the two experimental conditions. Subsequent bubbles, until around the tenth, grow with only minor differences with respect to the second one, which suggests that conditions in the system quickly settle to an approximately steady state. After the tenth bubble (1-3 hours into the experiment), the plateau value of the derivative starts to decrease, indicating that the progressive loss of CO_2 in the bulk of the liquid starts to have a noticeable effect on the system.

As shown in figure 3.4a, fitting of the first bubble growth rate also requires a non-zero value of L, namely $L \approx 250$ μm. A likely explanation is related to the fact that the pressure drop from P_0 to P_s takes place over 30 s. It is conceivable that during this time a concentration gradient of thickness $\sim \sqrt{D \times 30\text{ s}} \simeq 243$ μm will develop above the pit and hence modify the "effective" initial conditions for the growing bubble.

iii. The onset of natural convection

Finally, we address the transition upward from the plateau value of the $d\bar{R}/dx$ curves (figure 3.2). We conjecture that this increase is due to the onset of buoyancy-driven convection near the bubble caused by the decrease of the density of the solution with decreasing concentration. To support this hypothesis, we recast the experimental data in terms of the Sherwood and Rayleigh numbers:

$$\mathrm{Sh} = \frac{2Rh}{D} = \frac{2R\dot{R}}{D\beta} \tag{3.5}$$

$$\mathrm{Ra}_m = \frac{g\lambda_c(c_0 - c_s)(2R)^3}{\nu D} \tag{3.6}$$

where $h = \rho\dot{R}/(c_0 - c_s) = \dot{R}/\beta$ is the mass transfer coefficient, g is the acceleration of gravity, $\lambda_c = 5.9 \times 10^{-4}$ m^3/kg is the concentration expansion coefficient of the solution and $\nu = 10^{-6}$ m^2/s is the kinematic viscosity. For natural convection around a sphere in an infinite medium it is known that $(\mathrm{Sh} - \mathrm{Sh}_p) \propto \mathrm{Ra}_m^{1/4}$ [77], with the constant $\mathrm{Sh}_p = 2$ accounting for pure diffusion. We replot our data in this form (figure 3.4b). The figure shows that initially the Sherwood number is constant, corresponding to diffusive mass transfer. It then starts increasing towards a $1/4$ power law, consistent with natural convection around a sphere. This indicates that density driven convection is developing around the bubble due to the lower density of the fluid in

the concentration boundary layer, accelerating the mass transfer rate of CO_2 into the bubble.

3.4 Conclusions

Why is this phenomenon not observed under a moderate supersaturation ratio? In a carbonated beverage $c_0/c_s = 3-4$, while in our experiments the values were 1.08 and 1.18. At moderate supersaturation, bubbles take well under one minute to reach a 0.5 mm detachment radius and advection by the moving interface is significant [35, 38, 39]. On the other hand, at our low supersaturations they take 5 to 15 minutes and advection is negligible. It is plausible that in the first case there is just not enough time for convection to fully develop into a steady state. However it is also conceivable that advection pre-empts density-driven convection by 'squeezing' the boundary layer and keeping it thin. Finally, it is possible too that convection is present in the background, although masked by advection. If so, it might be possible to bring the effect into evidence by consideration of $d\bar{R}/dx$, rather than $\bar{R}(x)$, as we have done in figure 3.2b.

4

The onset of natural convection around growing bubbles *

In the previous chapter, we conjectured that the observed increased in the growth rate of a bubble in a slightly supersaturated water-CO_2 solution was caused by the onset of density driven convection due to the developing concentration gradient around it. As evidence of this, we showed that the dimensionless mass transfer coefficient –the Sherwood number– of the bubbles follows a power law with exponent $1/4$ when plotted against the mass transfer Rayleigh number (Ra_m). While this is consistent with the relations for natural convection around a sphere, by itself it does not provide a criterion to predict when such convective motion should become patent. Therefore, in this chapter we investigate the development of density driven convection around a growing bubble. We look at the convection onset for CO_2 bubbles under a supersaturation $\zeta < 0.5$ and show that we can reasonably predict the onset time with a simple argument considering the buoyancy and drag forces on the depleted liquid around the bubble. Then we take a look at whether convection also develops for bubbles of a much less soluble gas, such as N_2. We are led to conclude that the phenomenon should, in principle, happen for any gas-liquid combination as long as the density of the mix increases with the concentration of gas.

*To be submitted as: [O.R. Enríquez, Andrea Prosperetti, Detlef Lohse and Devaraj van der Meer, The onset of natural convection around growing bubbles].

4.1 Introduction

How do bubbles grow in a slightly supersaturated gas-liquid solution? The answer, of course, depends on what we understand by slight supersaturation. Leaving a formal definition for later, we can consider typical bubbly drinks (soda, beer, or champagne) as containing a moderate excess of gas. Our inquiry instead focusses on solutions that are about ten times less supersaturated. In these, bubble growth should be driven only by gas diffusion and can in principle be treated as a quasi-static process.

In the previous chapter we reported on an experimental study of a carbon dioxide bubble growing on top of a silicon substrate (figure 4.1). We observed significant differences in the growth of such a bubble with respect to the expectations from previous theoretical [72,75] and experimental [35,38,39,78] works and disentangled their causes. The main differences were: *i*) an initially slower (diffusion-driven) growth rate, and *ii*) a later increase which both exceeded the predicted diffusive growth rate and showed a time dependence different from the expected $t^{1/2}$. The first was attributed to the presence of the substrate, in contrast with the theory, which was formulated for an unbounded bubble in an infinite medium, and the second to the onset of natural convection caused by the reduced density of the CO_2-depleted liquid around the bubble. The mentioned previous experimental works targeted bubble growth at supersaturations comparable to carbonated drinks or higher and found that the radius indeed grew proportionally to $t^{1/2}$, even in cases when the advection caused by the expanding bubble surface was no longer negligible. The possibility of density-driven convection was either not considered [38, 39, 78] or explicitly neglected [35].

In this chapter we further delve into the onset of natural convection around a growing bubble, asking the following questions: *a)* what is the time for convection onset and how does it vary with supersaturation? *b)* what is range of supersaturation values for which we can expect natural convection to develop? and *c)* can we expect this to happen for other gases (*e.g.* nitrogen) as well? We present a simple argument to predict the time at which convection influences the bubble growth rate and find very good agreement with experimental measurements using CO_2 bubbles. For experiments with N_2 we observe a change in the growth rate at the predicted time, albeit with a different character than for CO_2.

4.2 Diffusive bubble growth

4.2.1 Experimental conditions

Experiments start with an equilibrated solution of either CO_2 or N_2 in water at a pressure, P_0, of either 0.65 or 0.35MPa. The initial gas concentration, c_0, is given by Henry's law: $c_0 = k_H P_0$. We drop the pressure, gently and isothermally ($T = 21^\circ$C)

to P_s in order to induce a supersaturation defined as

$$\zeta = \frac{\Delta c}{c_s},$$

where $\Delta c = c_0 - c_s$, and c_s is the gas concentration that would be at equilibrium at P_s. A single bubble grows from a hydrophobized micro-pit, of radius $R_p = 10$ or 50 μm, etched on a silicon chip and we track the time evolution of its radius, $R(t)$, by imaging it through a long-distance microscope objective. The size of the pit determines the minimum supersaturation for which a bubble will grow as well as its detachment size but does not directly affect the growth rate. The chips are rectangular in shape, with length 3 cm and width 8 mm. The pit is located at half the width and 5 mm away from the edge opposite to where the chip is held. This ensures that the bubble is far from the holding device, where several bubbles usually grow, and also far enough from the edges, where bubbles might grow on the micro-roughness caused by the cutting process. Experiments with interacting CO_2 bubbles, which will be treated in the next chapter, suggest that bubbles which are more than 1.5 mm apart no longer feel the presence of each other, hence we can be sure of the isolation of our bubble. All experiments were done in the range $0.1 \lesssim \zeta \lesssim 0.5$; at higher supersaturation too many bubbles grow on the walls of the tank and on the edges of the silicon chip and so the quiescence of the liquid can no longer be ensured. Figure 4.1a shows a diagram of the experimental system and a detailed description of it can be found in [28].

4.2.2 Theoretical considerations

Figure 4.1b shows a sketch of a growing bubble. The interior excess pressure due to surface tension is always very small compared to P_s and can be safely neglected. Hence, the gas concentration at the interface can be considered constant and equal to c_s and therefore, the bubble grows due to the diffusive gas flow driven by the concentration difference Δc and the gas diffusivity D. The idealized initial condition is that the bubble grows from a radius R_0 with concentration c_s at the interface and c_0 everywhere else. In practice, R_0 cannot be determined, only estimated to be at most the same volume as the nucleation site; furthermore, since the pressure change from P_0 to P_s takes place gradually ($\sim$ 30s) the concentration difference is not established instantaneously. However, the effects from this are limited to an initial transient and have been treated in the previous chapter.

The asymptotic solution for the growth of an unbounded bubble in an infinite medium with the aforementioned initial conditions, expressed in dimensionless variables, as obtained by [72] is

$$\bar{R} \approx \left[\gamma + \left(1+\gamma^2\right)^{1/2}\right] x \equiv Sx, \tag{4.1}$$

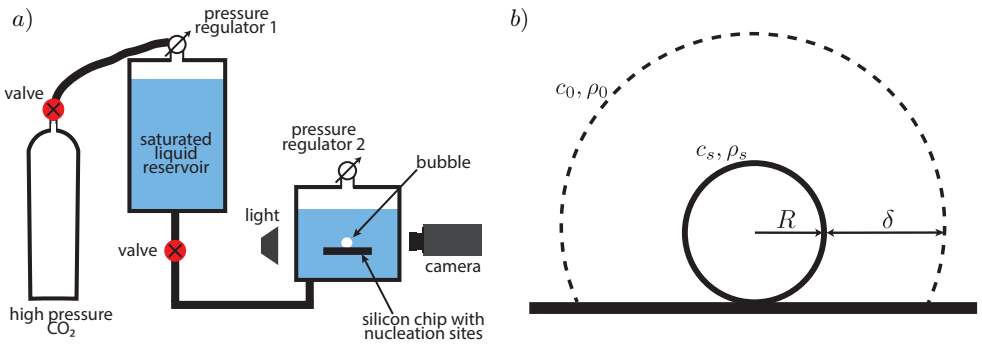

Figure 4.1: Sketches of the experimental system and the growing bubble. a) A saturated water-CO_2 solution is prepared in the reservoir tank ($V \approx 7$l) at a maximum pressure of 1 MPa. After transferring part of the mix to the observation tank ($V \approx 1$l), we drop the pressure slightly in order to produce a small supersaturation. The bubble grows from a nucleation site provided by a single hydrophobic cavity etched in a silicon chip. We image it with a long distance microscope objective and a PCO camera though a window in the tank. b) As the bubble grows, it develops a concentration and density profile around it, extending a distance δ into the solution.

which is valid for $\bar{R},\ x \gg 1$. Where

$$\begin{aligned} \bar{R} &= \frac{R(t)}{R_p}, \\ x &= \sqrt{\frac{2D\beta}{R_p^2}t}, \\ \beta &= \frac{\Delta c}{\rho}, \text{ and} \\ \gamma &= \sqrt{\frac{\beta}{2\pi}} \end{aligned} \tag{4.2}$$

with ρ representing the density of the gas at pressure P_s.

In the previous chapter, we found that the influence of the silicon chip, which acts like an obstacle for mass transfer through part of the bubble area, can be approximated with a correction to the asymptotic solution yielding

$$\bar{R} \approx \left[\gamma + \left(\frac{1}{2} + \gamma^2\right)^{1/2}\right] x \equiv S^* x. \tag{4.3}$$

In our experiments, $\beta \sim 0.1$, so we find that $S \approx 1$ and $S^* \approx \sqrt{2}/2$.

	CO_2	N_2
Diffusivity (D)	1.97×10^{-9} m^2/s	1.88×10^{-9} m^2/s
Henry's constant (k_H)	1.50×10^{-5} kg/m^{3}Pa	1.68×10^{-7} kg/m^{3}Pa
Expansion coeff. (λ_c)	5.91×10^{-4} m^3/kg	3.57×10^{-4} m^3/kg
Density (ρ)	9.89 kg/m^3	6.29 kg/m^3

Table 4.1: Properties of CO_2 and N_2 when dissolved in water at $P = 0.55$ MPa and $T = 21°$C. The large difference in the values of Henry's constant accounts for the two orders of magnitude change in solubility.

4.2.3 Concentration and density profile

As the bubble grows it depletes its surroundings of gas, developing a concentration profile that extends a distance $\delta = \sqrt{\pi D t}$ into the solution (fig. 4.1b) and soon becomes larger than the bubble radius. Variations in concentration imply changes in density, determined by the concentration expansion coefficient $\lambda_c = \frac{1}{\rho}(\frac{\partial \rho}{\partial c})$, which for a dilute solution of gas in a liquid can be approximated as:

$$\lambda_c \approx \frac{1}{\rho_{H_2O}} \left(1 - \frac{M_{H_2O}}{M\text{gas}}\right) \tag{4.4}$$

where M stands for molecular weight. Defined this way, a positive λ_c means that density increases with concentration.

If the density of the saturated solution is ρ_0, the value at the bubble surface is given by $\rho_s = \rho_0(1 - \lambda_c \Delta c)$. Table 1 shows the properties of aqueous solutions of CO_2 and N_2. The fact that $\lambda_c \ll 1$, combined with a $\Delta c \approx 1$ kg/m^3 (for our CO_2 experiments, and much smaller for the N_2 case) makes it tempting to neglect the changes in density, which has routinely been done in most earlier works on bubble growth in a supersaturated solution. However, as we will see later, the long growth times of our bubbles require that we take their effects into consideration.

4.3 Results for CO_2 bubbles

4.3.1 Observations of bubble growth

The typical bubble growth from our experiments is best appreciated by plotting the derivative $d\bar{R}/dx$, which represents the dimensionless rate of change of the bubble area (see appendix). Following equation 4.3 this should be constant and approximately equal to S^*. Figure 4.2a shows $d\bar{R}/dx$ divided by S^* for some experiments with CO_2 solutions at $P_0 = 0.35$MPa. After the initial transient, there is a plateau around the value of 1 which indicates diffusion-driven growth. Afterwards, the curves

start rising as a result of the enhancement of mass-transfer by natural convection. That this is indeed due to natural convection is seen when we recast the data into a Sherwood number (Sh) and a mass transfer Rayleigh number (Ra_b), respectively defined as:

$$\mathrm{Sh} = \frac{hL}{D} = \frac{2R\dot{R}}{D\beta}$$
$$\mathrm{Ra}_b = \frac{\Delta c \lambda_c g (2R)^3}{\nu D}$$

where $h = \rho\dot{R}/\Delta c$ is the mass transfer coefficient (see appendix), and we use the the bubble diameter as a length scale (L). $\dot{R}$ is the (dimensional) time derivative of the radius, which is computed by numerical differentiation of the acquired time series of R. When plotted this way (fig. 4.3), the rising part of the curve is described by a power law with exponent $1/4$, which is the expected relation between Sh and Ra_b for natural convection around a sphere. Further direct evidence of the presence of natural convection is obtained by comparing with experiments where the bubble grows underneath the chip and between two parallel plates with a separation of 1 mm (fig. 4.2b). In the first case, an increase of the growth rate is still observed, but at a slower pace, which is to be expected because of the geometrical inversion of the problem where the presence of the chip makes it harder for the buoyant liquid to rise. In the second case, the growth rate starts to rise but decreases again as the bubble comes close to the other wall, which inhibits the possibility for convection to develop.

4.3.2 Convection onset

The question that arises naturally is what is the critical Rayleigh number for convection onset, or equivalently, since Ra_b is a time dependent parameter, at what time does it take place. In order to investigate this, for all the experiments we carried out we determine the onset Ra_b by fitting a horizontal line to the plateau and a power law to the rising part of the Sh versus Ra_b curves. The transition is considered to be the at the intersection of those lines, and the result of those measurements is shown in figure 4.4. In all cases the best fitting power-law had a slope within 0.25 ± 0.2 consistent with figure 4.3. The fitting of the plateau was sometimes more difficult due to its short duration and proximity to the initial transient. Therefore, the nature of the procedure to determine the onset Ra_b accounts for the spread in the data. From the Ra_b measurements in figure 4.4, we can extract both the radius and the time of convection onset, and compare the latter with our estimate for the onset time, t_{ons}, discussed in the next subsection (figure 4.5).

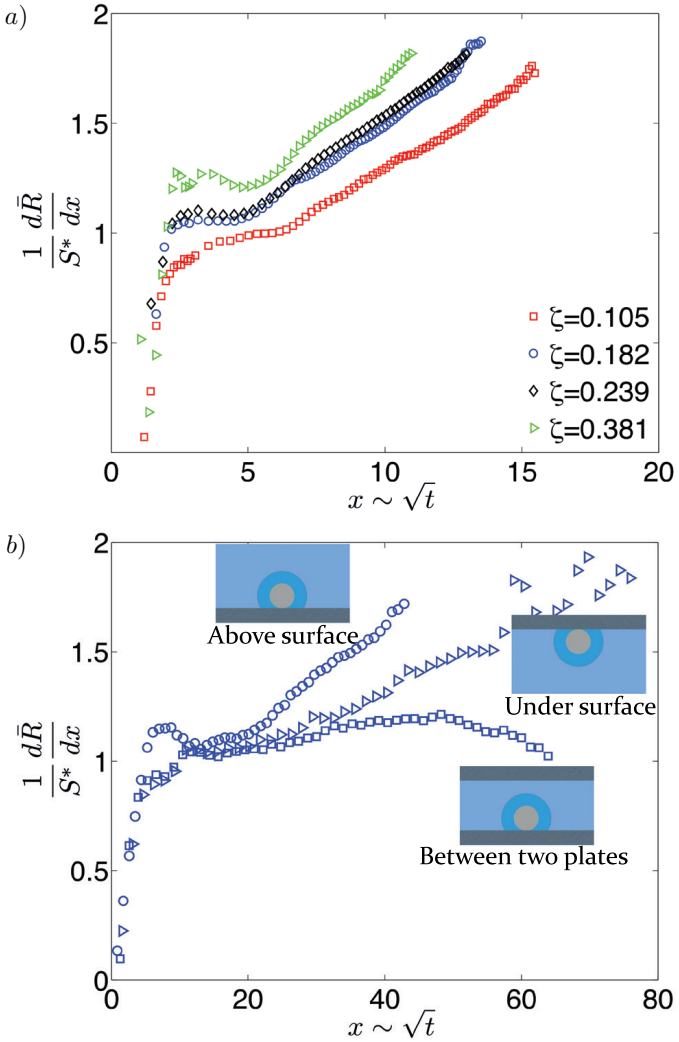

Figure 4.2: Dimensionless rate of change of the bubble area, divided by its theoretical (constant) value for a purely diffusive growth regime as a function of $x \sim \sqrt{t}$ (eq.4.3). This value is calculated with the correction proposed in [79] to account for the influence of the silicon chip. The leftmost rising part and horizontal plateau of the curves are expected from diffusion-driven growth; the right-hand rising part suggests the influence of convection. a) Experiments with $P_0 = 0.34$MPa and a pit with $r_p = 50\mu$m and various supersaturations ζ. Here the bubble grew on top of the silicon chip. b) Experiments with $P_0 = 0.65$MPa, a pit with $r_p = 10\mu$m and $\zeta \approx 0.182$ with the bubble in different positions.

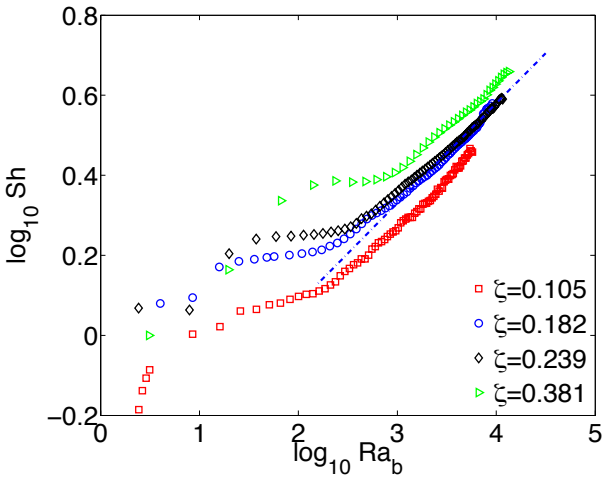

Figure 4.3: Sherwood number, Sh, as a function of the mass transfer Rayleigh number Ra_b calculated using the bubble diameter as a length scale with the same data as figure 4.2a. The line represents a $1/4$ power-law, which indicates that in the advanced stages, growth is driven by natural convection.

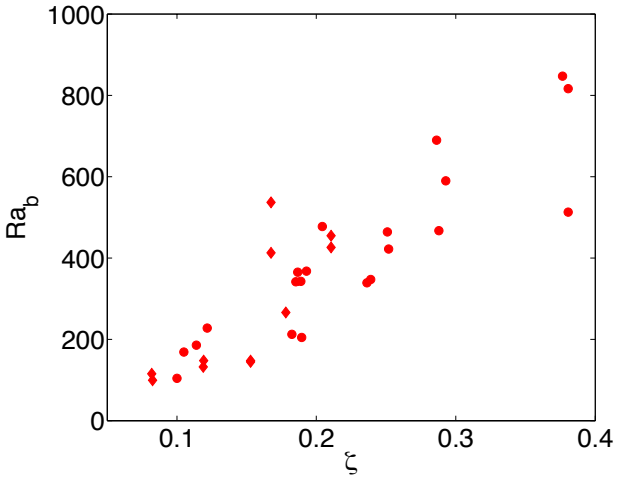

Figure 4.4: Rayleigh number, Ra_b, based on the bubble diameter, at the moment of convection onset as a function of supersaturation, ζ. Diamonds correspond to experiments with $P_0 = 0.65$MPa and $r_p = 10\mu$m and circles to $P_0 = 0.34$MPa and $r_p = 50\mu$m.

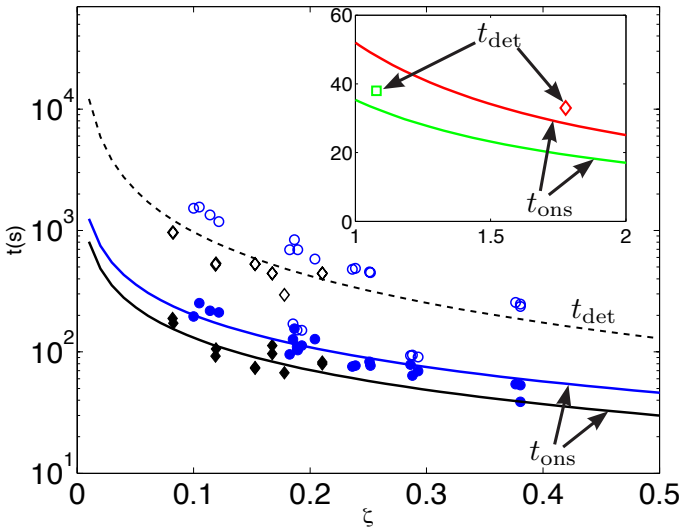

Figure 4.5: Experimental and theoretical convection onset times, t_{ons} (solid symbols and solid lines, respectively) as function of the supersaturation coefficient ζ. Diamonds (black) correspond to experiments with $P_0 = 0.65$MPa and $r_p = 10\mu$m and circles (blue) to $P_0 = 0.34$MPa and $r_p = 50\mu$m. Open symbols show the bubble detachment times and the dashed black line represents the theoretical detachment time, t_{det}, of a bubble growing (on a surface) only by diffusion until a radius of 500 µm. Inset: the green square and red diamond show the detaching times of bubbles in the experiments by [35] and [38], respectively, which were done at higher supersaturations. They reported no influence of natural convection. The convection onset time t_{ons} predicted by our model for their experiments is shown in the corresponding green and red lines. It is only very slightly below the detachment time, which provides a possible explanation to why they did not observe natural convection.

Onset time estimate

As mentioned earlier, when the bubble grows it creates around itself a region with reduced gas concentration and smaller density than the fluid bulk. This configuration –a light fluid underlying a heavier one– is unstable under gravity and hence the lighter fluid will experience an upward buoyant force. In order to calculate this force, we must calculate the volume, V_b, of what we will hereafter term the buoyant region which is the spherical segment (of diameter $d = 2R + 2\delta$ and height $2R + \delta$) denoted by the dotted line in figure 4.1b minus the volume of the bubble. With the bubble radius and buoyant region growing, respectively, as $R \approx a\sqrt{t}$ and $\delta \approx \sqrt{\pi D t}$, the buoyant volume is given by

$$V_b \approx \frac{\pi}{3}\left[(2R+\delta)^2(R+2\delta) - 4R^3\right] \tag{4.5}$$

$$= \frac{\pi}{3}\left[\left(12a^2 + 9a + 2\pi D\right)(\pi D)^{1/2}\right] t^{3/2} \equiv f_V t^{3/2}, \tag{4.6}$$

where $a = S^* \sqrt{2D\beta}$. We stress that f_V is a dimensional constant that depends on the liquid and gas properties, and most importantly on the supersaturation.

We can then estimate the terminal rise velocity of the buoyant region by recognizing that the only forces acting upon it are buoyancy, F_b, and viscous (Stokes) drag, F_d (the small density difference and quasi-static growth of V_b in the small supersaturation regime make the acceleration and therefore the added mass force on V_f negligible). Therefore we have:

$$F_b \approx \Delta c \lambda_c \rho_0 g V_b \tag{4.7}$$

$$F_d \approx 6\pi u d \mu \tag{4.8}$$

which combined lead to

$$u \approx \frac{\Delta c \lambda_c g V_b}{6\pi \nu d} \tag{4.9}$$

Note that for the force balance we must consider that the velocity difference between the rising fluid and the descending fluid that comes to replace it is $2u$.

In order for the liquid at the bubble interface to remain "fresh" – *i.e.* not depleted of CO_2– the ascending fluid should go away fast enough. The parameter that should indicate this is the Reynolds number, Re$= ud/\nu$. When $\mathrm{Re}_d \sim 1$, the rise velocity caused by buoyancy is of the same size as ν/d, the velocity scale with which viscosity is able to "fil" the space with depleted liquid from the vicinity. Using the above expression for u:

$$\mathrm{Re}_d = \frac{ud}{\nu} \approx \frac{\Delta c \lambda_c g f_V}{6\pi \nu^2} t^{3/2} \tag{4.10}$$

from which we can straightforwardly obtain t_{ons}, the time at which $\text{Re}_d = 1$ as function of the experimental parameters

$$t_{\text{ons}} \approx \left(\frac{6\pi\nu^2}{\Delta c \lambda_c g f_V} \right)^{2/3} \tag{4.11}$$

In figure 4.5, we see that without any free parameter the onset time prediction agrees very well with experimental measurements (in which the error is about 10%). We also show, for reference, the experimental detachment times (t_{det}) and the theoretical ones if the bubbles would grow only by diffusion to a radius of $500\mu m$ (which is approximately the detachment size from the $R_p = 10$ μm pit). Furthermore, we include as well the detachment times of experiments by other authors [35, 38] who reported no influence of natural convection in bubble growth but where, however, the advection caused by the expanding bubble surface might not be negligible. Such times are only slightly larger than our prediction for t_{ons}, which could explain why convection was not observed. However, possibly there was indeed no natural convection since at those values of ζ the quasi-static growth consideration on which our analysis is based no longer holds, and if indeed present, it might be overpowered by advection from the moving surface. We have found that when $\zeta \approx 0.4$, at the moment of convection onset $2R \approx \sqrt{\pi D t}$, which indicates the end of the validity of quasi-static growth is near, since it requires that $R \ll \sqrt{\pi D t}$.

Finally, using $f_V t^{3/2} = V_b$ in eq. 4.10 we realize that Re_d is in fact a Grashof number, divided by a factor 6π, with $V_b^{1/3}$ as length scale. Multiplying it by the Schmidt number ($\text{Sc} = \nu/D$) we obtain a Rayleigh number based on the the buoyant volume:

$$\text{Ra}_{V_b} = \frac{\Delta c \lambda_c g V_b}{6\pi\nu D} \tag{4.12}$$

Figure 4.6 shows the values of Ra_{V_b} at the start of convection for all our experiments. In spite of their spread, the data show no dependence on ζ, unlike the Rayleigh number based on the bubble diameter, Ra_b, which clearly increases with supersaturation (*cf.* 4.4).

4.4 The case of N_2 bubbles

Now the picture is clear for CO_2, which admittedly is a gas with an exceptionally high solubility in water (indicated by Henry's constant, k_H). What happens if we turn to a gas with a lower solubility like N_2? The advantage of this lies in the chemical inertness of the latter in water, whereas CO_2 dissociates slightly. The diffusivity, D, and expansion coefficient, λ_c, in aqueous solutions are similar for both gases, however, k_H is about one hundred times smaller for N_2 (see table 1), which leads to a an equally smaller Δc if the supersaturation ζ is the same as in the CO_2 experiments.

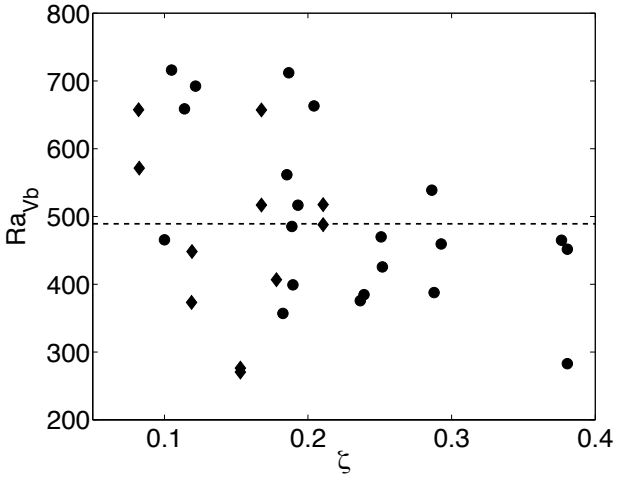

Figure 4.6: Rayleigh number Ra_{V_b}, based on the buoyant volume V_b, at the moment of convection onset as a function of supersaturation ζ. Diamonds correspond to experiments with $P_0 = 0.65$MPa and $r_p = 10\mu$m and circles to $P_0 = 0.34$MPa and $r_p = 50\mu$m.

The implications are clear when we remember that $R \sim \sqrt{\Delta c D t/\rho}$: N_2 bubbles will grow much more slowly and Re_d will take much longer to reach a value of 1. Figure 4.7 shows the theoretical detachment (t_{det}) and onset (t_{ons}) times for the two gases. Long as they are, it is feasible to do experiments for the times it takes N_2 bubbles to grow and to investigate if they develop convection. Some experimental $d\bar{R}/dx$ curves are shown in figure 4.8, along with an example for CO_2. Note that although the time is very different in experiments with each gas, x is similar for N_2 and CO_2. The early stages look very similar; in fact, the slowness of N_2 bubbles allows for a smoother plateau region, avoiding the hump in the CO_2 curve which is due to the oscillations of the pressure controller after the pressure drop. At the predicted t_{ons} there is a clear change in behaviour for the N_2 bubbles, but very different than in the CO_2 case. To understand the possible cause of this, it helps to interpret figure 4.8 using dimensional terms: t_{ons}, $R(t_{\mathrm{ons}})$ and $\delta(t_{\mathrm{ons}})$ are, respectively, 60 s, 300 μm and 610 μm for the CO_2 bubble; for the N_2 ones, 3280 s, 210 μm and 4.4 mm when $\zeta = 0.304$ and 2620 s, 230 μm and 4.0 mm when $\zeta = 0.457$. *I.e.*, whereas the onset radius, $R(t_{\mathrm{ons}})$ is of the same order, the onset time, t_{ons} and consequently the boundary layer thickness are much larger for N_2.

As we mentioned in section 4.2.1, during experiments it is not uncommon that some bubbles grow on the edges of the silicon chip, which are at least 4 mm away. For

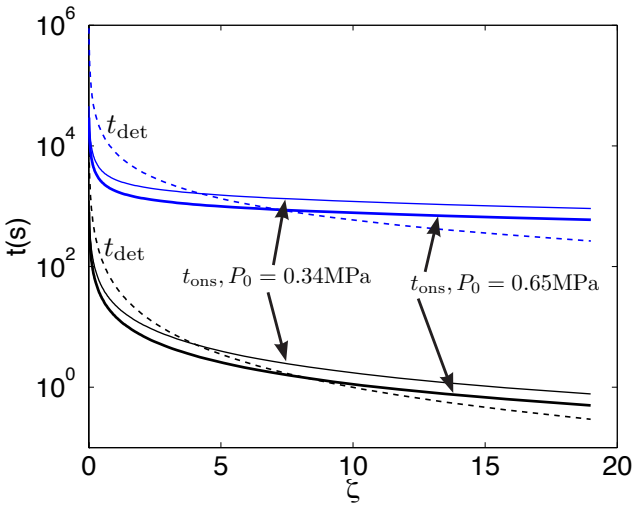

Figure 4.7: Theoretical detachment ($t_{\rm det}$, dashed) and convection onset ($t_{\rm ons}$, solid) times as function of the supersaturation coefficient ζ for CO_2 (black) and N_2 (blue) bubbles. For thick solid lines $P_0 = 0.65$ MPa, and for thin solid ones $P_0 = 0.34$ MPa. The detachment curves are calculated considering a final radius of $R_{\rm det} = 500$ μm, corresponding to a pit radius of $r_p \approx 10$ μm.

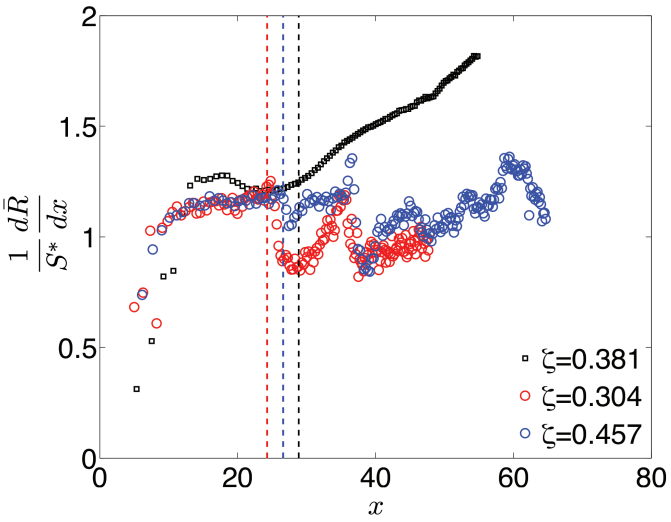

Figure 4.8: Normalized dimensionless rate of change of the surface area for one CO_2 bubble (black squares) and two N_2 ones (red and blue circles). The vertical dashed lines in corresponding colours indicate the predicted convection onset times $x_{\text{ons}} \sim \sqrt{t_{\text{ons}}}$ for each case (*cf.* fig.4.7).

CO_2 bubbles this is not a problem since that distance is much larger than $\delta(t_{\text{ons}})$ and hence beyond the range in which they might interact. However, for N_2 this distance allows for considerable overlap of buoyant regions, which might cause that the onset of mixing brings to the bubble surface liquid that is already depleted of gas. This is consistent with the irregular growth rates that we observe in all our N_2 experiments after t_{ons} and with the lack of reproducibility beyond that point even though the initial growth is reproducible and similar to CO_2 bubbles. In addition, the mixing process itself might be significantly altered in the case of N_2 bubbles where, although the amount of buoyant force is similar, the volume is much larger than for CO_2 bubbles (where it is of the order of the bubble volume).

4.5 Conclusions

We have shown that quasi-static diffusive bubble growth, driven by a small supersaturation of gas in a liquid solution can lead to natural convection that enhances the bubble growth rate (figures 4.2 and 4.3). For experiments with CO_2, the prediction for the onset time agrees very well with measurements, despite the difficulty of determining t_{ons} precisely (figure 4.5). The prediction for t_{ons} suggests that, in principle, density driven convection around a growing bubble can occur at any value of super-

saturation as long as the detachment radius is large enough (figure 4.7). However, this might not be the case when the interface moves fast enough to cause advection. The verification of this is presently beyond our experimental capability.

For N_2 bubbles, there is a clear transition taking place at t_{ons}, consistent with the onset of mixing, but different than in the CO_2 case due to the long range interactions that are made possible by the very long growing times in this case (figure 4.8). That we observe such transition with a gas one hundred times less soluble, suggests that this can happen for any gas-liquid solution as long as the density of the mix increases with gas concentration.

Appendix A: Physical interpretation of $d\bar{R}/dx$

In order to understand what $d\bar{R}/dx$ physically represents, it is useful to express this term using its dimensional components (see equations 4.2)

$$\frac{d\bar{R}}{dx} = \frac{1}{R_p\sqrt{D\frac{\Delta c}{R_p^2\rho}}}\frac{dR}{d\sqrt{t}} \tag{4.13}$$

we then substitute $d\sqrt{t} = \frac{1}{2}t^{-1/2}dt = dt/2\sqrt{t}$ to get

$$\frac{d\bar{R}}{dx} = \frac{2\sqrt{t}}{\sqrt{D\frac{\Delta c}{\rho}}}\frac{dR}{dt} \tag{4.14}$$

and finally make use of $R \approx S^*\sqrt{D\frac{\Delta c}{\rho}t}$ to eliminate the dependence on $\sqrt{t}$

$$\frac{d\bar{R}}{dx} = \frac{2R}{S^*D\frac{\Delta c}{\rho}}\frac{dR}{dt} = \frac{1}{S^*D\frac{\Delta c}{\rho}}\frac{d(R^2)}{dt} \tag{4.15}$$

which makes clear that $d\bar{R}/dx$ is the dimensionless rate of change of the bubble area.

Appendix B: calculation of the Sherwood number

The Sherwood number $\text{Sh} = hL/D$ represents the dimensionless mass transfer coefficient with length scale L and diffusivity D. For the case of a gas bubble growing due to a concentration difference Δc (kg/m^3), Sh is constructed as follows:

Starting from the definition of the mass transfer coefficient, h

$$h = \frac{\dot{m}}{A\Delta c} \tag{4.16}$$

where $\dot{m}$ is the mass transfer rate in $\mathrm{kg/s}$ and A is the bubble surface area in m^2 respectively given by

$$\dot{m} = \rho \frac{dV}{dt} = \rho 4\pi R^2 \frac{dR}{dt} \tag{4.17}$$

$$A = 4\pi R^2 \tag{4.18}$$

and combined with 4.16 to give

$$h = \frac{\rho \dot{R}}{\Delta c} \tag{4.19}$$

Finally, the bubble diameter, $2R$, is used as the relevant length scale L, and hence

$$\mathrm{Sh} = \frac{\rho 2R\dot{R}}{D\Delta c} = \frac{2R\dot{R}}{D\beta} \tag{4.20}$$

5

Interactions between gas bubbles growing in a supersaturated solution *

How do gas bubbles interact with each other when growing in a slightly supersaturated solution? We explore and discuss two types of interaction: a 'spatial' one, when two or more bubbles grow near each other simultaneously and a 'temporal' one when a bubble grows from a nucleation site from which one or more bubbles have grown and detached before. In the first case, bubbles directly affect each other's growth rate depending on the distance between them and the number of neighbours. In the second case, the interaction takes place through the gas depletion of the surrounding liquid by a growing bubble, which, upon detaching, leaves modified initial conditions for its successor. Comparing to the single bubble case, we start from pairs and triplets in linear and triangular arrangements and finally turn to a line of many growing bubbles. For a sequence of bubbles we observe the mixed effects of the two kinds of interaction, leading to subtle phenomena which are enriched by the fact that under low supersaturations bubble growth is initially driven by diffusion but eventually develops a density-driven convective flow around it which enhances the growth rate.

*To be submitted as: [O.R. Enríquez, Andrea Prosperetti, Detlef Lohse and Devaraj van der Meer, Interactions between gas bubbles growing in a supersaturated solution].

5.1 Introduction

So far, we have treated a bubble growing in isolation. However, that is rarely the case in natural (or industrial) occurrences of bubble formation in supersaturated solutions. In general, when bubbles grow in such a solution, multiple nucleation sites are present and their position cannot easily be controlled. Bubbles growing close to each other are expected to interact since their growth relies on incorporating gas molecules from the solution. Therefore, the presence of a nearby bubble implies a competition for a limited available species. Furthermore, in a bubbling process where the nucleation-growth-detachment cycle is short, bubbles will also interact by mixing the solution as they detach and rise [40, 80].

Perhaps the ultimate example of bubbles neighbouring each other is foam, where a mixture of liquid and gas develops bubbles which are separated only by very thin liquid films, usually stabilized by the influence of a surfactant. Foams have been studied in connection to production of polymeric foams [22–25], the degassing of magmas that can lead to volcanic eruptions [9, 10] and stout beers [42]. Another case receiving considerable attention is the formation of 'foamy oil' which is a phenomenon that happens when dissolved gasses start coming out of the solution during oil production [43–47], and which has the extra complication of occurring inside porous materials [81–83].

Bubbles growing close to each other in smaller numbers have been studied by Karapantsios, *et al.* [84] in connection to bubble formation on heaters. In such a case, bubbles grow due to the supersaturation induced by the local heating of the liquid (below the boiling point) and are usually detrimental for heat transfer purposes [85]. These studies were carried out at low gravity conditions in order to suppress the influence of buoyancy, and the authors observed that two bubbles growing next to each other do indeed slow down each other's growth rate. Earlier experiments with electrolysis [32] and high levels of supersaturation [86], had already observed that neighbouring bubbles do not follow the $R \sim t^{1/2}$ growth predicted for single bubbles.

As mentioned, authors studying interacting, growing bubbles have based their comparisons on several experimental works that have confirmed that a single bubble follows the $R \sim t^{1/2}$ growth obtained in the theoretical solutions of *e.g.* Epstein and Plesset [72] and Scriven [75]. However, in the previous chapters we have seen that, in the low supersaturation limit, the development of a concentration profile around the bubbles gives rise to density-driven natural convection that enhances the mass transfer rate. We will see that this continues to play an important role when bubbles grow close to each other.

Besides the numerous situations where bubbles can grow close to each other, 'competitive' diffusive processes have been studied in connection with nanoelectrode arrays, where the overlap of the diffusion layers of the individual elements influences the behaviour of the array [87, 88]. Another analogous situation can be found in the

non-equilibrium growth of crystals by deposition which can lead to the formation of complex patterns [89].

5.2 Experiments

All experiments in this chapter started from a saturated water-CO_2 solution at $P_0 = 0.65$ MPa with the initial gas concentration given by Henry's law: $c_0 = k_H P_0$. We drop the pressure smoothly (in thirty seconds) and isothermally ($T = 21°$C) to $P_s = 0.55$ MPa . The resulting supersaturation ζ of the solution is defined as

$$\zeta \equiv \frac{\Delta c}{c_s} \approx 0.18,$$

where $\Delta c = c_0 - c_s$, and c_s is the gas concentration that would be at equilibrium at P_s, *i.e.*, $c_s = k_H P_s$. The extra pressure induced by the bubble curvature is negligible for the experimental conditions used here. As nucleation sites, we use hydrophobic pits etched on a rectangular silicon substrate with length 3 cm and width 8 mm. The substrate is held in the center of the observation tank by a device introduced and fixed through a porthole at half the tank depth. This way, the bubbles grow far away from the walls and bottom, where some bubbles may grow as well, and also far from the region near the free surface where significant degassing takes place. The pits are located at half the width and 5 mm away from the opposite edge to the holding point (see figure 5.1). This ensures that the bubbles are far from the holding device, where some bubbles usually grow, and also far enough from the edges, where bubbles might also grow on the micro-roughness caused by the cutting process.

We use the following configurations of nucleation sites (see fig. 5.1):

- Single pit
- Pairs at distances $l = 570,\ 760,\ 1000$ and 1500 μm
- Triplets in a line at $l = 760$ and 1000 μm
- Triplets in triangular arrangement at $l = 760$ and 1000 μm
- Fourteen in line (only six within view) at $l = 570$ μm

In all cases the pits have a radius $R_p = 10$ μm.

5.3 The growth of a single bubble

The growth of a single bubble in the above experimental conditions has been studied in the previous two chapters. After emerging from its pit, a bubble initially grows

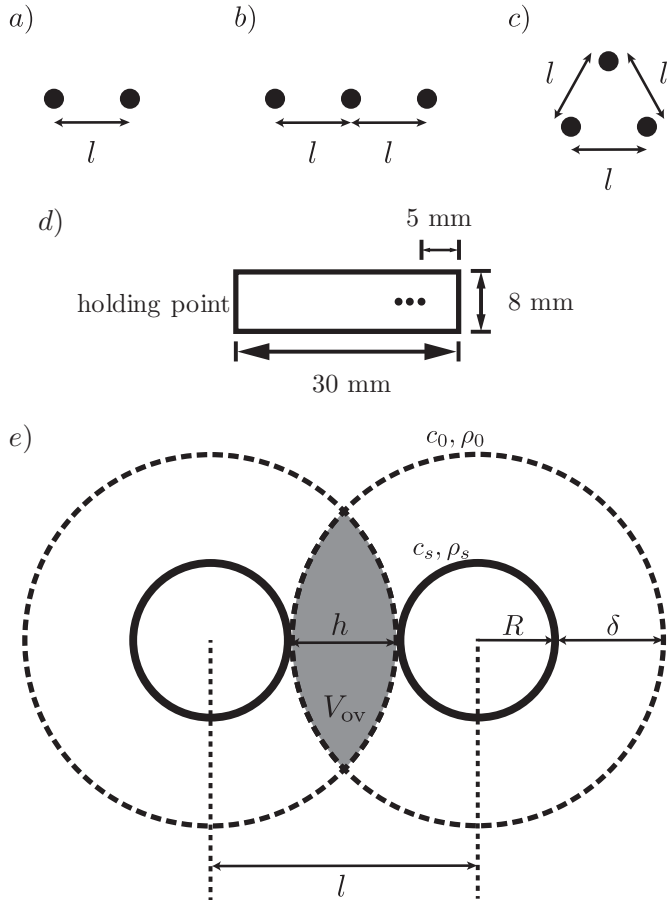

Figure 5.1: Diagram of the pit configurations used in experiments. a) pair, b) triplet in line and c) triangular triplet. All pits have a radius of 10 μm. d) Sketch of the silicon chips, showing their dimensions and the positioning of the pits. e) Sketch of two bubbles growing side by side, separated a distance l. Their concentration profiles overlap with a length h and volume V_{ov} (shaded region).

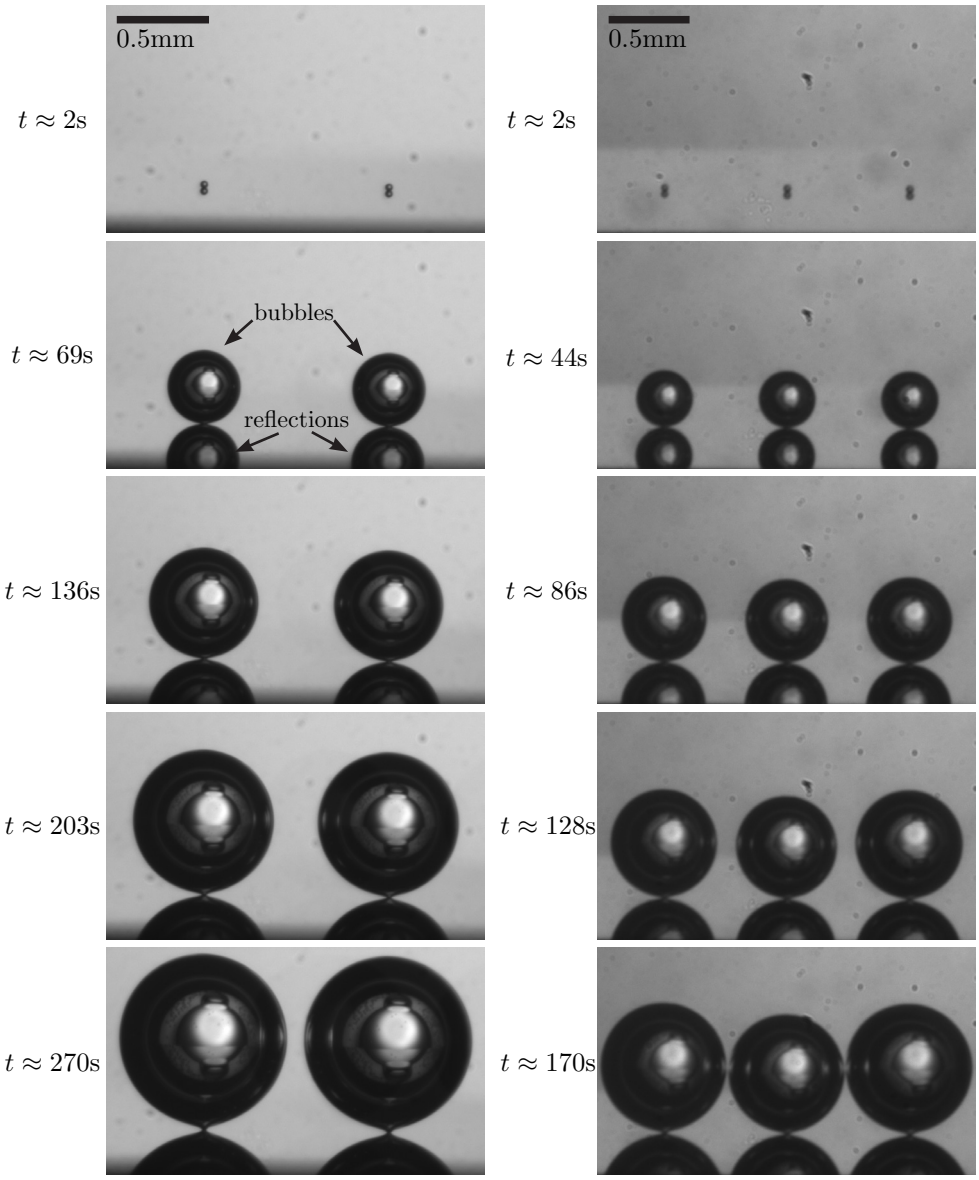

Figure 5.2: Snapshots from experiments with a pair of bubbles at distance $l = 1000$ μm and a line triplet with $l = 760$ μm

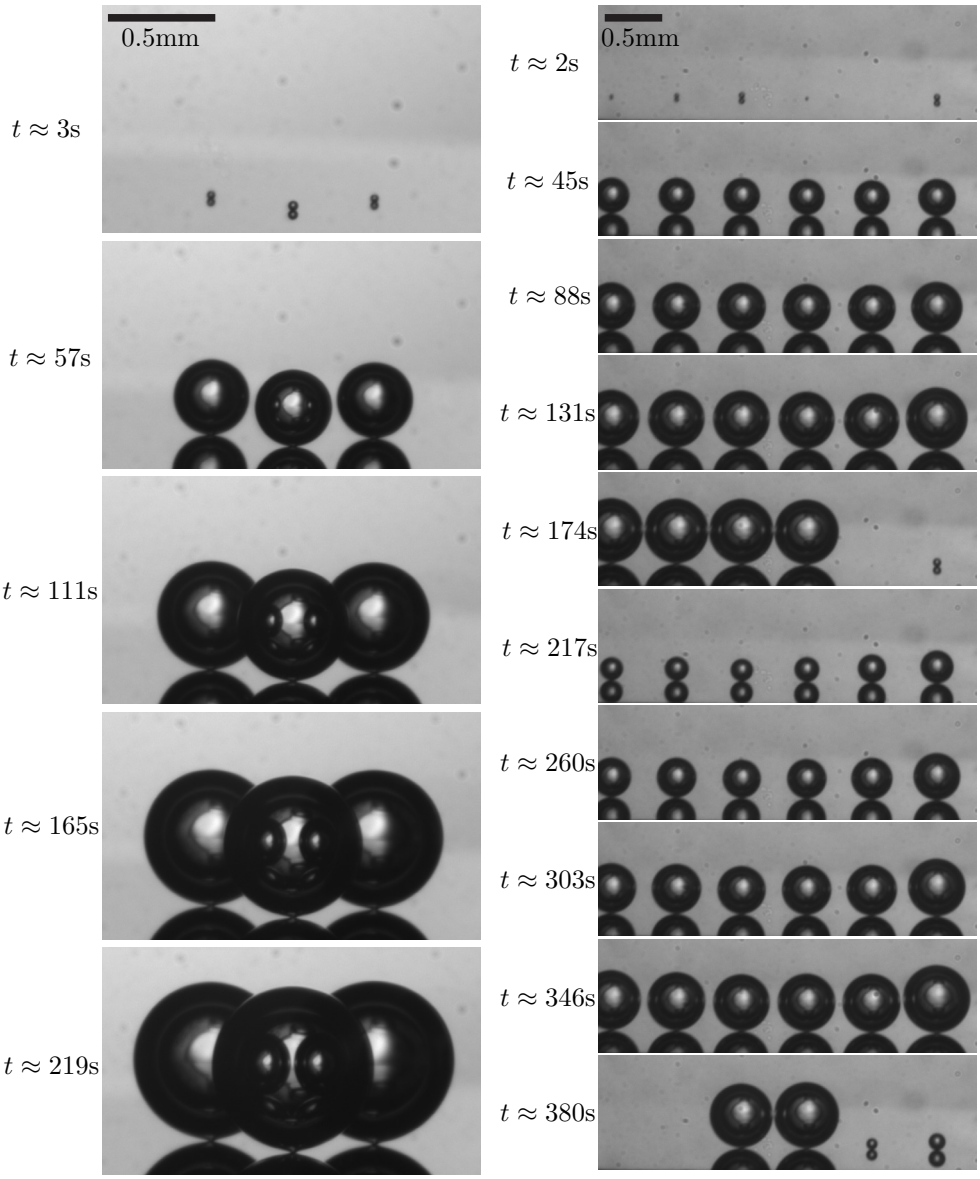

Figure 5.3: Snapshots from experiments with a triangular triple at distance $l =$ 760 µm and a line $l = 570$ µm

driven by gas diffusion but with a lower growth rate than the theoretical prediction for a bubble in an unbounded medium [72]. This has been shown to be largely due to the influence of the substrate on which the bubble grows, which partially obstructs mass transfer. Later on, the growth rate starts to increase, and $R(t)$ is no longer proportional to $t^{1/2}$, as was the case in the diffusive regime. This is due to the onset of density driven convection that originates from the concentration profile that forms around the bubble as it grows. As was shown in the previous chapter, the time at which convection becomes dominant for the bubble growth rate can be predicted from experimental parameters, considering the balance between the buoyancy of the gas depleted region around the bubble and viscosity.

The asymptotic solution for the diffusion-driven growth of an unbounded bubble in an infinite medium, expressed in dimensionless variables, as obtained by [72] is

$$\bar{R} \approx \left[\gamma + \left(1+\gamma^2\right)^{1/2}\right] x \equiv Sx, \tag{5.1}$$

which is valid for $\bar{R},\ x \gg 1$. Where

$$\begin{aligned}
\bar{R} &= \frac{R(t)}{R_p}, \\
x &= \sqrt{\frac{2D\beta}{R_p^2}}t, \\
\beta &= \frac{\Delta c}{\rho}, \text{ and} \\
\gamma &= \sqrt{\frac{\beta}{2\pi}}
\end{aligned}$$

with ρ representing the density of the gas at pressure P_s.

In [79], we found that the influence of the silicon chip, which acts like an obstacle for mass transfer through part of the bubble area, can be approximated with a correction to the asymptotic solution yielding

$$\bar{R} \approx \left[\gamma + \left(\frac{1}{2}+\gamma^2\right)^{1/2}\right] x \equiv S^* x. \tag{5.2}$$

In our experiments, $\beta \sim 0.1$, so we find that $S \approx 1$ and $S^* \approx \sqrt{2}/2$.

The detachment radius of the bubble is determined by the competition between buoyancy, that pulls the bubble upward, and surface tension that keeps it pinned on the pit and is given by

$$R_F = \left(\frac{3}{2}\frac{\sigma R_{pit}}{\rho g}\right)^{1/3}$$

For pits with $R_{pit} = 10\ \mu m$, the detachment radius is $R_F \approx 470\ \mu m$, considering a slightly reduced surface tension of $\sigma = 0.069\ N/m$ and slightly increased liquid density of $\rho = 1010\ kg/m^3$ due to the dissolved CO_2. In experiments we observe small variations around that value which are attributable to small differences in the hydrophobic coating of the pits fabricated in different occasions.

For a single bubble it was also observed that the first bubble that emerges from the pit has a slightly different initial behaviour than the subsequent ones. The cause of this, which was treated in [35], is that the first bubble grows in a medium with homogeneous gas concentration, under conditions that actually resemble the theoretical scenario. Upon detaching, the bubble leaves behind itself a slight local gas depletion that slows down the growth of the following bubble. The size of the depleted region must be a fraction of the volume affected by the concentration profile that develops around the bubble. For quasi-static, diffusive growth, this region theoretically extends a typical distance $\delta = \sqrt{\pi D t}$, the boundary layer thickness, from the bubble surface. A rough estimate can be made considering that the bubble, upon detaching, takes with it half of the depleted volume, leaving the other half behind to fill the place left by the bubble. However, since density driven convection takes place during a significant time of the bubble lifetime, the real extension of the concentration profile cannot be easily calculated. In chapter 3 we estimated the extension (L) of the depleted area by solving numerically the diffusion problem with an initial linear concentration profile over the length L, using this quantity as a fitting parameter to match our experimental observations. For the experimental conditions of the experiments reported here, we found $L \approx 380\ \mu m$ for bubbles detaching at $R_{det} \approx 470\ \mu m$ after growing for about 300 seconds.

5.4 Growth of two neighbouring bubbles

We start our exploration of interacting bubbles looking at pairs at different distances. The interaction between them should be determined by how much each one of the modifies the medium surrounding the other one. For purely-diffusive growth, bubbles are expected to start competing for the surrounding gas at some point, thereby reducing their growth rate [84]. A phenomenon like Ostwald ripening [90], where small bubbles dissolve and large ones grow larger for a more favourable energetic condition, is not expected to happen (and indeed was never observed) since the Laplace pressure jump is negligible for bubbles larger than a few microns in radius, and hence, surface-tension-induced concentration differences are negligible when compared to the pressure-induced Δc.

It is reasonable to expect that the interaction is mediated by the overlapping concentration profiles (figure 5.1). For two bubbles with a distance l between them and

equal radii, R, we define the dimensionless overlap as

$$h^* = \frac{h}{2\delta} = \frac{2(R+\delta)-l}{2\delta} \tag{5.3}$$

Thus, $h^* < 0$ indicates no overlap, $h^* = 0$ is the moment where the concentration profiles "touch" each other, at $h^* = 1/2$ the profile reaches the other bubble (see figure 5.1e) and $h^* = 1$ occurs when the bubbles physically come in contact and detach.

Simultaneous growth

In figure 5.4 we compare the experimental value of the dimensionless rate of change of the bubble area ($d\bar{R}/dx$) for pairs of bubbles at distances $l = 1500$, 1000, 760, and 570 μm, with single bubble experiments at the same supersaturation conditions and pit radius. The dimensionless separation between the bubbles is defined by dividing l with twice the detachment radius of an isolated bubble, R_F

$$l^* = \frac{l}{2R_F} \tag{5.4}$$

therefore, in these experiments $l^* \approx 1.6$, 1.1, 0.8 and 0.6.

There are two pairs of symbols in each graph, corresponding to the first and second pairs of bubbles that come out of the pits. The first pair always shows a peak in the early stages of growth, which is due to the pressure drop process. Bubbles usually emerged from the pits around 10 seconds after the pressure drop began. This time depends on the size of the gas pocket trapped inside the pit. We can estimate the maximum possible size of the gas pocket –the volume of the pit– but its real size cannot be determined and furthermore, slight variations in the characteristics of the inner coating would lead to different pinning (size) of the gas cavity. Thus, the bubble is initially growing with a pressure that decreases in time, with some overshoot (about 5 kPa) and oscillation of the pressure controller before reaching stability. The second pair has a smooth rise towards the plateau, during which diffusion drives the bubble growth. The smooth rise is due to both the stability of the pressure at that point and the slower initial growth caused by local depletion. For each pair of bubbles growing simultaneously, their curves overlap, reflecting their symmetric situation. In each graph, we also show the growth rate of the second bubble from an isolated nucleation site under the same experimental conditions and the value of h^*.

Starting with the bubbles that are farthest apart ($l = 1500$ μm, figure 5.4a), we notice that their growth largely coincides with the one of an isolated bubble. However, in the final stages of growth the bubble pair curves lie slightly above that of a single bubble, starting around the time when $h^* \approx 0.5$. Although this increase is quite small, it is consistently found in all of our measurements such that we are confident

to consider it a true effect. This suggests a subtle interaction mechanism, enabled by the density-driven mixing. Apparently, the bubbles are far enough to avoid competing for the gas around them but close enough to collaborate through the mixing caused by the natural convection around them, thereby transporting depleted liquid away and bringing "fresh" liquid to their vicinity in a more efficient way.

When bubbles are closer together ($l = 1000$ μm, figure 5.4b) varied interactions appear in different stages, specially for the second pair. In this case, the initial growth rate is slowed down in more pronounced way than for an isolated bubble or two more separated ones. This is due to the combined depletion of the liquid by the previous pair (which will be treated in greater detail later in this section). Afterwards, we observe again a collaborative interaction in the earlier onset of the convective regime, which also happens around $h^* \approx 0.5$. However, this only happens for the second bubble pair, suggesting that the depletion from the previous pair also plays a role in this. Towards the end, the boundary layer of the bubbles (both the first and second pair) start interfering with each other and their growth rate stalls when $h^* \approx 0.85$.

Moving the pits a bit closer ($l = 760$ μm, figure 5.4c) we again see a slower initial growth rate of the second bubble pair with respect to the isolated one, followed by a slightly higher slope at the start of the convective regime, which once more indicates collaborative mixing. However, this starts for a larger overlap than in the previous cases ($h^* \approx 0.75$) and it ends quickly, as the bubbles get close enough to compete and stall their growth rates ($h^* \approx 0.85$). What happens at the end is somewhat intriguing: the growth rate of both bubbles becomes erratic. Our explanation for this is that the mixing at that point is no longer bringing "fresh" solution to the bubble surface, but rather liquid with non uniform gas content, leading to random variations of the growth rate. This resembles what we observed in the previous chapter for the growth of N_2 bubbles, where we conjectured that due to their very long growth times, we could no longer assume that a bubble is growing in isolation. In that case, we concluded that the uncontrollable presence of other bubbles, at distances that do not affect CO_2 bubbles, was responsible for the variations in the growth rate after a certain time.

Finally, for the shortest separation we experimented with ($l = 570$ μm, figure 5.4d) the second bubble pair does not initially grow slower than the isolated one. The bubbles in this case (and also in the previous one) are not allowed to reach their preferred detachment radius (see figure 5.5a) but rather detach when the sum of their radii is equal to the distance between them. Hence, the detachment is not due to buoyancy overcoming surface tension, but rather because the oscillations induced upon the coalescence of the bubbles that come in contact tear them from their contact lines. Their smaller detachment radius (and time) imply that the depletion of their medium is less than the other cases, which explains why the second bubble does not grow initially slower. There is no longer a collaborative interaction between these bubbles, instead they soon interfere with each other (when $h^* \approx 0.85$), and completely

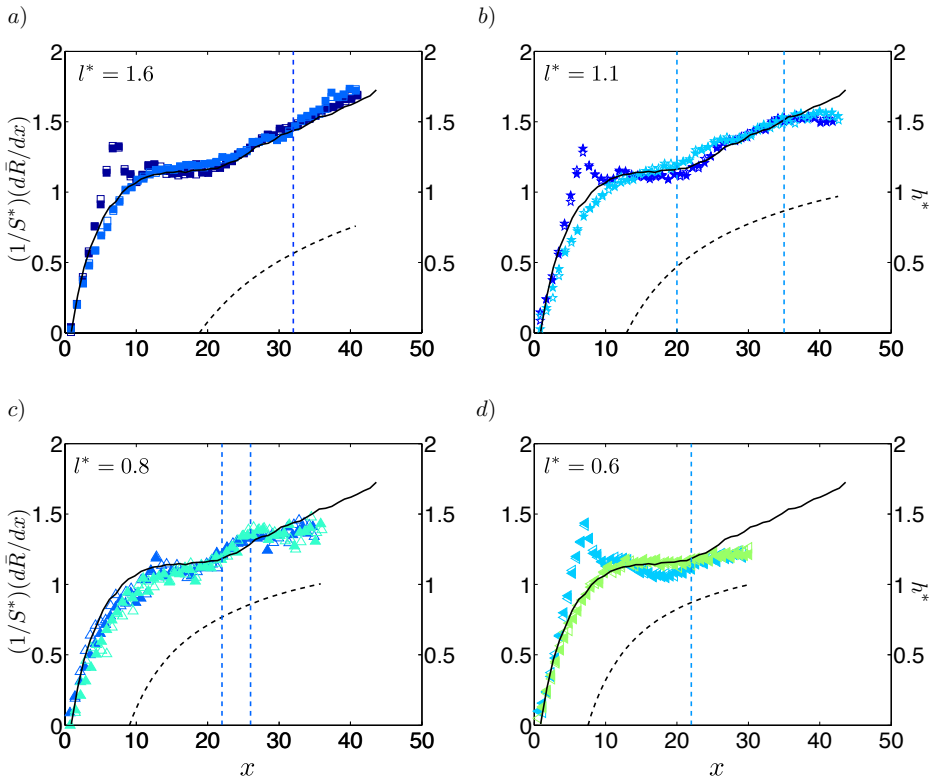

Figure 5.4: Dimensionless rate of change of the bubble area ($d\bar{R}/dx$) scaled with S^* for pairs of bubbles at distances of 1500 (a), 1000 (b), 760 (c) and 570 μm (d). Filled symbols denote the left-hand bubble and empty ones the right-hand one. The darker tone symbols in each graph correspond to the first bubble pair while the second has a lighter shade. The black solid curve in each graph is a typical example of the second (single) bubble that grows from an isolated nucleation site of the same size and under the same experimental conditions. The black dashed curve shows the dimensionless overlap h^* and the vertical dashed lines are guides for the eye indicating when the duo bubble growth starts to deviate from the single one.

avoid the development of a convective regime.

Detachment time and collective depletion

Figure 5.5b shows the relative detachment time $\tau = t_{\text{det}}(\text{exp})/t_{\text{det}}(\text{theo})$ of bubbles growing sequentially. We calculate the theoretical detachment time, $t_{\text{det}}(\text{theo})$ assuming that the bubble would grow only by diffusion, thus $R(t) \approx at^{1/2}$ (*i.e.*, the dimensional version of eq.5.2), until the measured detachment radius. The value of a is calculated with our proposed geometrical correction to the Epstein-Plesset solution to account for the slowed-down growth and is given by $a = S^*\sqrt{2D\beta}$. Bubbles that are closer to each other have longer relative detachment times. This is because the longer bubbles are "allowed" to grow in a convective regime, the more they will compensate for their initially slower growth rate. As a result of the cumulative local gas depletion, in all cases τ increases as more bubbles grow and detach from the same place. As mentioned in chapter 3 for the single bubble case, the increased detachment time is due to the initial slowing down of the growth rate, but bubbles still reach the same plateau value. After about ten bubbles, the plateau level starts to decrease as well. Since the increase of τ per number of bubbles is linear for all experiments, we find the slope for each case and plot it in figure 5.5c against the dimensionless distance between pits, $l^* = l/2R_F$. We can clearly see that for the shortest separation the slope, and hence the cumulative depletion, is the smallest. Within the experimented distances, the maximum occurs when $l = 760$ μm. When the bubbles detach without having come in contact, the depletion is quite similar to the isolated bubble, and the differences are within the error bars of our experiments.

How much two bubbles deplete their surroundings, and to what extent they influence each other through this, should be related to the amount of overlap of their concentration profiles. We make an estimation of the overlapped volume V_{ov} at the moment of detachment. This is given by two times the volume of a spherical cap of height $h/2$ on a sphere with radius $R_{\text{det}} + \delta = R_{\text{det}} + \sqrt{\pi D t_{\text{det}}}$:

$$V_{\text{ov}} = \frac{2}{3}\pi\left(\frac{h}{2}\right)^2\left[3(R_{\text{det}}+\delta) - \frac{h}{2}\right] \tag{5.5}$$

For each bubble configuration, this value is calculated by averaging t_{det} and R_{det} over the first five bubble pairs of each experiment and then averaging over all the experimental repetitions. This is done in order to smooth out the small variations in detaching radius for the cases when bubbles touch each other, caused by small differences between the time it takes each bubble to emerge from its pit (up to three seconds). For the sake of geometric simplicity, we momentarily ignore the presence of the wall, and use the uncorrected Epstein-Plesset growth rate to obtain the theoretical values to compare against. Figure 5.6 shows V_{ov} divided by V_F, the volume of a bubble that

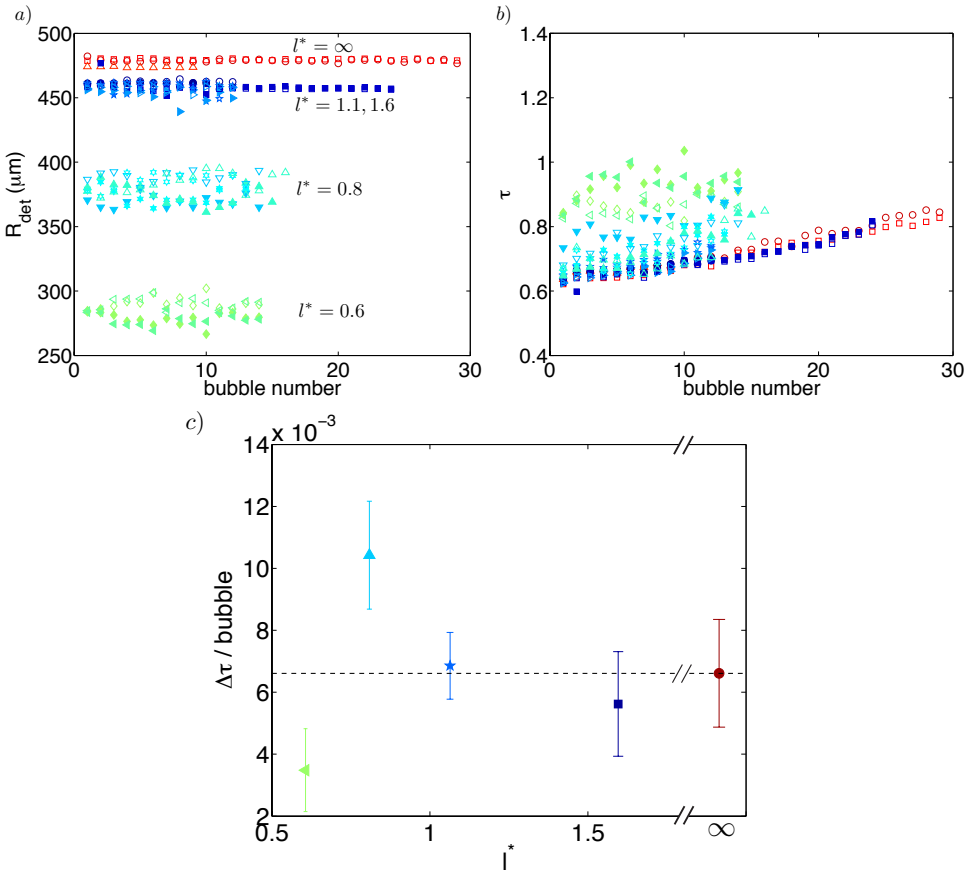

Figure 5.5: Detachment radius, R_{det}, in microns (a) and relative detachment time, $\tau = t_{\text{det}}(\text{exp})/t_{\text{det}}(\text{theo})$, (b) for pairs of bubbles at different distances and a single bubble. For bubble pairs, filled symbols correspond to the left-hand bubble and empty ones to the right-hand one. We fit lines to describe the progression of τ and plot their slope in (c) The red circle and the dotted line correspond to the measurements for a single bubble, which is denoted being infinitely far away from its neighbour.

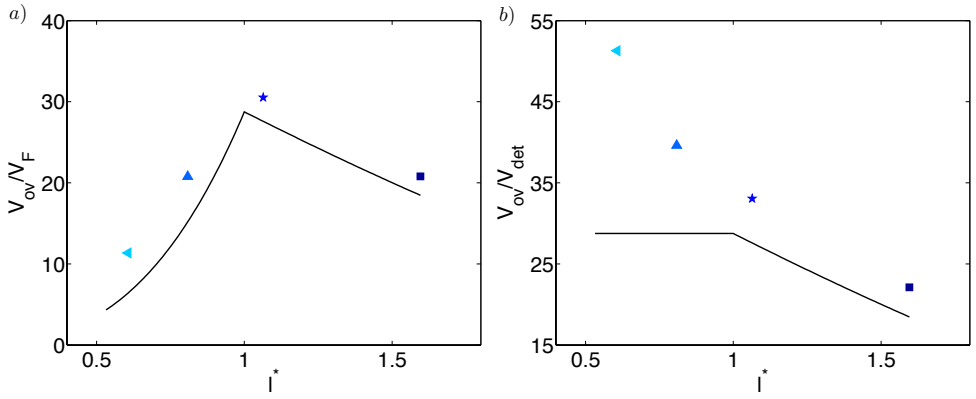

Figure 5.6: Volume of overlapping concentration profiles at the moment of bubble detachment. In (a), divided by the constant volume of a bubble detaching at R_F, and in (b) divided by the actual volume of the bubble at the detaching moment. Lines are the theoretical estimates, ignoring the presence of the substrate.

detaches with radius R_F, *i.e*, that of a single bubble growing under the same circumstances (fig.5.6a) and also divided by the actual detachment volume V_{det} (fig.5.6b). The first one makes it clear that the overlap is maximum when $l^* = 1$ and shows that our bubbles reasonably follow that trend. When divided by the real detachment volume, the left-hand part of the theoretical curve becomes constant since $V_{\text{ov}} \propto V_{\text{det}}$, and because $h/2 = \delta$ when bubbles detach at contact, dropping the dependence on l from equation 5.5 (see appendix).

5.5 Growth of three neighbouring bubbles

Now we turn to the case of three bubbles that interact while growing; experimenting with two different separations: $l = 760$ and 1000 µm and two geometrical arranges: line and equilateral triangle. As one might expect, bringing a third bubble into the relationship can complicate things and introduces different ways of interaction. The loss of symmetry in the linear configuration and the possibility for desynchronized detachment are the main causes for the new phenomena we observe.

Simultaneous growth

In figure 5.7 we compare the growth of the second triplet in each configuration against an isolated bubble. In the in-line cases (5.7a and 5.7c), during the interfering interaction the bubble in the center is clearly more affected. For the larger separation (5.7a), we see a collaborative interaction starting when $h^* \approx 0.63$; furthermore, the

three curves overlap until the onset of the interference, starting at $h^* \approx 0.82$, at which point the growth rate reduction for the central bubble is more pronounced. In the case with smaller separation (5.7b) there is a slight interfering interaction around $x = 20$, which affects more the central bubble, but which is apparently overcome by the three bubbles as they manage to enter a convective growth regime, and definitely start interfering with each other when $h^* \approx 0.69$. Again, the middle bubble is noticeably more affected. We recall that for a pair of bubbles with this separation, we observed irregular oscillations of the growth rate in the final stages. Now, the irregularity does not show up, but the oscillations do, once again suggesting an interplay of the interactions caused by interference and mixing.

For the triangular arrangements, the curves (fig.5.7b and 5.7d) reflect the symmetry of the situation, although they do not overlap as faithfully as those of the bubble pairs. This is an indication of the increased sensitivity to perturbations of the three-bubble system, which will be treated shortly. The experiment with $l = 1000$ μm (5.7b) was a special case, since a defect in the hydrophobic coating caused the bubbles to detach somewhat earlier than R_F, with radii that were slightly different from pit to pit. Still, it allows us to observe a case were bubbles interact without coming in contact. Similarly to the linear arrangement, they start a collaborative interaction, albeit less pronounced, at $h^* \approx 0.63$. However, as soon as their growth rates start to decrease, they detach. For the other triangle (5.7d), we see only interfering interaction, starting when $h^* \approx 0.70$. One of the bubbles has a noticeably slower growth rate, although it always follows the same tendency as the other two. We consistently observed that the last bubble to emerge in this triangular configuration always grew slightly more slowly than the other two.

Detachment

In the examples shown in figures 5.7a, 5.7c, and 5.7d, the three bubbles detached simultaneously. However, this is not always the case. The three bubble system is more sensitive to perturbations which may lead to desynchronized growth and detachment. We quantify the desynchronization time for a series of bubbles as:

$$t_{\mathrm{ds}} = \sum_i \left| t_{\mathrm{em}_{i,j}} - \bar{T}_{\mathrm{em}_j} \right| \tag{5.6}$$

where $t_{\mathrm{em}_{i,j}}$ is the time at which the j-th bubble emerges from pit i, and $\bar{T}_{\mathrm{em}_j}$ is the mean emergence time for the j-th bubble generation from the three pits. In figures 5.8a and 5.8c we show the desynchronization for the three-bubble lines. For the larger separation, desynchronized detachment is not so common. From the four experiments shown here, it happened only in one of them and the total t_{ds} after more than twenty bubbles is just over 300 s, *i.e.*, just over one bubble lifetime. This is to be contrasted with the shorter separation, where out of nine experiments, all of them

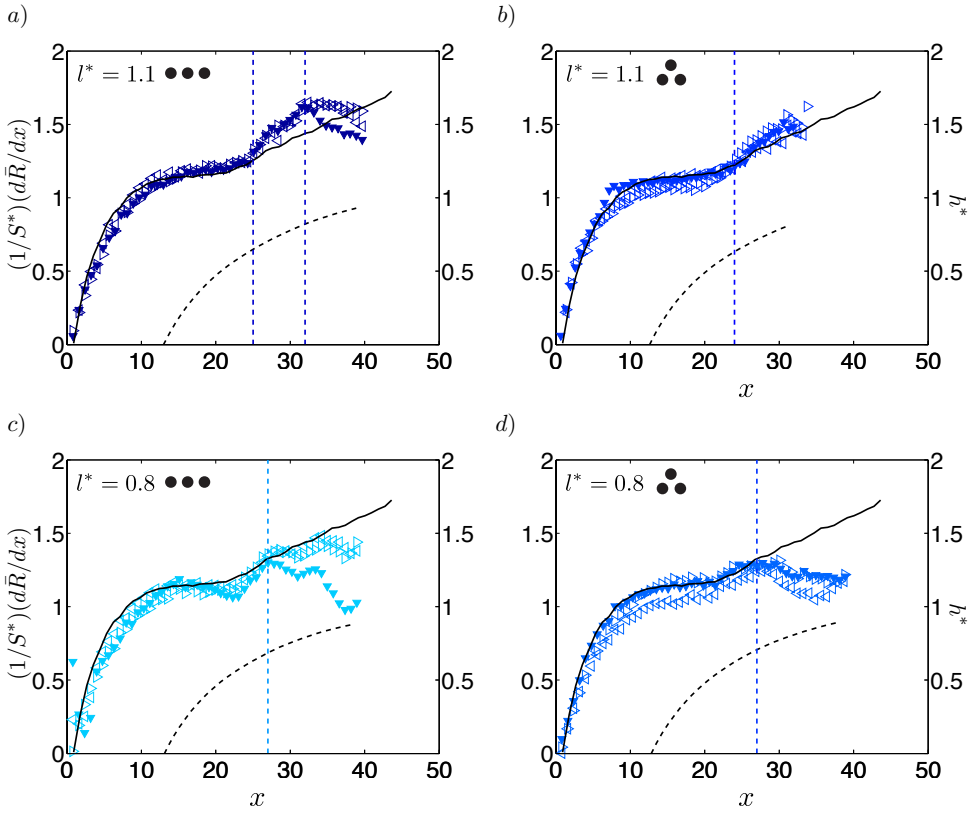

Figure 5.7: Rate of change of surface area for triplets of bubbles at distances of, 1000 (a, b) and 760 μm (c, d), arranged as lines (a, c) and equilateral triangles (b, d). Left-pointing triangles represent the left-hand bubbles, and similarly for the right-pointing ones. Filled symbols are for the middle bubble. For the triangle cases these positions have no relevance due to the symmetry of the arrange, however, we keep the same symbols representing their position in the images. We show only the second set of bubbles for each case and compare them to the corresponding isolated bubble (black solid curve). The black dashed curve shows the dimensionless overlap h^* and the vertical dashed lines are guides for the eye, indicating transitions in bubble growth characteristics.

eventually desynchronize, and t_{ds} can sometimes surpass 800 s (close to three bubble lifetimes) after twelve bubbles. For the triangular geometries we always found desynchronization for the $l = 1000$ μm case (figure 5.8b), explained by the fact that those bubbles had different preferred detachment radii (figure 5.9b). We only saw very small desynchronization for the $l = 760$ μm one, which was due to the slightly different emerging times of the bubbles, and not to variations in the detachment moment, which always happened simultaneously.

Desynchronization

What causes the desynchronization? The two most significant sources of disturbances that we have identified (besides the already complex spatial and temporal interactions between bubbles) are the slight differences between the times at which bubbles emerge from neighbouring pits, and the occasional rise of bubbles that grow in the bottom of the tank. The first one is important only when bubbles detach by coming in contact, and, of course, only for more than two bubbles. An earlier contact between two of them will cause them to detach together, and leave the other free to grow toward R_F (figure 5.9c). Bubbles that do not touch overcome such perturbations by "helping" each other to detach through the agitation they produce in the liquid upon pinching-off and rising. A neighbouring bubble that is close to the buoyancy-surface tension tipping point is prone to detach under such a disturbance. This was the case when $l = 1000$ μm (figure 5.9a) where, despite bubbles not touching each other, the central bubble was consistently forced to detach with a smaller radius. As for bubbles rising from the bottom, we have been aware of this throughout our experiments. However, it had previously not been significant since we were observing only the first and second bubbles that grow from the pits, which made it easy to verify that no such event happened during those times. In addition to this, rising bubbles will pass reasonably far away (at least 4 mm) from the pits thanks to the shielding provided by the substrate. Nonetheless, occasionally, a rising bubble passed through the field of view and we correlated it to a jump in the growth rate, which would quickly decay and go back to 'normal' (see figure 5.10c at $t \approx 2400$ s). Although we did not see this in the $l = 1000$ μm of figure 5.8a, we cannot rule out the possibility that a rising bubble might have caused the desynchronization that occurred.

The richest desynchronization phenomena occur for the in-line configuration with $l = 760$ μm. In all experimental series it eventually happened; in one occasion only after 12 triples had detached simultaneously (see square symbols in figure 5.8c) In some cases, the desynchronization even reversed (circles, downward and leftward pointing triangles in 5.8c) when the three bubbles once again detach together, and afterwards desynchronized again in an inverted way. We take a close look at one such series (the downward pointing triangles in figure 5.8c) in figure 5.10 by plotting the dimensionless mass transfer rate, represented by the Sherwood number, defined as

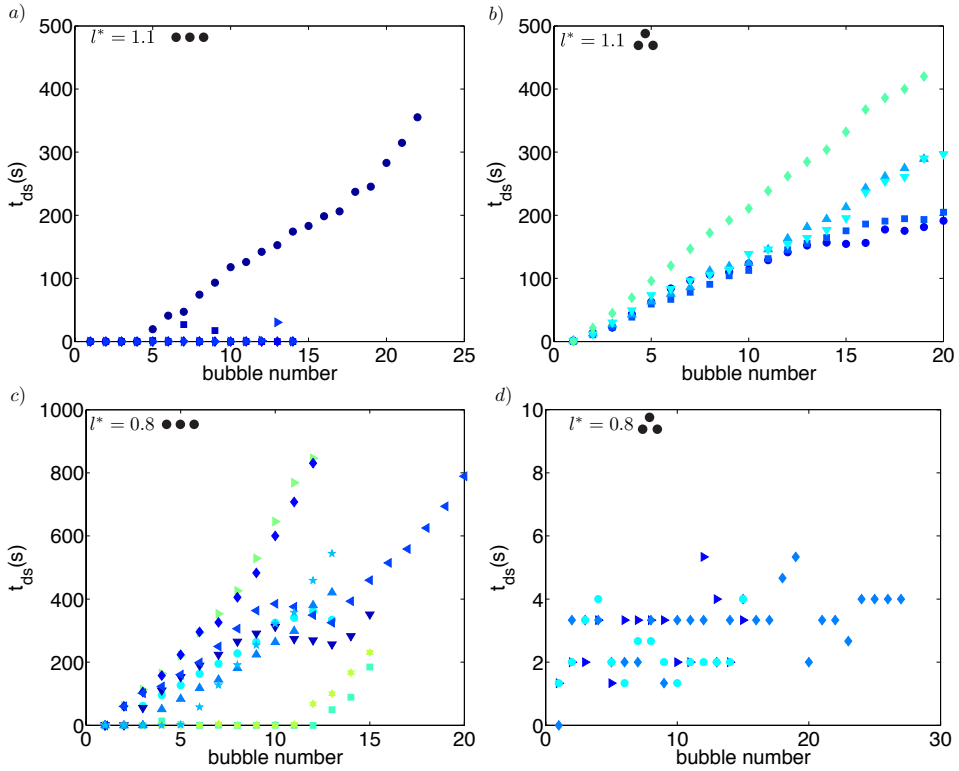

Figure 5.8: Desynchronization time for series of bubble-trios. (a) For a line with $l = 1000$ µm bubbles are usually synchronized. In one case, the bubbles became desynchronized with the detachment of the fourth triplet. From there, t_{ds} grew slowly until an amount equivalent to one bubble cycle. (b) For the triangle with $l = 1000$ µm bubbles always desynchronized since the bubble from each pit had a slightly different R_F; desynchronization is intrinsic to such a situation. (c) The line with $l = 760$ µm shows the most varied types of desynchronization and reaches the highest values. (d) The triangle with $l = 760$ µm was never seen to desynchronize, it only had small differences in the emerging time, but not in the detachment one. Each set of symbols represents one experiment.

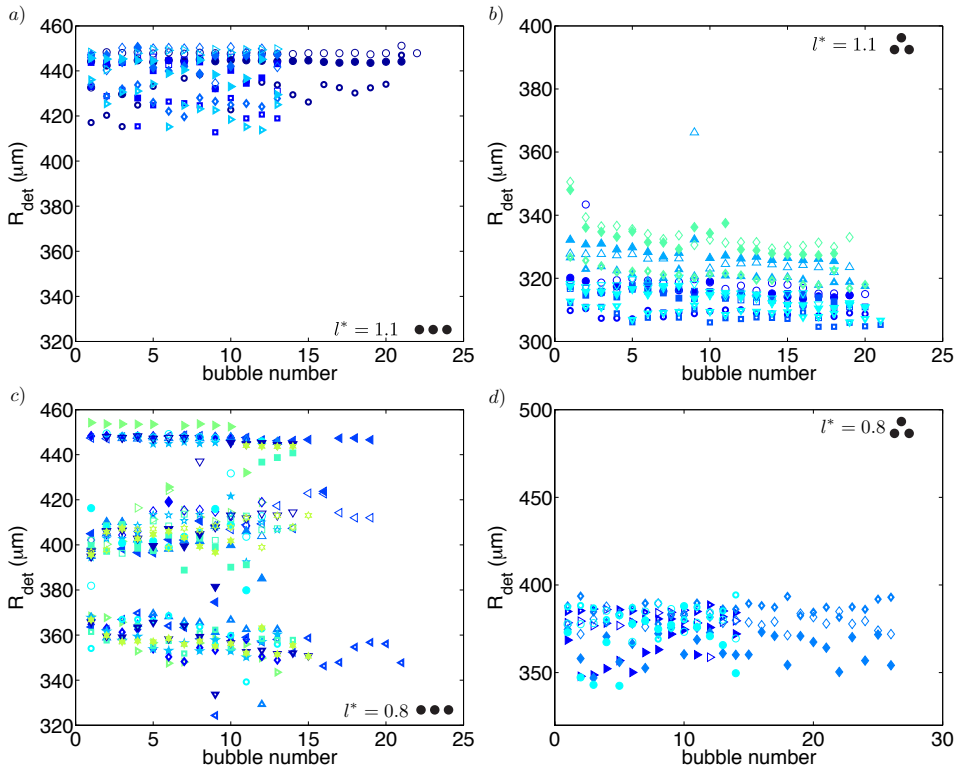

Figure 5.9: Detachment radii for trios of bubbles. (a) For a line with $l = 1000$ μm, the bubbles at the extremes always detach at $R_F \approx 450$ μm, the middle bubble, which grows slower, detaches at a smaller radius at the same time as its neighbours, due to the agitation produced by their pinch-off and rise. (b) For the triangle with $l = 1000$ μm the bubbles detach at smaller radii due to defects in the hydrophobic coating. (c) For the line with $l = 760$ μm the middle bubble always detaches with the smallest radius of the three ($R_{\text{det}} \approx 360$ μm), and it always goes at the same time as one of the extremes (with $R_{\text{det}} \approx 400$ μm). The bubble that remains can grow until R_F. (d) For the triangle with $l = 760$ μm bubbles always detach together as soon as two of them touch. Filled symbols represent the left-hand bubble, smaller, empty symbols with a thicker line the central one, and empty ones the right-hand bubble.

$\mathrm{Sh} = 2R\dot{R}/D\beta$, as a function of time for an entire series of growing and detaching bubbles. This allows us to visualize the growth of the bubbles with respect to each other when they are at different regimes, and also the effect of a detachment event on the bubble(s) that remain. These detachment events are of two kinds: double and single. In a double one, the central bubble detaches at the same time as one of the extremes while in the single event, a bubble from the extremes detaches alone. Desynchronization always starts with a double detachment and when the bubbles are synchronized both types of event happen simultaneously. Detachment events are indicated with vertical dotted lines, and labelled with the number of the event and the letters '*d*' or '*s*' according to their type.

In the first panel of figure 5.10 we see that the first bubble triplet detached simultaneously at $t \approx 200$ s. For the second triplet, the left-hand and central bubbles detach earlier (2*d*), and the right-hand bubble's mass transfer rate increases with a jump. This increase must be due to the agitation caused by the rise of its neighbours, and is maintained for the remaining 40 s of its growth until detachment, now that there is no interference from nearby bubbles. When this bubble detaches (2*s*), the other two, which are slowly growing, have a small jump. The right-hand bubble starts growing shortly after, and eventually it overtakes the central one. At the next detachment (3*d*), the growth rate of the right-hand feels again a large jump, and its mass transfer rate keeps increasing after this. Notice that the middle bubble that starts growing after (3*d*) is growing next to a large bubble with a rather high Sh, which limits it to a very slow growth rate. After detachment (3*s*) the growth rates of the three bubbles start varying somewhat irregularly. This continues all through the second panel, where we consistently see that the right-hand bubble always reaches higher values of Sh than the other two, the central bubble is mostly frustrated by its neighbours and only allowed to grow slowly, and the left-hand one grows at a rate between the other two. Notice, for example, that at (5*s*) the growth rate of the central bubble increases, while the left-hand side decreases, or that after (6*d*) the right-hand bubble feels the usual jump but its Sh sharply decreases afterwards before slightly rising again. With these oscillating growth rates, after more than 2000 s of bubble growth, the three of them detach together once again (9*d* and 8*s*). On the next cycle, they desynchronize again, but this time the right-hand and center bubbles detach together, leaving the left-hand one alone. Around $t = 2400$ s there is a clear disturbance due to a rising bubble from the bottom, that causes a peak in the three bubbles' growth rate, adding to the variations that were already taking place. Through the fourth panel, bubbles continue growing with different rates from each other, but not reaching the values of Sh that they did earlier. Finally, in the last detachment events shown, the desynchronization goes back to its initial configuration, with left-hand and middle bubbles detaching together and the right-hand one staying behind.

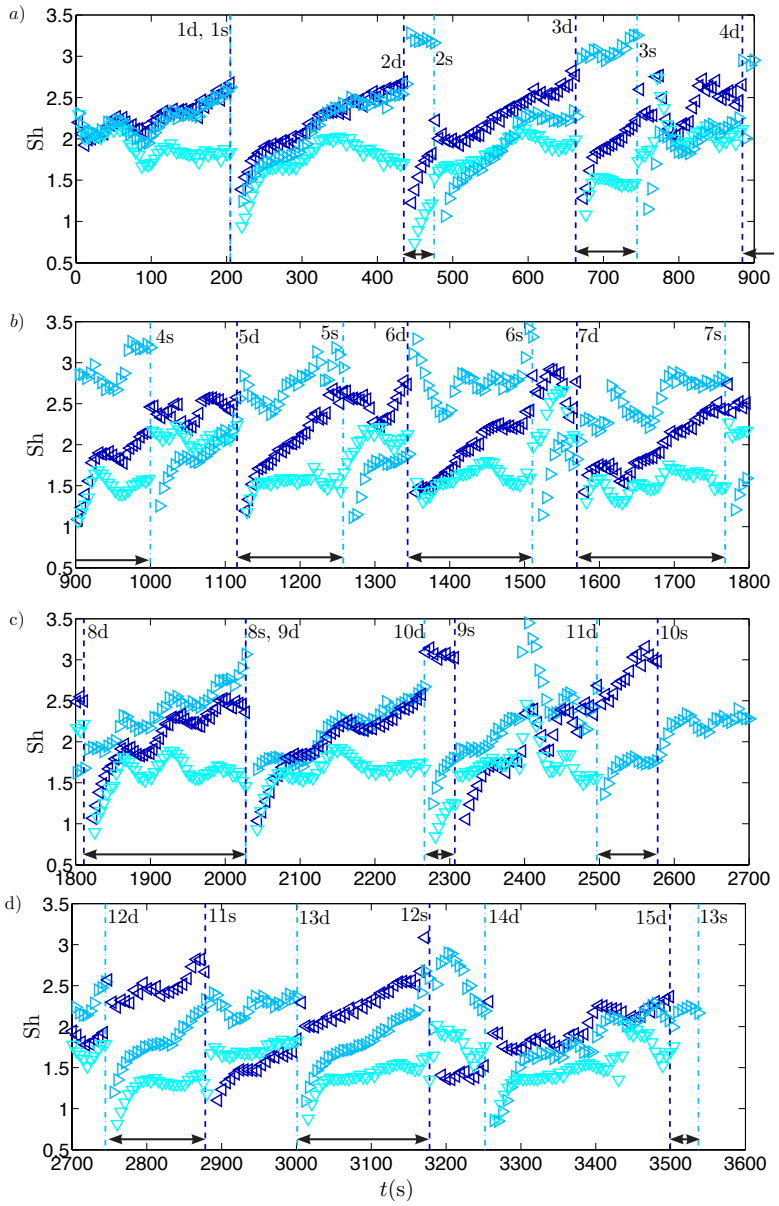

Figure 5.10: Sherwood number $\mathrm{Sh} = 2R\dot{R}/D\beta$ as function of time for each bubble in a series of desynchronized growth and detachment events from a three pit line ($l = 760$ μm) Left, down and right pointing triangles represent left, center, and right hand bubbles. Vertical lines indicate a detachment event. Such events can be of two sorts: double (labeled 'd') where the middle bubble detaches along with one from the extremes, or single (labeled 's') when the left over bubble detaches. Along with the letter indicating the type of event, we indicate its number. When the desynchronization starts, a 'd' event always takes place first. We indicate the separation between a 'd' event and its corresponding 's' event with arrows.

Collective depletion

The evolution of the detachment time for series of bubble triplets again gives us an indication of the amount of collective depletion. In figure 5.11 we see that the bubbles in triangular arrangements increase their detachment time more slowly than their linear counterparts. Also, and similarly to the line with $l = 1000$ μm, all experiments for each configuration roughly follow the same path. This is not the case for the line with $l = 760$ μm, were there are larger variations in the values and the slopes of the τ lines. In figure 5.12 we show the average of these slopes, comparing them to the single and bubble pair cases, and also to a longer line of bubbles, discussed in the next section. The slopes of the triangular configurations are averaged for the three bubbles, since they are symmetric. For the in-line cases, when $l = 1000$ μm we also average for the three positions, since the means at each position were very similar. For the line with $l = 760$ μm there was a clear difference between the central bubble, which had a higher slope, and the ones in the extremes; therefore we present them separately. With respect to the distance, we see the same tendency as in the bubble pairs: the highest slopes are found when $l = 760$ μm As for the geometry, lines have higher slopes than triangles, which somewhat surprisingly, show the same behaviour as the bubble pairs.

5.6 A longer line of bubbles

The final case we look at is a line of fourteen bubbles separated by $l = 570$ μm. Only six of them, including the one at the end, were within the field of view of our long distance microscope objective, however, this allows us to observe the main features of the arising interactions. There is one bubble that behaves clearly differently form the rest: the one at the edge (in this case at the far right), which is in the most asymmetrical position of the arrangement, having no neighbour to one side. This bubble always develops the highest growth rate (figure 5.13a), detaches at a larger size than the rest (figure 5.13b) and its detachment time increases slower in the bubble series (figure 5.13c). The second, but more subtle, different one is the bubble immediately to its left, which has the smallest detachment size (figure 5.13b) and has a slightly lower growth rate towards the end (figure 5.13a). The rest of the inner bubbles have similar behaviour to each other. For detachment, bubbles tend to arrange in pairs, sometimes in triplets. Normally, the edge bubble touches its neighbour and they detach together (figure 5.13a), allowing for a small increase of the growth rate of the next bubble to the left, which detaches with is next neighbour. The rest of the bubbles in the middle of the line usually pair up, but sometimes detach in groups of three. Except for a few exceptions (related to the simultaneous detachment of three bubbles), they detach at the same radius (about $l/2$, see figure 5.13b). As for their collective depletion, on figure 5.12 we show the slopes of the linear fits to the τ lines, once again separating

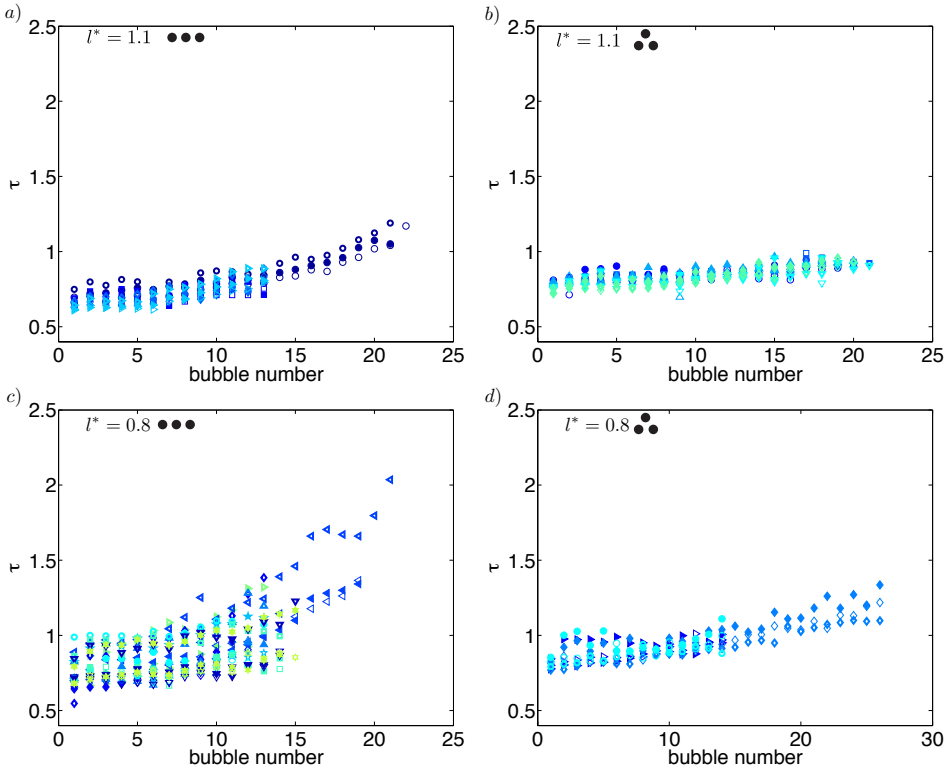

Figure 5.11: Dimensionless detachment time $\tau = t_{\mathrm{det}}(\mathrm{exp})/t_{\mathrm{det}}(\mathrm{theo})$ for series of bubble trios. For bubbles separated by $l = 1000$ µm and for the triangle with $l = 760$ µm τ increases gradually and in the same way for all experimental repetitions. In the case of the line with $l = 760$ µm, the detachment times show more variations, due to the different detachment sizes of the bubbles according to their position and their desynchronization. Filled symbols represent the left-hand bubble, smaller, empty symbols with a thicker line the central one, and empty ones the right-hand bubble.

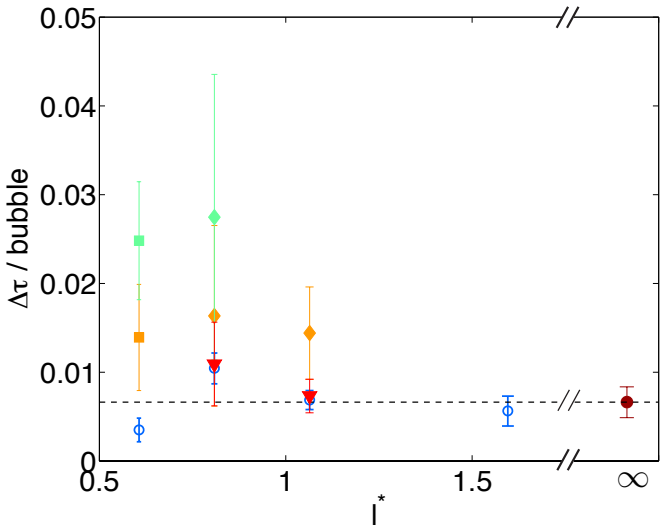

Figure 5.12: Average increase Δt of the dimensionless detachment time per detached bubble as a function of the dimensionless separation. Here we compare all the configurations studied in this work. Bubble pairs are represented by empty circles, lines by diamonds (for triplets) and squares (for the longer line), and triangles by triangles. For the cases of lines of bubbles that detach upon contact, we show separately the bubbles at the edges (orange symbols) and the ones in the center (green symbols). Triangular configurations are always averaged. The black dotted line shows the mean for the single bubble experiments ($l^* = \infty$), which are also shown by the the red filled circle.

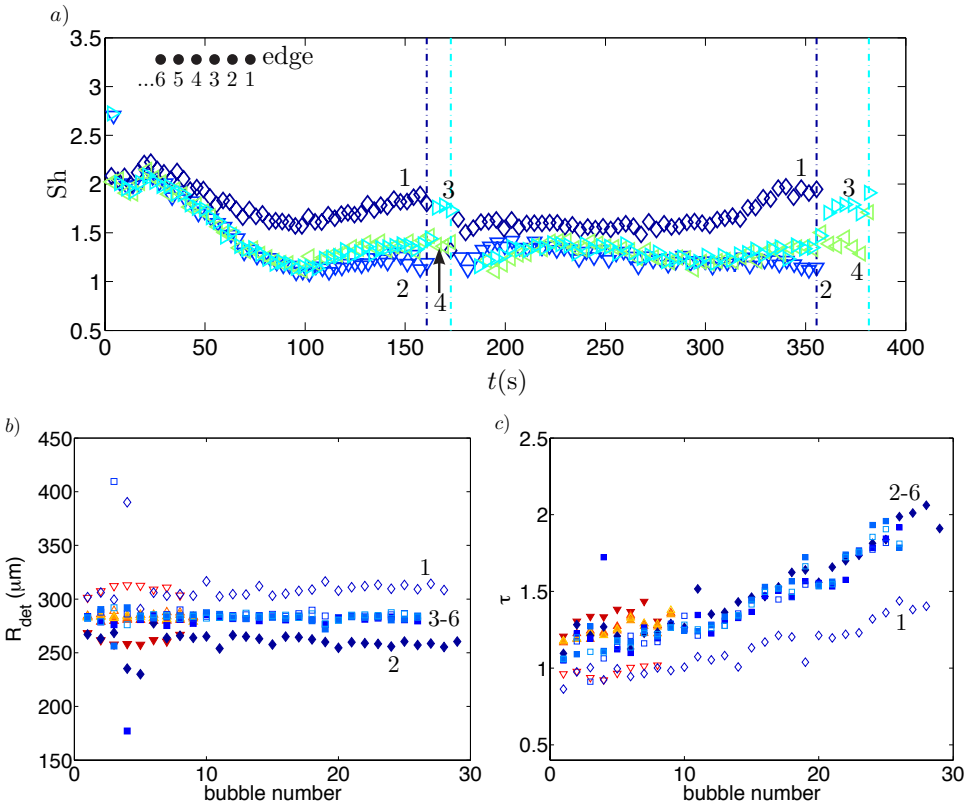

Figure 5.13: Six bubbles from a line of fourteen ($l = 570$ μm). (a) Sherwood number $\mathrm{Sh} = 2R\dot{R}/D\beta$ for the first two bubbles growing from four of the pits. The darkest symbols represent the bubble on the extreme right and downward pointing triangles its neighbour. These two detach together, and at that moment the next bubble to the left feels a jump in its growth and detaches shortly afterwards with its other neighbour. (b) Detachment radii for the six visible bubbles. The extreme right one detaches at the largest size, and its neighbour at the smallest. (c) Dimensionless detachment time. Once again, the edge bubble has a noticeably different behaviour.

the edge bubble (with a smaller slope) from the inner bubbles. The slopes are somewhat smaller than their counterparts in the triplets with $l = 760$ μm, and for the edge bubble, about the same as in the outer bubbles of the $l = 1000$ μm case.

5.7 Conclusions

We have studied the growth of bubbles that are close enough to affect each other's growth rate. The interaction between the bubbles is mediated by the overlap of the concentration profiles that develop around them. Whereas for bubbles growing exclusively by diffusion one would expect only a slowing down of the growth rates when bubbles come close enough, the development of density-driven convection allows for subtle collaborative interactions, where the bubbles actually increase their growth rate. We distinguished between interactions that take place due to bubbles growing next to each other at the same time and interactions due to gas depletion by previous bubbles. The second kind mainly provokes a progressive slowing down of subsequent bubbles. We proposed that this temporal interaction should be quantifiable by the amount of overlap of the concentration profiles, which depends on the distance between the bubbles. A theoretical estimation, considering purely diffusive growth, predicts a maximum depletion when the bubbles are separated by a distance $l = 2R_F$. However, in our experiments we find the maximum at a smaller separation ($l \approx 1.6R_F$). We conjecture that this due to the complexities in the interaction introduced by natural convection, which alters the concentration profile around the bubbles. The experimental determination of the concentration profile is beyond our means at this point, and determining it analytically –even for a single bubble– is not straightforward. Quantitative evaluation of the effects of the convective mixing will require the use of simulations.

Appendix A: Expressions for the overlapping volume

In order to calculate the overlapping volume of the concentration profiles of two adjacent growing bubbles at the moment they detach, we start from the expression describing the volume of a spherical cap of height b on a sphere with radius r

$$V_{\text{cap}} = \frac{1}{3}\pi b^2(3r - b) \tag{5.7}$$

From figure 5.1 we realize that the overlapping volume is twice the volume of a spherical cap of height $h/2 = R_{\text{det}} + \delta - l/2$ on a sphere with radius $R_{\text{det}} + \delta$; therefore

$$V_{\text{ov}} = \frac{2}{3}\pi\left(R_{\text{det}} + \delta - \frac{l}{2}\right)^2\left[3(R_{\text{det}} + \delta) - \left(R_{\text{det}} + \delta - \frac{l}{2}\right)\right] \tag{5.8}$$

For bubbles that detach upon touching each other and coalescing this expression is simplified since in that case $R_{\text{det}} = l/2$, from which

$$V_{\text{ov}} = \frac{2}{3}\pi\delta^2\left(3R_{\text{det}} + 2\delta\right) \tag{5.9}$$

Assuming a purely diffusive growth, we can substitute $R_{\text{det}} \approx a t_{\text{det}}^{1/2}$ and $\delta \approx (\pi D t_{\text{det}})^{1/2}$, where $a = S(2D\beta)^{1/2}$ (see eq. 5.1), obtaining

$$V_{\text{ov}} = \frac{2}{3}\pi^2 D\left[3a + 2(\pi D)^{1/2}\right]t^{3/2} \tag{5.10}$$

When divided by the constant value V_F (the volume of a bubble that grows until the detachment radius determined by the size of the nucleation site) this gives the rising, left-hand part of the curve in figure 5.6a. If divided by the actual detachment volume $V_{\text{det}} = 4\pi R_{\text{det}}^3/3$ we obtain

$$\frac{V_{\text{ov}}}{V_{\text{det}}} = \frac{1}{2}\frac{\pi D}{a^3}\left[3a + 2(\pi D)^{1/2}\right] \tag{5.11}$$

i.e. a constant that depends on the experimental parameter $\beta = \Delta c/\rho$ (figure 5.6b).

For bubbles that do not touch each other, $V_{\text{det}} = V_F$. Re-arranging eq. 5.8 we can write,

$$\frac{V_{\text{ov}}}{V_{\text{det}}} = \frac{(R_{\text{det}} + \delta)^3 - \frac{3}{4}l(R_{\text{det}} + \delta)^2 + \frac{l^3}{16}}{R_{\text{det}}^3} \tag{5.12}$$

In order for overlap to occur $(R_{\text{det}} + \delta) \geq l/2$, and therefore the second term in the numerator is at least three times larger than the third. Neglecting the l^3 term, and substituting the time expressions for R_{det} and δ we get

$$\frac{V_{\text{ov}}}{V_{\text{det}}} \approx \frac{\left[a + (\pi D)^{1/2}\right]^2}{a^3}\left[a + (\pi D)^{1/2} - \frac{3}{4}l t^{-1/2}\right] \tag{5.13}$$

which is a close approximation to the right-hand part of the curves in figures 5.6a and 5.6b

6

Universality of Tip Singularity Formation in Freezing Water Drops *

A drop of water deposited on a cold plate freezes into an ice drop with a pointy tip. While this phenomenon clearly finds its origin in the expansion of water upon freezing, a quantitative description of the tip singularity has remained elusive. Here we demonstrate how the geometry of the freezing front, determined by heat transfer considerations, is crucial for the tip formation. We perform systematic measurements of the angles of the conical tip, and reveal the dynamics of the solidification front in a Hele-Shaw geometry. It is found that the cone angle is independent of substrate temperature and wetting angle, suggesting a universal, self-similar mechanism that does not depend on the rate of solidification. We propose a model for the freezing front and derive resulting tip angles analytically, in good agreement with observations.

*Published as: [A.G. Marín, O.R. Enríquez, P. Brunet, P. Colinet and J.H. Snoeijer, Universality of Tip Singularity Formation in Freezing Water Drops, Physical Review Letters 113, 054301 (2014)].

6.1 Introduction

Liquid solidification can lead to intricate morphological structures, from dendritic growth [91] to the fascinating complexity of snowflakes [92]. In an apparently much simpler situation of a water drop freezing on a cold substrate, it has been observed that the final shape of the ice drop is pointy [93–96], with a sharp tip that is reminiscent of the domes of orthodox churches (figure 6.1). Intriguingly, the sharp tip appears despite the presence of liquid surface tension, which usually tends to smooth out sharp features. These singular ice drops can be observed in frozen water accretion on aircraft cabins during flights, during solidification for freeze drying purposes [58], and in recent studies on supercooling [97] and icing of substrates [98]. A similar mechanism is thought to be at the origin of the formation of spiky micro-structures following the irradiation by high-power ultra-short lasers in Germanium and Silicium substrates [99], which like water are materials that expand upon freezing.

Though the formation of pointy ice drops has been attributed to the expansion of water upon freezing, there is still no satisfactory explanation for this phenomenon. Previous studies revealed that the freezing can indeed yield a tip singularity, by modeling a planar solidification front reaching the top of the drop [93,95]. However, these theories predict a singularity only when the ratio of solid and liquid densities is below 0.75: this clearly does not explain the appearance of conical ice drops, since for water $\nu \equiv \rho_s/\rho_\ell = 0.92$. The paradox can be resolved by assuming that the freezing dynamics induces a contact angle, with a slope discontinuity at the solid/liquid/air tri-junction point that depends on the freezing rate [93].

Alternatively, the singularity was also recovered for realistic ν when numerically treating the solidification dynamics in full detail, but without the assumption of a dynamic contact angle [94, 100].

The true mechanism behind the tip singularity has therefore remained elusive, in particular since there is a lack of systematic experiments to which any of the theories can be compared.

In this chapter we reveal that the geometry of the freezing front, essentially determined by the final stages of a quasi-steady heat transfer problem, is responsible for the formation of pointy ice drops. First, we experimentally show that the cone angles at the tip are universal, and do not depend on the substrate temperature, excluding the influence of the solidification rate. Next, we reveal the boundary conditions of the solidification front by tracking the freezing process in a Hele-Shaw geometry. It is found experimentally, and explained theoretically from heat conduction, that the front develops a spherical shape that ends perpendicularly to the solid-air interface. Taking this into account into the mass balance during solidification, we then show how the singularity emerges for any density ratio $\nu < 1$. The theory predicts a cone angle $\alpha = 131^\circ$ for water drops (α defined in figure. 6.1c), which falls within the range of experimental observations.

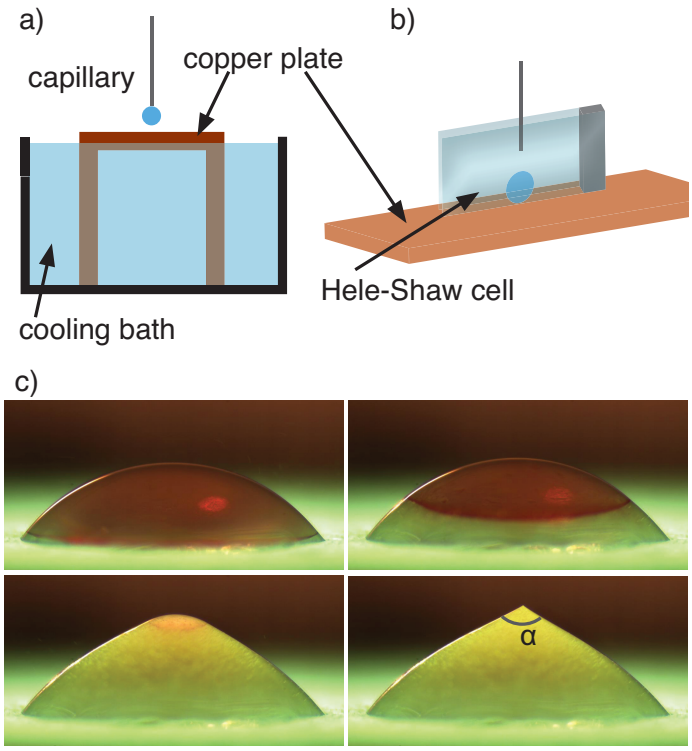

Figure 6.1: Experimental set-up. (a) Water drops are deposited on a copper plate immersed in a cooling bath of ethylene-glycol, ethanol and dry ice. (b) The shape of the advancing freezing front can be observed using a 2D-like Hele-Shaw set-up. (c) A freezing water droplet with red dye. The position of the tri-junction point is clearly visible, while the images give also give a qualitative impression of the geometry of the freezing front.

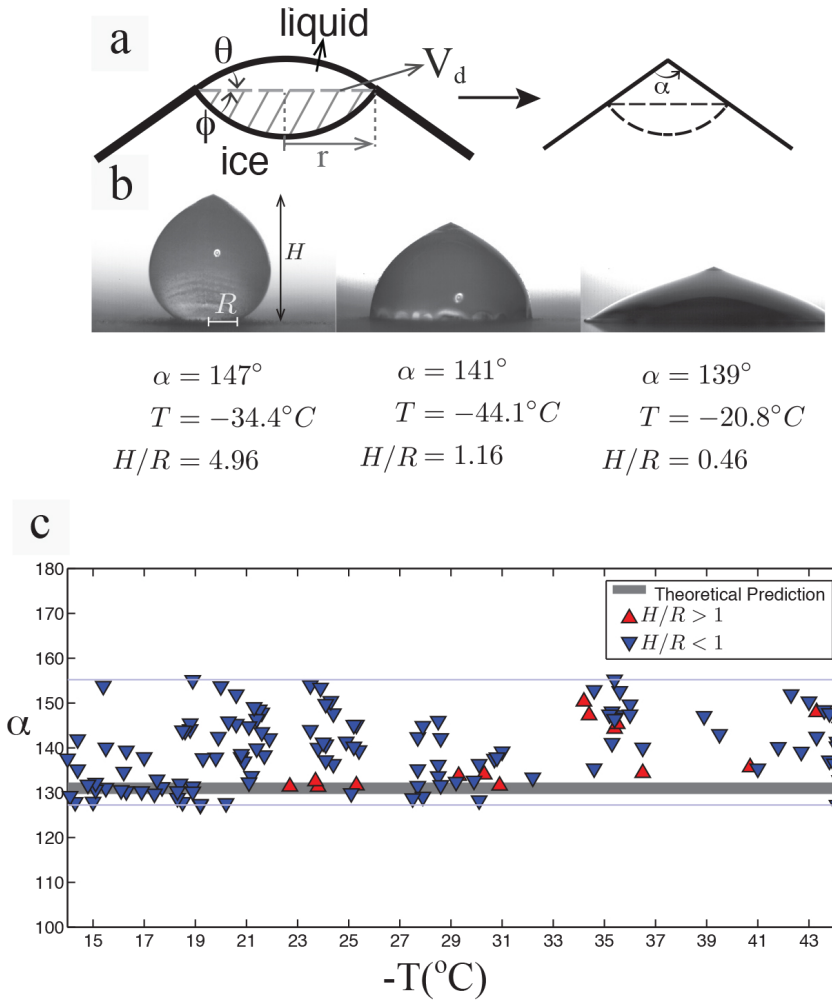

Figure 6.2: Tip formation on freezing drops. (a) Sketch of the geometry during the final stages of the freezing process. θ is the angle formed by the liquid interface with the horizontal, ϕ is that formed by the solid-frozen interface with the horizontal, and α the final tip angle. The drop radius R, and the "downward volume" V_d are also defined. (b) Drops with different contact angles (i.e. aspect ratios) are achieved by changing the deposition height, at different temperatures. (c) Measurement of the tip angle α for the full range of temperatures explored. Base-down triangles represent data from droplets at high contact angles and therefore a height-to-radius aspect ratio $H/R > 1$. Base-up triangles represent drops with low contact angle characterized by aspect ratios $H/R < 1$. We find no systematic dependence of α with global drop shape and substrate temperature. The grey line indicates the theoretical prediction (6.4).

6.2 Experiments

Droplets of pure water (milli-Q, degassed) were frozen on a copper structure that is partially immersed in a cooling bath composed of ethylene-glycol, ethanol and dry ice (figure 6.1a). With this mixture, the temperature can be controlled in the range -78 to -17°C by modifying the volume fraction of the two liquids [101]. Droplets of volume 4-8 µl were deposited using a syringe pump (Harvard Apparatus PHD ULTRA) and a 200 µm capillary. The temperature on the plate was measured near the droplet using a thermocouple. We focus here on temperatures above -44°C, for which reproducible experiments could be performed. At lower temperatures non-directional freezing and multiple freezing fronts appear. The freezing process was recorded, using a PCO camera (Sensicam QE), a long distance microscope (Edmund Optics VZM1000) and diffused back lighting, until the tip was formed.

We extracted the final shape of the drops through image analysis and fitted third-order polynomials to the left-hand and right-hand regions close to the tip. The angle of the tip is then computed as the intersecting angle of the polynomials, with an experimental error bar of $\pm 5^{\circ}$ on average. The total time for the solidification is on the order of 1 second for the coldest cases and 10 seconds for the warmest. Importantly, the liquid near the contact line freezes long before reaching the equilibrium contact angle, so that different contact angles can be achieved by varying the height of deposition. This results in drops of different aspect ratio, H/R, where H is defined as the final height of the ice drop and R the radius of the wetted area (see figure 6.2a for geometric definitions and figure 6.2b for typical droplet shapes).

Figure 6.2b shows typical shapes of ice drops, as obtained for different temperatures and contact angles. Despite the large disparity of drop shapes, the formation of the tip singularity appears to be independent of contact angle and substrate temperature. This can be inferred from figure 6.2c, where we report the cone angle α for more than 200 experiments, carried out at different temperatures (horizontal axis) and for different aspect ratios (upward/downward symbols). All measurements fall within a well-defined range of tip angles, characterized by an average and standard deviation $\alpha = 139^{\circ} \pm 8^{\circ}$. The data give no evidence for any correlation of α with temperature and aspect ratio. The experiments thus show that the tip formation is not influenced by global geometry of the drop, nor by the rate at which the solidification occurs – the latter suggesting that the singularity is the outcome of a quasi-static process. The observed variability in α is beyond the accuracy of the measurement, and appears to be due to the conditions in which the experiments where performed, *i.e.*, with the droplet exposed to air currents and vapor from the cooling bath.

6.3 Freezing front

To obtain further insight in the tip formation, we next investigate the shape of the solidification front. The still images in figure 6.1c suggest that the front does not remain planar, as was also discussed in [102, 103]. However, in order to achieve quantitative access to the advancing front, we constructed a Hele-Shaw cell with two microscope slides separated by a 1 mm spacer (figure 6.1b). The cell was placed on the copper plate and the capillary carefully maneuvered between the walls. The gap is wide enough for the drop to form a conical tip, but this is not always visible due to the presence of a wetting meniscus. To minimize image distortion due to this meniscus, the glass is treated such that the wetting contact angle $\approx 90^\circ$. This gives a clear view on the quasi-two-dimensional freezing process – typical videos can be found in the supplementary materials of [104].

Figure 6.3a shows that the solidification front in the Hele-Shaw cell grows towards the top of the drop in a similar fashion as the unconfined experiment, although the timescale of the process is a bit faster. In the first instants of the process, vapor condensates on the glass slides resulting in a "frost halo" [97] around the drop. Such event occurs simultaneously as the partial and kinetically-controlled recalescent freezing [105], also visible in figure 6.3(a) as a brighter area above the freezing front.

Our prime interest here is to extract quantitative information on the geometry of the freezing front. The front shown in figure 6.3a has a convex shape at the early stage of the freezing, while at the last stages the curvature is inverted towards a concave geometry. Interestingly, these profiles closely resemble two-dimensional numerical simulations [94]. At all times, the experimentally observed freezing front appears to be perpendicular to the ice-air interface. This is confirmed in figure 6.3c, where we present the angle $\gamma = \theta + \phi$ defined in figure 6.3b, as a function of the height z of the tri-junction point. The red line corresponds to the average over 20 experiments, performed at temperatures ranging from -30 to -15°C. We find that the front is nearly perpendicular during the entire experiment. During the final stages we find an average and standard deviation $\gamma = 87^\circ \pm 8^\circ$.

6.4 Heat-transfer-limited self-similar freezing dynamics

Coming back to the axisymmetric case we now derive the shape of the solid-liquid front from the heat transfer in the late stages of the freezing process (*cf.* figure 6.2a). We neglect any small-scale kinetic undercooling or Gibbs-Thomson effect (as considered, *e.g.*, in [100]) such that the front here always remains at the equilibrium melting temperature T_m. As the air surrounding the drop has a much smaller thermal conductivity than the solid (and the liquid), the latent heat released by the advancing front must be evacuated via the solid, while the liquid remains at uniform temper-

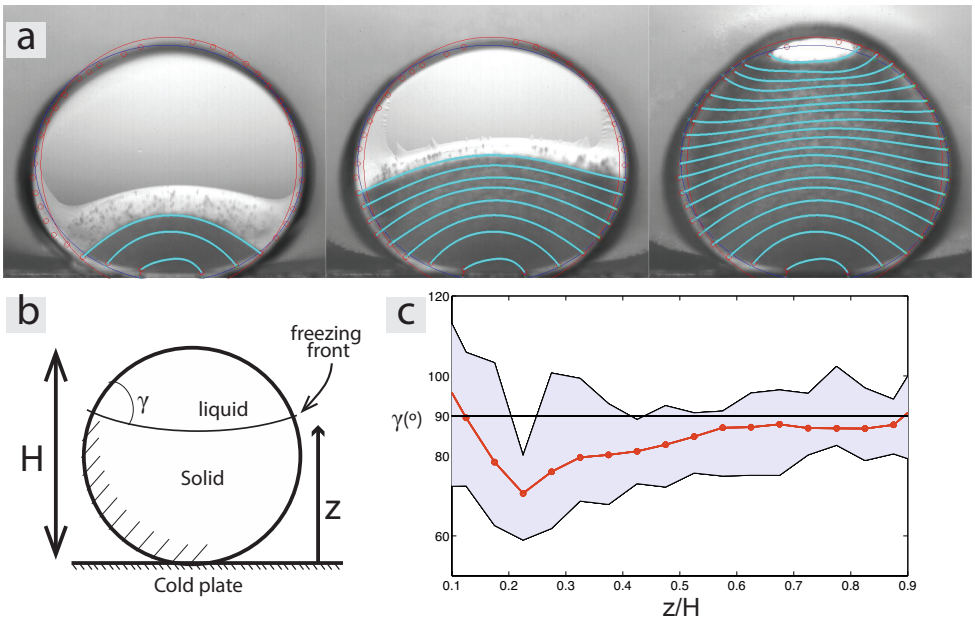

Figure 6.3: Freezing experiments with droplets sandwiched in a Hele-Shaw cell. (a) Evolution of the freezing front (green line) in different stages of the process. (b) Sketch and definitions of angles and distances. (c) Front-to-interface angle γ plotted against the relative height of the freezing front z/H. Within experimental variations, we find $\gamma \approx 90^\circ$.

ature T_m. The fact that heat cannot cross the solid-air boundary has an important consequence: it implies that the isotherms, in particular the freezing front at T_m, are locally perpendicular to the solid-air boundary, *i.e.*, $\gamma = 90^\circ$. This simple argument is in good agreement with the Hele-Shaw cell experiments, even though heat transfer via the glass slides might not be entirely negligible there.

The final stages of the heat transfer are expected to be self-similar. Namely, the angle γ made by the front with the external surface remains approximately constant, and the freezing is characterized by a single length scale, r, the radius at the triple junction. Based on this length, one can derive a scaling-law for the normal velocity v_n of the front, which is proportional to the rate at which latent heat released by the front is evacuated. This gives $v_n \sim -dr/dt \sim \lambda_s \delta T / \rho_s \mathscr{L}_m r$, where λ_s is the solid thermal conductivity, $\mathscr{L}_m$ is the latent heat of melting, and the undercooling $\delta T = T_m - T$. Here we assumed that the heat transfer process in the solid is quasi-steady, i.e. that the time scale of front motion r/v_n is much larger than the thermal diffusion time scale r^2/κ_s, where κ_s is the thermal diffusivity of the solid. Taking into account that $\kappa_s = \lambda_s/\rho_s c_{p,s}$, where $c_{p,s}$ is the thermal capacity of the solid, this is equivalent to assuming that the Stefan number $S = c_{p,s}\delta T/\mathscr{L}_m$ is small [94]. Actually, we find $S = 0.27$ for the maximal value of $\delta T = 44$ K in our experiments, such that this quasi-steadiness assumption is sufficiently accurate here (as also confirmed in figure 6.2c). Note that solving the above energy balance for r leads to a classical r^2-law, *i.e.*, r^2 decreases linearly with time during tip formation.

The above theory also provides the self-similar shape of the freezing front, which is crucial for understanding the tip formation. The heat transfer problem amounts to solving $\nabla^2 T = 0$ in the solid, with the boundary condition that the isotherms make an angle $\gamma = 90^\circ$. When the solid approaches a conical shape, the resulting isotherms are portions of concentric spheres centered at the final cone tip (figure 6.2a). The two-dimensional equivalent is that the freezing front is a portion of a circle – in good agreement with the concave shape in the final stage (figure 6.3a). This solution is stable with respect to dendrite formation given that cooling is from the solid side [91]. Hence, the front will remain spherical during the self-similar final stages of tip formation.

6.5 Geometric theory for tip formation

The results above point towards a scenario where the tip is formed by a quasi-static mechanism. Based on this, we propose a model in the spirit of [93], but taking into account the self-similar spherical geometry of the freezing front. The starting point is mass conservation

$$\frac{d}{dz}\left(V_\ell + \nu V_s\right) = 0, \tag{6.1}$$

here expressed in terms of liquid and solid volumes $V_{\ell,s}$ and density ratio ν. Since temporal dynamics is unimportant, the conservation law has been written in terms of a derivative with respect to z, the height of the tri-junction. The total liquid volume can be decomposed into a spherical cap of angle θ and a downward volume V_d (*cf.* figure 6.2a). The liquid and solid volumes then are

$$V_\ell = r^3 f(\theta) + V_d; \quad V_s = -V_d + \int_0^z dz' \, \pi r(z')^2, \tag{6.2}$$

where $r(z)$ and $\theta(z)$ are the local radius and angle of the frozen drop, and the geometry of a spherical cap gives

$$f(\theta) = \frac{\pi}{3}\left(\frac{2 - 3\cos\theta + \cos^3\theta}{\sin^3\theta}\right). \tag{6.3}$$

Closing the problem requires an expression for V_d, which in general implies a full solution of the solidification front. For the final stages, however, we can take advantage of our previous observation that the front develops a spherical shape with downward angle $\phi = \gamma - \theta$, such that $V_d = r^3 f(\gamma - \theta)$. With this, and taking into account that $dr/dz = -1/\tan\theta$, expressions (6.1–6.3) give a closed set of equations for $r(z)$, indeed predicting a sharp tip as $r \to 0$ [†]. At the singularity, θ obeys

$$f(\gamma - \theta) + f(\theta) = \nu\left[f(\gamma - \theta) + \frac{\pi}{3}\tan\theta\right], \tag{6.4}$$

from which we can infer $\alpha = \pi - 2\theta$, for any density ratio.

The central result of this analysis is that, combined with our result that $\gamma = 90°$, equation (6.4) gives a parameter-free prediction for the tip angle of ice drops: $\alpha = 131°$. This is consistent with our experimental observation $\alpha = 139° \pm 8°$, though most experiments are slightly above the theoretical prediction. We tentatively attribute the experimentally observed variability in the cone angle to variations of γ. Inserting the γ-variations measured in the Hele-Shaw cell in (6.4) indeed gives $\alpha = 133° \pm 5°$, in close agreement with experiments.

Equation (6.4) has an elegant interpretation in terms of the volumes before and after freezing. After multiplication by r^3, the left hand side represents the unfrozen liquid volume, consisting of two spherical caps. This mass is to be transformed into ice, where due to expansion factor ν the upward liquid sphere is transformed into a cone of volume $\frac{\pi}{3} r^3 \tan\theta$. The tip angle is thus determined from purely geometrical considerations. Interestingly, the model does not display a critical density ratio: a tip is formed even for $0 < 1 - \nu \ll 1$. This can be seen by expansion of (6.4), yielding a nonzero angle $\theta = \frac{12}{\pi} f(\gamma)(1 - \nu)$, in radians. This is in marked contrast with the

[†]The tip formation is obtained by taking $r \to 0$. In this limit, the asymptotic solution is of the form $\theta(r) - \theta_{\text{cone}} = A r^b$, where the sought-for cone angle θ_{cone} is given by condition (4).

model where the solidification front was assumed planar [93,95], which predicted tip formation only for ν below a critical value $3/4$.

6.6 Conclusion and outlook

This offers a fundamentally new view of freezing phenomena near free surfaces, valid beyond the ice-cone formation studied here: our findings provide the first direct measurement of the boundary condition for the freezing front, and highlight that geometric aspects are more critical than dynamical effects. The confinement of heat transfer within the solid-liquid system is a generic feature of solidification near free surfaces. The results are therefore expected to have impact on a broad variety of applications, such as icing, drop impact on cold surfaces and solidification during 3D printing.

7
Summary and outlook

In this thesis we have conducted experimental studies on two different topics: the growth of gas bubbles in slightly supersaturated liquids and the freezing of a water droplet on a cold plate, which ends with the formation of a singular tip. Both topics presented considerable experimental challenges which were both interesting and exciting to face. The bubbles had a bit of a surprise hidden for us: the important effects of the depletion layer around them, which had not been completely acknowledged before. Although they had indeed been thought about in previous works on bubble growth, they were only considered as affecting the growth of subsequent bubbles by locally depleting the solution [35]. That they might affect the growth of a bubble in 'real time' had previously been overlooked.

In Chapter 2 we have described the design and building of the experimental setup that we used for the study of growing bubbles. Essentially a soda-machine, this system allowed us to prepare a saturated solution of water with gas at a maximum pressure of 1 MPa in a short time and afterwards supersaturate the solution to the desired level in a smooth and controlled way. The silicon chips with hydrophobic pits that we manufactured worked very well as nucleation sites. With these we were able to control the number and position of bubbles in each experiment. We reported the first tests in which we made sure that the system worked as it was supposed to and presented the first observations of growing bubbles.

In Chapter 3 we observed the growth of a single bubble in a very slightly supersaturated solution. To our knowledge, no comparable experiment had been performed before. What we expected to be just a test case, where we should have measured that the bubble radius grew proportionally to $t^{1/2}$ ended up presenting us with a surpris-

ing puzzle, as we very consistently failed to recover such predicted growth rate. After convincing ourselves that there was nothing wrong with our experiment, switching our perspective from looking at R versus $t^{1/2}$ curves, to instead look at the rate of change of the bubble area as a function of $t^{1/2}$ (figure 3.2) provided a valuable clue towards the answer. This made it clear that the early part of the bubble growth was follow the expected tendency, and later on departing from it. Finally, looking at the dimensionless mass transfer rate (the Sherwood number) as a function of the mass transfer Rayleigh number (the dimensionless buoyancy caused by the concentration field around the bubble) confirmed that the mass transfer rate was being enhanced by the onset of natural convection.

In Chapter 4 we delved further into the onset of natural convection. We attempted to measure the concentration profile around the bubble by different optical means, namely Schlieren imaging and interferometry. However, the long optical path in the observation tank, combined with the very subtle difference in refractive index caused by the concentration profile made this endeavour unfruitful. A direct experimental measurement of the concentration profile would require that the experiment is confined to a Hele-Shaw geometry, which would, of course, qualitatively change the convective flow but might still allow some insight into the phenomenon. Nonetheless, by performing experiments at several supersaturations and for different initial pressures, we were able to measure the time of convection onset in different conditions. We compared this to a simple criterion to predict the onset time, which was based on the balance of buoyancy and drag forces that act on the gas-depleted region around the bubble, and found good agreement.

We have subsequently performed experiments with N_2 in response to the question of whether there would also be natural convection around bubbles of other gasses. In all our experiments, the rate of change of bubble area of N_2 bubbles initially followed the same path as for CO_2 bubbles. At the time when the transition to convective growth would have been expected, the growth of N_2 bubbles became erratic and was no longer reproducible. We attributed this to the fact that the growth times are so long that the isolation of N_2 bubbles can no longer be ensured, and interaction with bubbles growing on the edges of the substrate can become significant. However, the observed transition suggests that mixing motion does indeed occur and influences bubble growth.

In Chapter 5 we explored the simultaneous growth of bubbles. We started with the case of two bubbles and observed two kinds of interaction: a spatial one when bubbles grow next to each other at the same time, and a temporal interaction of bubbles growing from the nucleation site where other bubbles have grown and detached from before. For the spatial interaction we identified a subtle, yet consistently repeatable collaborative interaction where the convective flows around the bubbles contribute to enhance each other's growth rate with respect to the case of an isolated bubble.

After such a regime, if the bubbles are close enough, they will eventually develop an interfering interaction and slow down their growth. In order to quantify the temporal interaction, we looked at the increase in the detachment time as a series of bubbles grew and detached. The maximum effect of such interaction (*i.e.* the largest increase in detachment time per detached bubble pair) is expected to happen when the overlap between the concentration profiles of the bubbles is maximum. For purely diffusive growth, this would be when the distance between them is exactly $2R_F$, with R_F the detachment radius determined by the size of the nucleation site. However, in our experiments the maximum was found at a shorter distance, which we attribute to the influence of convection.

Then we looked at triplets of bubbles in linear and triangular arrangements. Clear differences were observable due to the symmetry, or lack thereof, of the arrangement. In lines, the bubble in the middle was clearly more affected than the ones at the extremes. The case of a bubble line where bubbles touch each other and detach due to their coalescence at that point gave rise to an interesting de-synchronization process, where usually two of the bubbles would detach together and leave the other to grow alone for a while. They were never seen to develop a steady de-synchronized stage, and therefore every experiment was different from the rest. Bubbles that do not touch each other before detaching, or in triangular arrangements were less prone to desynchronize, and when they did so it was always in a less pronounced way than the line where bubbles do touch.

In Chapter 6 we looked at the tip singularity that is formed at the end of the freezing process of a droplet on a cold plate. This presented the experimental challenge of visualizing the evolution of the freezing front, which is not really possible with conventional optical means through the surface of a spherical droplet. The crafty development of an experiment to freeze a two-dimensional droplet, allowed us to provide the first experimental measurements of the boundary conditions of the freezing front and to show that the geometrical aspects are indeed more important than the dynamic ones, therefore suggesting the universality and self-similarity of the tip formation.

In both topics we have contributed to better understand the underlying physics. In both topics there are many questions that could be tackled next. About the growing bubbles, it would be interesting to go further in the study of how they grow in confinement and close to other bubbles. Although we provided a glimpse in that direction by performing experiments where a bubble grew sandwiched between two plates, there is a long way to go towards porous materials, which is the situation where bubbles grow during oil production. The growth of hydrogen bubbles during electrolysis is another promising direction which will be taken up using our experimental set-up. This is of crucial importance in the production of hydrogen gas, which is a very important candidate for energy sources alternative to fossil fuels. Another

(opposite) direction which is interesting to pursue, and in fact is already in progress in our lab, is the dissolution of bubbles upon re-pressurization of the solution. This could again have geophysical implications, since the growth of many bubbles during oil extraction tends to re-pressurize the surroundings, but it can also be related to the stabilization of nanobubbles. Finally, one could also think about trying to tailor the interaction of bubbles in order to take advantage of the mixing they produce. This could be done by positioning nucleation sites of different sizes at such distances that would favour and maximize the subtle collaborative interactions that we observed, which might be of interest for bio-reactors where mixing at low Reynolds number is important in order to promote mass transfer but without damaging the fragile cells in there.

As for the freezing droplets there are also interesting questions to pursue. During experiments we observed that despite using degassed water, bubbles would form at the freezing front and become trapped in the ice. This could be due to atmospheric air dissolving into the liquid. The solubility of air in water increases as the latter cools down; hence, cold, degassed water is undersaturated and will tend to incorporate gas to re-establish a saturated state. Other interesting questions are what determines the arrest of the contact line and where exactly does the freezing start. We observed that, upon landing on the plate, the contact line of the droplet can oscillate before becoming arrested; however, we did not study this systematically. Finally, the solidification of other materials bears a lot of interest concerning metal drop deposition and 3D printing.

To conclude, I go back to the beginning and paraphrase Varro: *Had I possessed the leisure, Fundania, I should write in a more serviceable form what now I must set forth as I can, reflecting that I must hasten; for if man is a bubble, as the proverb has it, all the more so is a Ph.D.*

Bibliography

[1] A. Prosperetti, "Bubbles", Phys. Fluids **16**, 1852–1865 (2004).

[2] M. Varro, *De Res Rustica (Country Matters)* (Loeb Classical Library, 1934) (ca. 37 BC).

[3] R. Harris, "The bubble act: Its passage and its effects on business organization", J. Econ. Hist. **54**, 610–627 (1994).

[4] P. M. Garber, "Famous first bubbles", J. Econ. Perspect. **4**, 35–54 (1990).

[5] J. Magnaudet and I. Eames, "The motion of high-reynolds-number bubbles in inhomogeneous flows", Annu Rev. Fluid Mech. **32**, 659–708 (2000).

[6] M. P. Brenner, S. Hilgenfeldt, and D. Lohse, "Single-bubble sonoluminescence", Rev. Mod. Phys. **74**, 425–484 (2002).

[7] V. Ajaev and G. Homsy, "Modelling shapes and dynamics of confined bubbles", Annu. Rev. of Fluid Mech. **38**, 277–307 (2006).

[8] S. Thoroddsen, T. Etoh, and K. Takehara, "High-speed imaging of drops and bubbles", Annu. Rev. Fluid Mech. **40**, 257–285 (2008).

[9] R. S. J. Sparks, "The dynamics of bubble formation and growth in magmas: A review and analysis", J. Volcanol. Geotherm. Res. **3**, 1 – 37 (1978).

[10] A. A. Prousevitch, D. L. Sahagian, and A. T. Anderson, "Dynamics of diffusive bubble growth in magmas: Isothermal case", J. Geophys. Res-Sol. Ea. **98**, 22283–22307 (1993).

[11] P. Papale, "Strain-induced magma fragmentation in explosive eruptions", Nature **397**, 425–428 (1999).

[12] J. Blower, J. Keating, H. Mader, and J. Phillips, "The evolution of bubble size distributions in volcanic eruptions", J. Volcanol. and Geoth. Res. **120**, 1 – 23 (2003).

[13] M. A. Chappell and S. J. Payne, "A physiological model of the release of gas bubbles from crevices under decompression", Respir. Physiol. Neurobiol. **153**, 166 – 180 (2006).

[14] V. Papadopoulou, R. J. Eckersley, C. Balestra, T. D. Karapantsios, and M.-X. Tang, "A critical review of physiological bubble formation in hyperbaric decompression", Adv. Colloid Interfac **191192**, 22 – 30 (2013).

[15] A. L. Klibanov, "Ultrasound contrast agents: Development of the field and current status", in *Contrast Agents II*, edited by W. Krause, volume 222 of *Topics in Current Chemistry*, 73–106 (Springer Berlin Heidelberg) (2002).

[16] S. Mitragotri, "Healing sound: the use of ultrasound in drug delivery and other therapeutic applications", Nat. Rev. Drug Discov. **4**, 255–260 (2005).

[17] P. C. Munasinghe and S. K. Khanal, "Biomass-derived syngas fermentation into biofuels: opportunities and challenges", Bioresource technology **101**, 5013–5022 (2010).

[18] J. K. Edzwald, "Principles and applications of dissolved air flotation", Water Sci. Technol. **31**, 1–23 (1995).

[19] M. Cable and J. R. Frade, "Diffusion-controlled growth of multi-component gas bubbles", J. Mater. Sci. **22**, 919–924 (1987).

[20] M. Cable and J. R. Frade, "The influence of surface tension on the diffusion-controlled growth or dissolution of spherical gas bubbles", P. Roy. Soc. of Lond. A. Mat. **420**, 247 (1988).

[21] G. Y. Gor and A. E. Kuchma, "Steady-state composition of a two-component gas bubble growing in a liquid solution: Self-similar approach", J. Chem. Phys. **131**, 234705 (2009).

[22] M. Amon and C. D. Denson, "A study of the dynamics of foam growth: analysis of the growth of closely spaced spherical bubbles", Polym. Eng. Sci. **24**, 1026–1034 (1984).

[23] M. A. Shafi and R. W. Flumerfelt, "Initial bubble growth in polymer foam processes", Chem. Eng. Sci. **52**, 627–633 (1997).

[24] D. C. Venerus, "Diffusion–induced bubble growth in viscous liquids of finite and infinite extent", Polym. Eng. Sci. **41**, 1390–1398 (2001).

[25] M. Favelukis, "Dynamics of foam growth: Bubble growth in a limited amount of liquid", Polym. Eng. Sci. **44**, 1900–1906 (2004).

[26] J. B. Condon and T. Schober, "Hydrogen bubbles in metals", J. Nucl. Mater. **207**, 1–24 (1993).

[27] A. McBirney and T. Murase, "Factors governing the formation of pyroclastic rocks", Bulletin Volcanologique **34**, 372–384 (1970).

[28] O. R. Enríquez, C. Hummelink, G.-W. Bruggert, D. Lohse, A. Prosperetti, D. van der Meer, and C. Sun, "Growing bubbles in a slightly supersaturated solution", Rev. Sci. Instrum. **84** (2013).

[29] H. N. Oguz and A. Prosperetti, "Dynamics of bubble growth and detachment from a needle", J. Fluid Mech. **257**, 111–145 (1993).

[30] A. Prosperetti and H. N. Oguz, "The impact of drops on liquid surfaces and the underwater noise of rain", Annu. Rev. of Fluid Mech. **25**, 577–602 (1993).

[31] R. Bergmann, D. van der Meer, M. Stijnman, M. Sandtke, A. Prosperetti, and D. Lohse, "Giant bubble pinch-off", Phys. Rev. Lett. **96**, 154505 (2006).

[32] D. E. Westerheide and J. W. Westwater, "Isothermal growth of hydrogen bubbles during electrolysis", AIChE Journal **7**, 357–362 (1961).

[33] J. P. Glas and J. W. Westwater, "Measurements of the growth of electrolytic bubbles", Int. J. Heat Mass Transfer **7**, 1427–1443 (1964).

[34] A. Prins and K. Van't Riet, "Proteins and surface effects in fermentation: foam, antifoam and mass transfer", Trends Biotechnol. **5**, 296–301 (1987).

[35] S. Jones, G. Evans, and K. Galvin, "Bubble nucleation from gas cavities–a review", Adv. Colloid Interface Sci. **80**, 27–50 (1999).

[36] A. A. Atchley and A. Prosperetti, "The crevice model of bubble nucleation", J. Acoust. Soc. Am. **86**, 1065 (1989).

[37] R. Cole, "Boiling nucleation", Adv. Heat Transfer **10**, 85–166 (1974).

[38] C. G. J. Bisperink and A. Prins, "Bubble growth in carbonated liquids", Colloids Surf., A **85**, 237–253 (1994).

[39] G. S. Barker, B. Jefferson, and S. J. Judd, "The control of bubble size in carbonated beverages", Chem. Eng. Sci. **57**, 565–573 (2002).

[40] G. Liger-Belair, "The physics and chemistry behind the bubbling properties of champagne and sparkling wines: A state-of-the-art review", J. Agric. Food Chem. **53**, 2788–2802 (2005).

[41] K. K. Sahu, Y. Hazama, and K. N. Ishihara, "Gushing in canned beer: The effect of ultrasonic vibration", J. Colloid Interface Sci. **302**, 356–362 (2006).

[42] W. T. Lee, J. S. McKechnie, and M. G. Devereux, "Bubble nucleation in stout beers", Phys. Rev. E **83**, 051609 (2011).

[43] M. Pooladi-Darvish and A. Firoozabadi, "Solution-gas drive in heavy oil reservoirs", J. Can. Pet. Technol. **38**, 54–61 (1999).

[44] S. Akin and A. R. Kovscek, "Heavy-oil solution gas drive: a laboratory study", J. Petrol. Sci. Eng. **35**, 33–48 (2002).

[45] D. D. Joseph, A. M. Kamp, and R. Bai, "Modeling foamy oil flow in porous media", Int. J. Multiphas Flow **28**, 1659–1686 (2002).

[46] P. Arora and A. R. Kovscek, "A mechanistic modeling and experimental study of solution gas drive", Transport in Porous Media **51**, 237–265 (2003).

[47] I. Bondino, S. R. Mcdougall, and G. Hamon, "A pore-scale modelling approach to the interpretation of heavy oil pressure depletion experiments", Journal of Petroleum Science and Engineering **65**, 14–22 (2009).

[48] S. Uzel and M. Chappell, "Modeling the cycles of growth and detachment of bubbles in carbonated beverages", J. Phys. Chem. B **110**, 7579–7586 (2006).

[49] A. L. Yarin, "Drop impact dynamics: splashing, spreading, receding, bouncing", Annu. Rev. Fluid Mech. **38**, 159–192 (2006).

[50] S. T. Thoroddsen, "The making of a splash", J. Fluid Mech. **690**, 1–4 (2012).

[51] L. V. Zhang, J. Toole, K. Fezzaa, and R. D. Deegan, "Evolution of the ejecta sheet from the impact of a drop with a deep pool", J. Fluid Mech. **690**, 5–15 (2012).

[52] H. Katsuragi, "Morphology scaling of drop impact onto a granular layer", Phys. Rev. Lett. **104**, 218001 (2010).

[53] B.-J. de Gans, P. C. Duineveld, and U. S. Schubert, "Inkjet printing of polymers: state of the art and future developments", Advanced Materials **16**, 203–213 (2004).

[54] A. L. Biance, C. Clanet, and D. Quéré, "Leidenfrost drops", Physics of Fluids **15**, 1632–1637 (2003).

[55] H. Lhuissier, Y. Tagawa, T. Tran, and C. Sun, "Levitation of a drop over a moving surface", J. Fluid Mech. **733**, R4 (2013).

[56] D. L. Frost, "Dynamics of explosive boiling of a droplet", Physics of Fluids **31**, 2554–2561 (1988).

[57] Z. Liu, Y. Gou, J. Wang, and S. Cheng, "Frost formation on a super-hydrophobic surface under natural convection conditions", Int. J. Heat Mass Tran. 5975–5982 (2008).

[58] J. D. Mellor *et al.*, *Fundamentals of freeze-drying.* (Academic Press Inc.(London) Ltd.) (1978).

[59] F. Kuni and I. A. Zhuvikina, "A theory of homogeneous boiling-up of liquid solutions: 1. kinetic equation of boiling-up", Colloid J. **64**, 166–171 (2002).

[60] I. A. Zhuvikina and F. M. Kuni, "A theory of the homogeneous boiling-up of liquid solutions. 2. the steady-state rate of boiling-up", Colloid J. **64**, 556–561 (2002).

[61] F. M. Kuni, I. A. Zhuvikina, and A. P. Grinin, "A theory of homogeneous boiling-up of liquid solutions: 3. growth of supercritical bubbles with allowance for solvent fugacity", Colloid J. **65**, 201–205 (2003).

[62] S. D. Lubetkin, "Why is it much easier to nucleate gas bubbles than theory predicts?", Langmuir **19**, 2575–2587 (2003).

[63] P. M. Wilt, "Nucleation rates and bubble stability in water-carbon dioxide solutions", J. Colloid Interface Sci. **112**, 530 – 538 (1986).

[64] S. F. Jones, G. M. Evans, and K. P. Galvin, "The cycle of bubble production from a gas cavity in a supersaturated solution", Adv. Colloid Interface Sci. **80**, 51–84 (1999).

[65] M. Hey, A. Hilton, and R. D. Bee, "The formation and growth of carbon dioxide gas bubbles from supersaturated aqueous solutions", Food Chem. 349–357 (1994).

[66] T. S. Light, E. A. Kingman, and A. C. Bevilacqua, "The conductivity of low concentrations of CO_2 dissolved in ultrapure water from 0-100 °C", in *209th American Chemical Society National Meeting* (Anaheim, CA) (1995).

[67] H. Jansen, M. Boer, R. Legtenberg, and M. Elwenspoek, "The black silicon method: a universal method for determining the parameter setting of a fluorine-based reactive ion etcher in deep silicon trench etching with profile control", J. Micromech. Microeng. **5**, 115 (1995).

[68] B. Borkent, S. Gekle, A. Prosperetti, and D. Lohse, "Nucleation threshold and deactivation mechanisms of nanoscopic cavitation nuclei", Phys. Fluids **21** (2009).

[69] P. W. Atkins, *Physical Chemistry* (Oxford University Press) (1978).

[70] D. R. Lide and H. P. R. Frederikse, *CRC Handbook of Chemistry and Physics* (CRC Press, Inc.) (1995).

[71] W. Fritz, "Berechnung des maximale volume von dampfblasen.", Phys. Z. **36**, 379–384 (1935).

[72] P. S. Epstein and M. S. Plesset, "On the stability of gas bubbles in liquid-gas solutions", J. Chem. Phys. **18** (1950).

[73] E. Lindeberg and D. Wessel-Berg, "Vertical convection in an aquifer column under a gas cap of CO_2", Energy Convers. Manage. **38, Supplement**, S229 – S234 (1997).

[74] L. A. Crum and Y. Mao, "Acoustically enhanced bubble growth at low frequencies and its implications for human diver and marine mammal safety", J. Acoust. Soc. Am. **99**, 2898–2907 (1996).

[75] L. E. Scriven, "On the dynamics of phase growth", Chem. Eng. Sci. **10**, 1–13 (1959).

[76] S. D. Lubetkin and M. Akhtar, "The variation of surface tension and contact angle under applied pressure of dissolved gases, and the effects of these changes on the rate of bubble nucleation", J. Colloid Interface Sci. **180**, 43–60 (1996).

[77] A. Bejan, *Heat Transfer* (John Wiley ans Sons, Inc.) (1993).

[78] J. Li, H. Chen, W. Zhou, B. Wu, S. D. Stoyanov, and E. G. Pelan, "Growth of bubbles on a solid surface in response to a pressure reduction", Langmuir **30**, 4223–4228 (2014).

[79] O. R. Enríquez, C. Sun, D. Lohse, A. Prosperetti, and D. van der Meer, "The quasi-static growth of CO_2 bubbles", J. Fluid Mech. **741**, R1 (2014).

[80] G. Liger-Belair, "Physicochemical approach to the effervescence in champagne wines.", Ann. Phys. Fr. **27**, 1–106 (2002).

[81] X. Li and Y. C. Yortsos, "Theory of multiple bubble growth in porous media by solute diffusion", Chem. Eng. Sci. **50**, 1247–1271 (1995).

[82] I. N. Tsimpanogiannis and Y. C. Yortsos, "The critical gas saturation in a porous medium in the presence of gravity", J. Colloid Interf. Sci. **270**, 388–395 (2004).

[83] L. Zuo, S. Krevor, R. W. Falta, and S. M. Benson, "An experimental study of CO_2 exsolution and relative permeability measurements during CO_2 saturated water depressurization", Transp. Porous Med. **91**, 459–478 (2012).

[84] T. Karapantsios, M. Kostoglou, and N. Divinis, "Nucleation, growth and detachment of neighboring bubbles over miniature heaters", Chem. Eng. Sci. **63**, 3438–3448 (2008).

[85] N. Divinis, T. D. Karapantsios, M. Kostoglou, C. S. Panoutsos, V. Bontozoglou, A. C. Michels, M. C. Sneep, R. D. Bruijn, and H. Lotz, "Bubbles growing in supersaturated solutions at reduced gravity", AIChE J. **50**, 2369–2382 (2004).

[86] W. M. Buehl and J. W. Westwater, "Bubble growth by dissolution: influence of contact angle", AIChE J. **12**, 571–576 (1966).

[87] N. Godino, X. Borris, F. Muoz, F. del Campo, and R. Compton, "Mass transport to nanoelectrode arrays and limitations of the diffusion domain approach: Theory and experiment", Phys. Chem. C **113**, 11119–11125 (2009).

[88] P. Ugo, L. M. Moretto, M. D. Leo, A. P. Doherty, C. Vallese, and S. Pentlavalli, "Diffusion regimes at nanoelectrode ensembles in different ionic liquids", Electrochim. Acta **55**, 2865 – 2872 (2010).

[89] E. Ben-Jacob and P. Garik, "The formation of patterns in non-equilibrium growth", Nature **343**, 523–530 (1990).

[90] P. W. Voorhees, "The theory of ostwald ripening", J. Stat. Phys. **38**, 231–252 (1985).

[91] M. Glicksman, *Principles of solidification* (Springer - New York) (2002).

[92] K. G. Libbrecht, "The physics of snow crystals", Rep. Prog. Phys. **68**, 855–895 (2005).

[93] D. M. Anderson, M. G. Worster, and D. S. H., "The case for a dynamic contact angle in containerless solidification", J. Cryst. Growth **163**, 329–338 (1996).

[94] V. S. Ajaev and S. H. Davis, "Boundary-integral simulations of containerless solidification", J. Comp. Phys. **187**, 492–503 (2003).

[95] J. H. Snoeijer and P. Brunet, "Pointy ice-drops: How water freezes into a singular shape", Am. J. Phys. **80**, 764 (2012).

[96] O. R. Enriquez, A. G. Marin, K. G. Winkels, and J. H. Snoeijer, "Freezing singularities in water drops", Phys. Fluids **24**, 091102 (2012).

[97] S. Jung, M. Tiwari, and D. Poulikakos, "Frost halos from supercooled water droplets", Proceedings of the National Academy of Sciences **109** (2012).

[98] S. Jung, M. Dorrestijn, D. Raps, A. Das, C. M. Megaridis, and D. Poulikakos, "Are Superhydrophobic Surfaces Best for Icephobicity?", Langmuir **27**, 3059–3066 (2011).

[99] K. W. Kolasinski, "Solid structure formation during the liquid/solid phase transition", Curr. Op. Sol. St. Mat. Sci. **11**, 76–85 (2007).

[100] V. S. Ajaev and S. H. Davis, "The effect of tri-junction conditions in droplet solidification", J. Cryst. Growth **264**, 452–462 (2004).

[101] C. M. Jensen and D. W. Lee, "Dry-ice bath based on ethylene glycol mixtures", Journal of Chemical Education **77**, 629 (2000).

[102] M. Nauenberg, "Comment on "pointy ice-drops: How water freezes into a singular shape"", Am. J. Phys. **81**, 150 (2013).

[103] J. H. Snoeijer and P. Brunet, "Response to "comment on pointy ice-drops: How water freezes into a singular shape"", Am. J. Phys. **81**, 151 (2013).

[104] A. G. Marín, O. R. Enríquez, P. Brunet, P. Colinet, and J. H. Snoeijer, "Universality of tip singularity formation in freezing water drops", Phys. Rev. Lett. **113**, 054301 (2014).

[105] P. Kavehpour, S. Davis, and F. Tavakoli, "When a water drop freezes before it solidifies", Bulletin of the American Physics Society, Division of Fluid Dynamics (2012).

List of Publications

- **2014:** Universality of tip singularity formation in freezing water drops
  Á. Gómez Marín, O.R. Enríquez, P. Brunet, P. Colinet, and J.H. Snoeijer, Phys. Rev. Lett. 113, 054301

- **2014:** The quasi-static growth of CO_2 bubbles
  O.R. Enríquez, C. Sun, D. Lohse, A. Prosperetti, and D. van der Meer, J. Fluid Mech. 741, R1

- **2013:** Deactivation of Microbubble Nucleation Sites by Alcohol–Water Exchange
  X. Zhang, H.E. Lhuissier, O.R. Enríquez, C. Sun, and D. Lohse, Langmuir 29, 9979–9984

- **2013:** Growing bubbles in a slightly supersaturated liquid solution
  O.R. Enríquez, C. Hummelink, G.W.H. Bruggert, D. Lohse, A. Prosperetti, D. van der Meer, and C. Sun, Rev. Sci. Instrum. 84, 065111

- **2012:** Freezing singularities in water drops
  O.R. Enríquez, Á. Gómez Marín, K.G. Winkels, and J.H. Snoeijer, Phys. Fluids 24, 091102

- **2012:** Collapse and pinch-off of a non-axisymmetric impact-created air cavity in water
  O.R. Enríquez, I.R. Peters, S. Gekle, L.E. Schmidt, D. Lohse, and D. van der Meer, J. Fluid Mech. 701, 4058

- **2011:** Non-axisymmetric impact creates pineapple-shaped cavity
  O.R. Enríquez, I.R. Peters, S. Gekle, L.E. Schmidt, D. van der Meer, and D. Lohse, Phys. Fluids 23, 091106

- **2010:** Collapse of nonaxisymmetric cavities
  O.R. Enríquez, I.R. Peters, S. Gekle, L.E. Schmidt, M. Versluis, D. van der Meer, and D. Lohse, Phys. Fluids 22, 091104

Samenvatting

In dit proefschrift hebben we twee verschillende onderwerpen experimenteel bestudeerd: de groei van de gasbellen in licht oververzadigde vloeistoffen en het bevriezen van waterdruppels op een koude plaat; een proces dat eindigt met de vorming van een bijzondere tip. Beide onderwerpen bevatten grote experimentele uitdagingen die zowel wetenschappelijk interessant als spectaculair om te zien zijn. De bellen stelden ons voor een verrassing: het grote effect van de depletielaag om hen heen was tot op heden onbekend. In eerdere studies beschouwde men de rol van de depletielaag wel, maar enkel als zijnde van invloed op groei van de opvolgende luchtbellen door het plaatselijk be invloeden van het concentratieveld [35]. Dat de depletielaag ook de groei van een bel in "real time"zou kunnen be invloeden was echter tot nu toe over het hoofd gezien.

In hoofdstuk 2 hebben we het ontwerp en de bouw van de experimentele opstelling die we hebben gebruikt voor de studie naar groeiende bellen beschreven. De opstelling is in feite een soda-machine waarmee we in korte tijd een verzadigde oplossing van water met gas kunnen bereiden bij een maximale druk van 1 MPa. Daarna kunnen we op de oplossing op een soepele en gecontroleerde manier oververzadigen tot het gewenste niveau. Als substraat gebruikten wij siliciumchips met hydrofobe putjes die dienst doen als nucleatieplekken. Hiermee konden we het aantal bellen en hun positie in elk experiment precies controleren. We presenteerden de resultaten van de eerste testexperimenten die we gebruikten om te laten zien dat het systeem naar tevredenheid werkte en we lieten tevens de eerste waarnemingen van groeiende bellen zien.

In hoofdstuk 3 bestudeerden we de groei van een enkele bel in een licht oververzadigde oplossing. Voor zover wij weten is een dergelijk experiment niet eerder uitgevoerd. Het geplande testexperiment, waarbij we verwachtten te vinden dat de belstraal in de tijd groeit als $t^{1/2}$, bleek een ingewikkelde puzzel te zijn: telkens weer bleek dat we niet de verwachte groeisnelheid vonden. Na onszelf ervan overtuigd te hebben dat er niets mis was met ons experiment, veranderden we ons perspectief door in plaats van te kijken naar de R versus $t^{1/2}$ curves, te kijken naar de tijdsafgeleide van het beloppervlak als functie van $t^{1/2}$ (figuur 3.2). Dit nieuwe perspectief leverde een waardevolle aanwijzing voor de oplossing van het probleem. Het bleek dat de eerste fase van de belgroei volgens de verwachte tendens plaatsvond en dat

afwijkingen hiervan pas in latere fases optraden. Door te kijken naar de dimensieloze massaoverdracht (Sherwood getal) als functie het Rayleigh getal voor massaoverdracht (het dimensieloze drijfvermogen veroorzaakt door het concentratieveld rond de bel) hebben we tenslotte kunnen bevestigen dat massaoverdracht wordt versterkt door het optreden van natuurlijke convectie.

In hoofdstuk 4 zijn we nader ingegaan op het ontstaan van de natuurlijke convectie. We hebben met verschillende optische technieken, te weten Schlierenvisualisatie en interferometrie, geprobeerd om het concentratieprofiel rond de bel te meten. Echter, de lange optische weglengte van de observatietank, gecombineerd met het zeer subtiele verschil in brekingsindex veroorzaakt door het concentratieprofiel zorgden ervoor dat deze pogingen tevergeefs waren. Een directe experimentele meting van het concentratieprofiel vereist dat het experiment wordt beperkt tot een Hele-Shaw geometrie. Dit zal uiteraard kwalitatief de convectieve stroming be invloeden, maar kan nog steeds tot waardevolle inzichten in het fenomeen leiden. Desalniettemin hebben we, door het uitvoeren van experimenten bij verschillende mates van oververzadiging en voor verschillende begindruk, het ontstaan van natuurlijke convectie onder verschillende omstandigheden kunnen meten. Deze resultaten hebben we vergeleken met een eenvoudige criterium voor de aanvangstijd, gebaseerd op de balans tussen het drijfvermogen en de wrijvingskrachten die werken op het gasarme gebied rond de bel, hetgeen tot een goede overeenkomst leidde.

Wij hebben eveneens experimenten uitgevoerd met N_2 om te zien of er ook natuurlijke convectie is rond bellen bestaande uit een ander gas. In al onze experimenten vonden wij dat de groei van het beloppervlak van N_2 bellen aanvankelijk op dezelfde manier plaatsvindt als voor ce CO2 bellen. Echter, op het moment dat de overgang naar convectieve groei verwacht werd de groei van de N_2 bellen heel onregelmatig en niet meer reproduceerbaar. We wijten dit aan het feit dat voor een dermate lange groeitijd de individuele N_2 bellen niet meer ge isoleerd zijn en de interactie met bellen die groeien op de randen van het substraat belangrijk wordt. Echter, de waargenomen overgang suggereert dat de mengbeweging inderdaad optreedtafvlakt en de groei van bellen be invloedt.

In hoofdstuk 5 hebben we de gelijktijdige groei van bellen verkend. We begonnen met twee bellen en we namen twee soorten interactie waar: een spati ele wanneer bellen naast elkaar groeien en een temporele wanneer bellen groeien van de nucleatieplaats waar eerder andere bellen gegroeid en losgelaten hebben. Voor de spati ele interactie identificeerden we een subtiele, maar consistent reproduceerbare samenwerkingsinteractie waarbij de convectieve stromingen rondom de bellen elkaars groei versterken ten op zichte van het geval van een ge isoleerde bel. Na een dergelijke fase zullen de bellen, als ze zich dicht genoeg bij elkaar bevinden, een storende interactie ontwikkelen en zal hun groei vertragen. Om de temporele interactie te kwantificeren hebben we gekeken naar de toename van het loslaattijd wanneer een reeks van bellen

groeit en loslaat. Het maximale effect van een dergelijke interactie (textit ie de grootste toename in de loslaattijd van een ge isoleerd bellenpaar) wordt verwacht wanneer de overlap van de concentratieprofielen van de bellen maximaal is. Voor een puur diffusieve groei zou dit zijn wanneer de afstand tussen de bellen precies $2R_F$ bedraagt, met R_F de loslaatstraal zoals bepaald door de grootte van de nucleatieplaats. In onze experimenten werd het maximum gevonden bij een kortere afstand, die wij toeschrijven aan de invloed van convectie. Vervolgens hebben we gekeken naar lineaire en driehoekige patronen gevormd door drie bellen. We konden duidelijke verschillen waarnemen vanwege de symmetrie (of juist de afwezigheid daarvan) in de patronen. In lineaire patronen was de middelste bel duidelijk meer be invloed dan de bellen aan de randen. In het geval van een lineair patroon waarbij de bellen loslaten ten gevolge van hun coalescentie was een interessante desynchronisatie waarneembaar, waarbij meestal twee bellen samen loslieten terwijl de derde alleen nog even verder groeide. De desynchronisatie fase was echter nooit stabiel, waardoor elk experiment anders was dan de andere. Bellen die elkaar niet raakten voor ze loslieten of die zich in een driehoekig patroon bevonden waren minder gevoelig voor desynchronisatie, en als er al desynchronisatie optrad was dat altijd minder uitgesproken dan bij de lineair gerankschikte bellen die elkaar raken.

In hoofdstuk 6 is gekeken naar de singulariteit die zich ontwikkelt aan de bovenkant van een bevriezende druppel op een koude plaat. De experimentele uitdaging was hier om de ontwikkeling van het bevriezingsfront te visualiseren, hetgeen niet goed mogelijk is met conventionele optische technieken vanwege het bolvormige oppervlak van de druppel. Een ingenieus experiment waarbij we een tweedimensionale druppel bevroren stelde ons in staat om voor het eerst de randvoorwaarden van het bevriezingsfront te meten en om aan te tonen dat geometrische aspecten inderdaad belangrijker zijn dan dynamische. Dit toont de universaliteit en gelijkvormigheid van de tipvorming aan.

Bij beide onderwerpen hebben we bijgedragen aan een beter begrip van de onderliggende fysica, maar in beide zijn ook nog veel open vragen. Zo zou het interessant zijn om na te gaan hoe bellen groeien in een begrensd systeem en dicht in de buurt van andere bellen. Hoewel we een eerste aanzet hebben gemaakt door te kijken naar de groei van bellen tussen twee platen, is er nog een lange weg te gaan naar poreuze materialen, hetgeen overeenkomt met de situatie van groeiende bellen tijdens de olieproductie. De groei van waterstofbellen tijdens elektrolyse is een andere veelbelovende richting die met behulp van onze experimentele opstelling kan worden bestudeerd. Dit is van cruciaal belang voor de productie van waterstofgas, wat een belangrijke alternatieve energiebron vormt voor fossiele brandstoffen. Een andere (tegengestelde) richting die interessant is om verder te verkennen, en in feite al aan de gang is in ons laboratorium, is het oplossen van bellen bij het opnieuw onder druk zetten van de oplossing. Dit kan weer geofysische gevolgen hebben, aangezien

de groei van vele bellen tijdens oliewinning steeds opnieuw leidt tot een drukverhoging, maar het kan ook gerelateerd zijn aan de stabilisatie van nanobellen. Ten slotte kan men ook denken aan het controleren van de interactie tussen bellen om zo gebruik te kunnen maken van het menggedrag dat ze produceren. Dit kan door de nucleatieplaatsen zo te positioneren dat bellen van verschillende grootte zich op een dusdanige afstand van elkaar bevinden dat hun subtiele samenwerkende interacties maximaal benut kunnen worden. Dit is van belang in bioreactoren waar mengen van vloeistof bij lage Reynolds getallen belangrijk is om massaoverdracht te bevorderen zonder dat kwetsbare cellen beschadigd raken.

Ook voor de bevriezende druppels zijn er nog veel interessante open vragen. Tijdens de experimenten zagen we dat, ondanks het gebruik van ontgast water, bellen vormen bij het vriesfront die vast komen te zitten in het ijs. Dit kan te wijten zijn aan atmosferische lucht die oplost in de vloeistof. De oplosbaarheid van de lucht in het water neemt toe als de het water afkoelt; vandaar dat koud ontgast water onderverzadigd is en de neiging zal hebben om gas op te nemen om zo opnieuw een verzadigde toestand te bereiken. Andere interessante vragen zijn wat bepalend is voor het tot stilstand komen van de contactlijn en van waar precies de bevriezing begint. We zagen dat, nadat de druppel op de plaat terecht gekomen was, de contactlijn van de druppel nog een tijdje kan oscilleren voordat hij tot stilstand komt; dit fenomeen hebben we echter niet systematisch bestudeerd. Ten slotte is het stollen van andere materialen interessant met het oog op de toepassing van het printen van metaaldruppels en 3D printen.

Acknowledgements

The path that led to Enschede started in November 2007 during the meeting of the Division of Fluid Dynamics of the American Physical Society, in Salt Lake City, Utah. Shortly after arriving to my first conference abroad, as a 9th semester Engineering student, I decided to sign in for a student luncheon with a certain Dr. Devaraj van der Meer, who was an alleged specialist on Granular Stuff. I do not remember what made him stand out among the dozen available options of senior scientists who were willing to share a lunch with students while talking about science, but this turned out to be one of the best decisions I have ever made. Maybe at some point during our lunch conversation, or maybe shortly after returning to Mexico, it became clear that I had to apply for graduate school at the Physics of Fluids Group in the University of Twente.

Devaraj, thank you for your patient guidance and friendship. Thanks too for letting me find my own way, in spite of my rather disperse character and multiplicity of interests. You have played a very important part in the broad and exciting intellectual journey during my stay in Twente. Our conversations on very diverse topics have been a source of inspiration and insight.

Thanks to the group staff for creating and maintaining a fantastic place to work. It is hard for me to think of a place with better conditions for doing experimental fluid mechanics. Detlef, I really appreciate your support through the years I have been part of this group. You have always made sure that Daniela and I were well and your scientific input has always been valuable. Andrea, I really admire your dedication, tirelessness and vast knowledge. You consistently provided the key insight to get things unstuck. Chao, thanks a lot for your collaboration, especially at the beginning of my Ph.D. project. Joanita, Bas, Gert-Wim and Martin, you are, without a doubt, the pillars of this group. Thanks for all your help both in work and personal matters. Jacco, our collaboration in the freezing droplet project has been a highlight of my Ph.D. Michel, I learnt a lot about imaging and video-making from you, especially the first time we produced a (winning!) video for the Gallery of Fluid Motion. Leen, it has always been a great pleasure to talk with you about the history of Fluid Mechanics. Also thanks to Leen, Joanita, Bas, Devaraj and Detlef for going at least once to exhibitions of Daniela's work. Thanks to Jacco for promoting her for taking care of the JA@UT exhibition of 2013.

Roberto Zenit, gracias totales. You are a great friend and mentor. Meeting you has been a personal and academic watershed.

After almost three decades of being enrolled in some kind of educational institution, the number of teachers who have picked at my brain is quite large. Thank you all for the noble job you perform. A very special acknowledgement to the two persons who have left the most profound teachings on the importance of being critical and provided admirable examples of impeccability: Tobyanne Berenberg and Félix Núñez Orozco. Thanks to Ricardo Rodríguez

for his brilliant lessons in Thermodynamics, to Javier Cruz for teaching me the basics of Continuum Mechanics in what marked the beginning of my relation with Fluid Mechanics, to Rolando Peralta and Rafael Schouwenaars for providing some of the biggest and motivating challenges at UNAM, to Francisco Ricardo da Cunha for his teachings on Classical Thermodynamics, hosting me during my exchange in Brasil, and guiding me through my graduation project and thanks to José Luiz Alves da Fontura Rodriguez for his teachings on turbulence and convection.

The Physics of Fluids group has provided many friends and colleagues with whom we've shared lessons, trips, meals, sports, beers and fun times. Sander H. and Dimitrios were fantastic partners through long days and nights of studying and solving assignments during our Master's studies. Ivo, Stephan and Laura, our non-axisymmetric collapsing cavities were a delight to work on. Ivo, I learnt a lot from you during my master's project. Hanneke and Joost were great office mates during the memorable times of the "left-handed vegetarian office" you provided fun, inspiration and a lot of help. Tess, I enjoyed your visits to our office. Varghese and Stefan have taken care of keeping the office as a stimulating place, were we often pause for a nice conversation. Stefan introduced a revolutionary tool which improved my experimental image analysis: Golm Capture. Thanks a lot. Álvaro Gómez Marín has become a very good friend and partner in science, music and travels. You and Angie were also great hosts in Munich. Yoshi Tagawa Sensei, Henri Lhuissier and Antonin Eddi, discussions with you were always stimulating and I learnt many things from your experimental expertise. Koen, it was fun to start the freezing droplet project with you on board, especially when we had to go buy dry ice. There are several of us that started our Ph.D.'s around the same time and have therefore tread this path together: Claas-Willem, Tim, Mark-Jan, Rodolfo, Sander W., and Guillaume. We're almost through! I wish you success with whatever comes next. Guillaume, take good care of the Octopus wherever you go. Thanks to Rianne, Boukje, and Carlijn for letting me try to help you through your Master's and Bachelor's projects; I've learnt a lot from you. Peter and Edip, who would've thought that such an innocent-looking simulation of a growing bubble would prove so hard to accomplish. Thanks for your efforts, we're almost there. The friends from the far east: Minori, Takahiro, Yantao, SongChuan, Shing, Vivek, Vamsi, Shantanu and Marie-Jean (who is almost Chinese) it has been nice to cook, eat and share conversations about our cultures with you. The team mates of PoF United: Erik-Jan, Erwin, Bart, Maarten, Bram, Stefan, I hope I was a good goalkeeper in our matches. Erik-Jan, I have very good memories of our courses in Delft. Loreto and Leo, fellow vegetarians and Latin Americans. Theo, it was nice to exchange gardening advice with you. Pascal, I'll never forget your laughter in the corridor. Elena, I'm glad we both quit smoking. Christian, you did a great job in the design of our high-tech soda machine. The Mexican invasion of the PoF group, those who came before and paved the way, and those who shared the time here: Gabriel, you were very helpful when I was trying to get funded to come here. Daniel, Julián, Daniela, Fede, Quique, and Rodrigo you have all been very important in creating a homely atmosphere in Enschede. Fede and Quique, it's been especially meaningful to share such a long part of our University times, both here and back home.

Outside of the PoF group, but within the University, there have also been good friends, teachers, and collaborators. Lissa Roberts, whose course of Technology and Social Order I enjoyed enormously. Arie Rip who provided excellent advice for learning about Science and Technology Policy. Stefan Schlautmann who was extremely helpful with clean room matters and taught me many video editing tricks. Burak and Annemirl with whom we shared

many delicious dinners and a wonderful wedding and trip in Turkey. Suen and Idilio, our dear neighbours and good friends. Jorick and Katerina, with whom we've shared the joy of becoming parents. The Latin American Student Association has been a very important part of life at the University of Twente. It was an honour to be there since the very beginning of the association. Thanks to Andrea for putting the idea forward and pursuing it. Thanks to all of those who were there to set it in motion and who have been keeping it going. Joni, Coen, Laura, Julián, David, Mario, Jealemy, Nayeli, Vicky, Ileana, John, Juan, Edson, Teo, Juan Carlos, Diruji, Sergio, Adriana, Diego, Carolina, Andreea, Javier, Jennifer, Lila, Patti, Marina, Andrés, Vania, and Valentina.

One of the best parts of life in Enschede has been playing music. Comrade David deserves a special acknowledgement. He has been a great friend, scientific collaborator, party companion and musical partner. On a memorable November afternoon in 2009, in the living room of our Deppenbroek apartment, Daniela, David, Julián and myself gave birth to the Chilangos Habaneros. Thanks to all the friends that have been part of this fun musical adventure: Bob, Pawel, Maurizio, Kasia, Álvaro, Juan Carlos, Anne, Jorge, Matteo, Edit, Marine, Effie, Massi, Ada, and Diego.

Another of the most cherished parts of the time here has been the group of friends with whom we have shared so much, and in our own language. Growing vegetables together, bicycle excursions, concerts, dinners, parties and (sometimes heated) debates. Vicky and Lorenzo, Nayeli and Eduardo, Maite and Jorge, Diru and Juan, you are very special and although it's time for most of us to leave, you will always remain dear and close friends for us. Janik and Miguel, your visits in Enschede have been short a widely spaced, yet we have become good friends. I look forward to keep building that when we are back in Mexico.

There are also several collaborators from other places who I am grateful to. Claus-Dieter and the Singapore crowd, Roberto, Pedro, Tandiono, Firdaus, Chon U and Feng Fang, with whom I spent a great three-month internship at the end of my Master's. The freezing drop coalition in Brussels and Paris, Pierre and Phillippe, and Sam, who spent an intense week trying to visualize convection around droplets with me.

Special thanks to Javier Rodríguez for the enthusiastic and stimulating conversations we've had, the collaboration for solving bubble problems and for reading my thesis and giving useful feedback, to Serge Lemay for pointing out related topics to my research in areas that were unknown for me, and to Anton Darhuber for reading this thesis and participating in the committee.

There are several places that I have called home at some point. In all of them there are special persons that have made of each place a true home. Here in Enschede, Frank and Jolanda have been the best neighbours one could ask for. Back in Brasil, Bárbara and Alda were like a sister and a mother to me as soon as I arrived. Bárbara and Marcelo, it's fantastic that we manage to keep meeting in different places every now and then. I deeply cherish your friendship. Daniel, Paulo, Dante, Bugé and Bruno, who unfortunately left us too early, you made my year in Brasil unforgettable. Back in Canada there are friends who are more like family than friends. Lloyd, Diane, Ed and Carol, meeting you has been one of the best things that have happened to me. Kitty, Leo, Veit, Colin, J. Y. and Aaron, I love you guys.

Now getting back to my home home, Mexico, there are the people who have been there all through my life. My parents, to whom I owe a lot of who I am today. Thanks Malú and Oscar for your love and for the enormous effort you put into educating Gaby and I. My little sister, Gaby, who is not so little anymore and is a great friend and accomplice. My

dearest friends, Baxter, Cacho, Anahí, Marina, Luzma, Carlos, Lucía, Marifer, Jero, Holda and Manuel, it's been so many years and so many shared experiences; we grew up together and it's always exciting to meet again and find out how we have evolved in time. My aunts, uncles and cousins, who have always cared about and supported my endeavours. Pita, David, Josie and Lilia, you're far from Mexico, but you are a very special part of the family for me. My new family: Gaby, Daniel, Diego, Ernesto, Alejandro, Raúl, Tirma, Estela and Héctor; I always feel welcome and at home with you and it's always fun when we get together.

After returning to Mexico from the conference that provoked the decision to come to Enschede, I made another of the best decisions in my life (two in the same month, truly remarkable). I accepted a job as a substitute Physics teacher in 'Logos' highschool. I am deeply grateful and indebted towards my friend Anahí for declining the job offer and recommending me for it. In the first day at work I met the biology teacher in the teacher's lounge. At that point nobody imagined that by the end of that year she would quit her job and move to Enschede. Daniela, you truly complete me. You have helped me see, think and feel in ways that I had never experienced before. After seven years of building a beautiful partnership, I look forward to keep walking side by side with you. Together we have made another of those wonderful, life-changing decisions that has brought us immense joy. We named it Lucio, and he is indeed a light in our lives.

About the author

Oscar Raúl Enríquez Paz y Puente was born in Mexico City on September 13th, 1983. He was a reasonably well-behaved kid and a good student. Then he started to play drums. He graduated as a Mechanical Engineer in 2008 from the Universidad Nacional Autónoma de México (UNAM), which he loves deeply. During his bachelor studies he took a one-semester break and went to Canada to work as an apprentice in a machine shop, but also in construction, wood-splitting, hay-packing, and other odd jobs. He fell in love with experimental fluid mechanics during the fifth semester and their affair has lasted ever since. He spent a year as an exchange student at the Universdade de Brasília in Brasil. Upon returning to México he met his life partner, Daniela, who was brave enough to leave everything behind and move to Enschede. They have spent six joyful years there, formed a Latin American music band, started growing vegetables, and welcomed their first-born son Lucio. During his Master and Ph.D. studies Oscar has worked on impact of solids on liquids, impact of liquids on solids, bubble growth and droplet freezing. He has also nourished the humanitarian seed of his formation at UNAM and likes to read, think and write about the relation of science and technology with society. Oscar would like to see a world with less individualism, machismo, and neoliberalism.